THE UNIVERSITY of ADELAIDE

DEVELOPMENT OF NOVEL CONCRETES FOR STRUCTURAL APPLICATIONS

Tianyu Xie
BEng (Architectural Engineering) Hons

Thesis submitted to The University of Adelaide
School of Civil, Environmental and Mining Engineering
in fulfilment of the requirements
for the degree of Master of Philosophy

CONTENTS

THIS PAGE HAS BEEN LEFT INTENTIONALLY BLANK

ABSTRACT

Owing to its properties and cost benefit, concrete is the most widely used construction material globally. The rapid increase in industrialization and urbanization because of the global economy and population growth has increased environmental awareness and attracted attention to new methods and innovations in concrete technology.

To respond to these needs, three novel concrete technologies are investigated in this thesis: eco-binder concrete, concrete produced with recycled concrete, and the use of external and internal reinforcements in conventional high-strength concrete (HSC). Gaps in the current literature were identified and addressed by performing new tests at the University of Adelaide. The investigations have resulted in five journal papers, which are parts of this thesis.

First, the mechanical and durability-related properties of geopolymer concrete (GPC) are reported. GPC is currently investigated as an environmentally friendly alternative to concrete based on ordinary Portland cement (OPC). Because of the lack of literature data regarding the behaviour of coal ash-based geopolymer concrete cured under ambient conditions, this study uses ambiently-cured GPCs to identify the key parameters that affect the properties of fresh and hardened concrete.

Second, the mechanical and durability-related properties of recycled aggregate concrete (RAC) was experimentally investigated in this research. In addition to this, confinement of RAC with fibre-reinforced polymer (FRP) has shown great potential as concrete for high-performance structural elements. Moreover, its use can reduce the environmental impact of natural resources depletion. This thesis also discusses the experimental results that aim to fill in the knowledge gap in the key parameters of the axial compressive behaviour of RAC-filled FRP tubes (RACFFTs) manufactured with carbon FRP (CFRP) or basalt FRP (BFRP) tubes.

Finally, owing to the inherently brittle nature of HSC, even well-confined columns often exhibit temporary postpeak axial strength-softening behaviour, which negatively affects their overall performance. In this study, steel fibres, which effectively delay and stop crack propagation, were used as internal reinforcement to address the aforementioned shortcomings of conventional FRP-confined HSC. To date, this is the first experimental investigation of the effect of key parameters on the axial compressive behaviour of steel fibre-reinforced HSC (SFRHSC)-filled FRP tubes (SFRHSCFFTs).

STATEMENT OF ORIGINALITY

I certify that this work contains no material which has been accepted for the award of any other degree or diploma in my name, in any university or other tertiary institution and, to the best of my knowledge and belief, contains no material previously published or written by another person, except where due reference has been made in the text. In addition, I certify that no part of this work will, in the future, be used in a submission in my name, for any other degree or diploma in any university or other tertiary institution without the prior approval of the University of Adelaide and where applicable, any partner institution responsible for the joint-award of this degree.

I give consent to this copy of my thesis when deposited in the University Library, being made available for loan and photocopying, subject to the provisions of the Copyright Act 1968.

The author acknowledges that copyright of published works contained within this thesis resides with the copyright holder(s) of those works.

I also give permission for the digital version of my thesis to be made available on the web, via the University's digital research repository, the Library Search and also through web search engines, unless permission has been granted by the University to restrict access for a period of time.

_____ _____

Tianyu Xie Date

ACKNOWLEDGEMENTS

Firstly, I would like to acknowledge the support of my supervisors, Dr. Togay Ozbakkaloglu and Dr. Chengqing Wu, for their supervision, inspiration and encouragement over the course of my M.Phil candidature. I would particularly like to thank Dr. Togay Ozbakkaloglu for his continual enthusiasm, vision, patience and determination for my research to succeed.

I would also like to take this opportunity to express my gratitude to all academics and technical staffs who have helped me with this thesis in their fields of expertise. In particular, I thank Mr. Dale Hodson who provided technical assistance throughout the experimental program presented in this thesis.

I am very grateful to my fellow research students and staff: Dr. Thomas Vincent, Dr Xuyuan Li, Dr Feifei Zheng, Dr Eva Beh, Mr. Butje Louk Fanggi, and Ms. Yunita Idris for their friendship, encouragement, and help. I would also like to extend my sincere gratitude to Dr Jian Lim for his continuous support and encouragement through my entire M.Phil progress.

I would also like to thank my girlfriend Rong Lin, my parents, Ninghan Xie, Qian Zhang and my grandparents Professor Yuanzhen Zhang and A/Professor Guanhua Lv for their unwavering support and motivation.

INTRODUCTION

Concrete is the most important and commonly used construction material in the world and second only to water as the most used substance on the planet. It is produced by mixing cementitious materials, water, aggregates, and, if required, admixtures in predetermined proportions. Owing to its favourable material properties and cost benefit, the demand for concrete is growing rapidly because of the increase in world population and improved standards of living in emerging economies. Therefore, the scientific and technological challenges in developing new methodologies and incorporating innovations in concrete technology for improving the structural performance of concrete while reducing its environmental impact are significant.

Ordinary Portland cement (OPC) is typically used as the primary binder in concrete production. However, the production of 1 t of OPC generates nearly 1 t of carbon dioxide and consumes approximately 2.5 t of fuel and raw materials [1-3]. Therefore, the increasing environmental awareness focuses on the need to switch to geopolymer concrete (GPC), which is currently investigated as an environmentally friendly alternative to OPC-based concrete. Owing to its high worldwide availability, the use of coal ash, including fly ash and bottom ash, to produce geopolymer concrete is an attractive recycling option. However, the majority of studies to date on fly ash- and bottom ash-based geopolymers are concerned with geopolymer products cured at high temperatures and the behaviour of ambiently-cured GPCs is somewhat unknown with only a few reports in the literature [4-7]. Chapters 1 and 2 of this thesis report on the first series of experimental investigations on the behaviour of ambiently-cured GPCs. These studies provide important insights into the behaviour of GPCs cured under standard curing conditions that are present in most construction sites.

In recent decades, the rapid increase in industrialization and urbanization owing to the growth of the global economy and population has led to an increased worldwide demand for concrete. Natural aggregates (NA) constitute approximately 70% of the total volume in a concrete mix. The increased use of concrete thereby depletes the natural aggregate resources [8, 9]. Moreover, the demolition of old structures generates large amounts of construction and demolition (C&D) waste that is subsequently disposed to landfills at significant cost, reducing the landfill space as well. To conserve natural aggregate resources and minimize the environmental impact of C&D waste, recycled concrete aggregate (RCA), which is obtained from C&D waste, has been considered as an alternative to natural aggregates in structural concrete over the past two decades [10,11]. It is presently recognized that the use of RCA as coarse aggregate to make RAC is a highly attractive and promising technology for conserving natural resources and reducing the environmental impact of the construction industry. However, a careful review of the literature on RACs shows that there are no studies to date regarding the effect of particle size of coarse aggregate on the behaviour of concrete prepared with different amounts of RCAs and

the same compressive strength. Chapter 3 of this thesis presents the first experimental study to address these research gaps on RACs. The results of this study indicate that RACs exhibit slightly lower mechanical and durability-related properties compared to those of the companion NACs of the same compressive strength. These properties are satisfactory to allow the use of RAC as a feasible alternative to conventional concrete in structural applications, thereby enabling significant environmental and economic benefits that result from the replacement of NACs with RACs to materialize.

In addition, when compared with NACs, RACs exhibit slightly inferior short- and long-term material properties [12-14]. Owing to these shortcomings, RACs are mostly used as non-structural concrete only and the development and applications of such concrete are somewhat limited. It is well established that the external confinement of concrete with FRP tubes significantly improves the concrete compressive behaviour. Over the past few decades, a large number of studies investigated FRP techniques in strengthening existing columns or constructing new composite columns. However, a careful review of the existing literature on confined RACs shows that only a few studies focused on FRP-confined RACs (i.e. [15-18]). Chapter 4 of this thesis presents the first experimental investigation on the axial compressive behaviour of basalt and carbon FRP (BFRP and CFRP) confined RACs. The results of this study show that external confinement of RACs with FRP tube results in a significant improvement in the compressive behavior of the concrete. This in turnopens the great potential of using RAC in infrastructure applications.

FRP-confined HSC columns exhibit highly ductile behaviour under concentric and simulated seismic loading [19-20]. However, as it was shown in several of these studies, because of the inherently brittle nature of HSC, even well-confined columns often exhibit temporary postpeak axial strength-softening behaviour, which negatively affects their overall performance. It is known that the inherently brittle behaviour of plain concrete can be improved by adding steel fibres to the concrete mix [21, 22]. Steel fibre-reinforced HSC (SFRHSC) filled- FRP tubes (SFRHSCFFTs) may form an attractive composite system that is capable of addressing the aforementioned shortcomings in FRP-confined conventional HSC. Chapter 5 of this thesis reports on the first experimental results to date on the axial compressive behaviour of SFRHSCFFTs. The outcome of this experimental study indicates that the presence of steel fibres can partially or fully eliminate the postpeak strength loss of FRP-confined HSC, thereby improving the behaviour of FRP-confined HSC.

Research objectives

This research aims to develop novel concretes for structural applications and address the aforementioned research gaps. Through careful literature reviews, the key parameters of novel concrete were identified and experimentally investigated. Finally, the test results allow to understanding the mechanical and durability properties of ambiently-cured GPCs and RACs with the same compressive strength, and the axial

compressive behaviour of FRP-confined RACs and FRP-confined steel fibre-reinforced HSCs are investigated.

Thesis overview

This thesis consists of five chapters. Each chapter is a manuscript that has been submitted for publication as journal article [1–5]. Table 1 lists the focus areas of each manuscript, including the type of novel concrete technology, experiments, and parameters investigated. Table 2 presents the details of each experimental program as well as the specimen details and experimental results.

Table 1. Summary of publications, research area focused, and test parameters investigated

Publications	Research area focused	Novel concrete technology	Parameters investigated
Xie and Ozbakkaloglu [1]	Mechanical and durability-related properties of ambiently-cured GPCs	Geopolyer binder	1. Mass ratio of fly ash-to-bottom ash 2. Alkaline-to-binder ratio 3. Concrete type
Xie and Ozbakkaloglu [2]	Compressive behaviour and strength development of ambiently-cured GPCs	Geopolyer binder	1. Type of coal ash 2. Particle size of coal ash 3. Chemical composition of coal ash 4. Alkaline-to-binder ratio 5. Concentration of sodium hydroxide solution
Xie and Ozbakkaloglu [3]	Mechanical and durability-related properties of RACs	Recycled concrete aggregate	1. RCA replacement ratio 2. Maximum nominal aggregate size of RCA 3. Concrete mixing method
Xie and Ozbakkaloglu [4]	Axial compressive behaviour of FRP-confined RACs	FRP confinement, recycled concrete aggregate	1. RCA replacement ratio 2. FRP type 3. Specimen cross-sectional shape 4. Concrete strength
Xie and Ozbakkaloglu [5]	Axial compressive behaviour of steel fibre-reinforced concrete	FRP confinement, steel fibre reinforcement	1. Shape of steel fibre 2. Aspect ratio of steel fibre 3. Volume fraction of steel fibre 4. Concrete type

Table 2. Details of experimental studies undertaken

	Specimen details			Properties examined							
Publications	No. of specimens	Specimen type	Concrete type	Axial-compressive behaviour	Compressive strength	Elastic modulus	Flexural strength	Splitting tensile strength	Drying shrinkage	Water absorption	Strength gain with time
Xie and Ozbakkaloglu [1]	10 batches of concrete	Unconfined	GPC	-	Yes	Yes	Yes	-	Yes	Yes	-
Xie and Ozbakkaloglu [2]	11 batches of concrete	Unconfined	GPC	-	Yes	-	-	-	-	-	Yes
Xie and Ozbakkaloglu [3]	14 batches of concrete	Unconfined	RAC	-	Yes	-	-	-	-	-	-
Xie and Ozbakkaloglu [4]	36 CFFTs	FRP-confined	RAC	Yes	Yes	Yes	Yes	Yes	Yes	Yes	-
Xie and Ozbakkaloglu [5]	27 CFFTs	FRP-confined	SFRC	Yes	Yes	-	-	-	-	-	-

REFERENCES FOR INTRODUCTION

[1] Chindaprasirt, P., Chareerat, T., Hatanaka, S., and Cao, T. (2010). High-strength geopolymer using fine high-calcium fly ash. *Journal of Materials in Civil Engineering*, *23*(3), 264-270.

[2] Guo, X., Shi, H., and Dick, W. A. (2010). Compressive strength and microstructural characteristics of class C fly ash geopolymer. *Cement and Concrete Composites*, *32*(2), 142-147.

[3] Habert, G., De Lacaillerie, J. D. E., and Roussel, N. (2011). An environmental evaluation of geopolymer based concrete production: reviewing current research trends. *Journal of Cleaner Production*, *19*(11), 1229-1238.

[4] Temuujin, J., Williams, R. P., and Van Riessen, A. (2009). Effect of mechanical activation of fly ash on the properties of geopolymer cured at ambient temperature. *Journal of Materials Processing Technology*, *209*(12), 5276-5280.

[5] Temuujin, J., Van Riessen, A., and Williams, R. (2009). Influence of calcium compounds on the mechanical properties of fly ash geopolymer pastes. *Journal of hazardous materials*, *167*(1), 82-88.

[6] Geetha, S., and Ramamurthy, K. (2013). Properties of geopolymerised low-calcium bottom ash aggregate cured at ambient temperature. *Cement and Concrete Composites*, *43*, 20-30.

[7] Santa, R. A. A. B., Bernardin, A. M., Riella, H. G., and Kuhnen, N. C. (2013). Geopolymer synthetized from bottom coal ash and calcined paper sludge.*Journal of Cleaner Production*, *57*, 302-307.

[8] Behera, M., Bhattacharyya, S. K., Minocha, A. K., Deoliya, R., and Maiti, S. (2014). Recycled aggregate from C&D waste & its use in concrete–A breakthrough towards

sustainability in construction sector: A review. *Construction and building materials*, *68*, 501-516.

[9] Çakır, Ö. (2014). Experimental analysis of properties of recycled coarse aggregate (RCA) concrete with mineral additives. *Construction and Building Materials*, *68*, 17-25.

[10] Dilbas, H., Şimşek, M., and Çakır, Ö. (2014). An investigation on mechanical and physical properties of recycled aggregate concrete (RAC) with and without silica fume. *Construction and Building Materials*, *61*, 50-59.

[11] Medina, C., Zhu, W., Howind, T., de Rojas, M. I. S., and Fr ás, M. (2014). Influence of mixed recycled aggregate on the physical–mechanical properties of recycled concrete. *Journal of Cleaner Production*, *68*, 216-225.

[12] Elhakam, A. A., Mohamed, A. E., and Awad, E. (2012). Influence of self-healing, mixing method and adding silica fume on mechanical properties of recycled aggregates concrete. *Construction and Building Materials*, *35*, 421-427.

[13] Limbachiya, M., Meddah, M. S., and Ouchagour, Y. (2012). Use of recycled concrete aggregate in fly-ash concrete. *Construction and Building Materials*, *27*(1), 439-449.

[14] Limbachiya, M., Meddah, M. S., and Ouchagour, Y. (2012). Performance of Portland/silica fume cement concrete produced with recycled concrete aggregate. *ACI Materials Journal*, *109*(1), 91-100.

[15] Xiao, J., Huang, Y., Yang, J., and Zhang, C. (2012). Mechanical properties of confined recycled aggregate concrete under axial compression. *Construction and Building Materials*, *26*(1), 591-603.

[16] Xiao, J., Tresserras, J., and Tam, V. W. (2014). GFRP-tube confined RAC under axial and eccentric loading with and without expansive agent. *Construction and Building Materials*, *73*, 575-585.

[17] Zhao, J. L., Yu, T., and Teng, J. G. (2014). Stress-strain behavior of FRP-confined recycled aggregate concrete. *Journal of Composites for Construction*, *19*(3), 04014054.

[18] Islam, M. M., Choudhury, M. S. I., and Amin, A. F. M. S. (2015). Dilation Effects in FRP-Confined Square Concrete Columns Using Stone, Brick, and Recycled Coarse Aggregates. *Journal of Composites for Construction*, 04015017.

[19] Ozbakkaloglu, T. (2012). Axial compressive behavior of square and rectangular high-strength concrete-filled FRP tubes. *Journal of Composites for Construction*.

[20] Ozbakkaloglu, T., and Vincent, T. (2013). Axial compressive behavior of circular high-strength concrete-filled FRP tubes. *Journal of Composites for Construction*.

[21] Bhargava, P., Sharma, U. K., and Kaushik, S. K. (2006). Compressive stress-strain behavior of small scale steel fibre reinforced high strength concrete cylinders. *Journal of advanced concrete technology*, *4*(1), 109-121.

[22] Bencardino, F., Rizzuti, L., Spadea, G., and Swamy, R. N. (2008). Stress-strain behavior of steel fiber-reinforced concrete in compression. *Journal of Materials in Civil Engineering*.

LIST OF PUBLICATIONS

[1] Xie, T., and Ozbakkaloglu, T. (2015). Behaviour of low-calcium fly and bottom ash-based geopolymer concrete cured at ambient temperature. *Ceramics International*, *41*(4), 5945-5958.

[2] Xie, T., and Ozbakkaloglu, T. (2015). Influence of coal ash properties on compressive behavior of FA-and BA-based GPC. *Magazine of Concrete Research*, 10.1680/macr.14.00429.

[3] Xie, T., & Ozbakkaloglu, T. (2015). Influence of Recycled Aggregate Size and Content on Behavior of Recycled Aggregate Concrete, *Journal of Cleaner Production*, (tentatively accepted subject to final revisions).

[4] Xie, T., & Ozbakkaloglu, T. (2015). Behavior of Recycled Aggregate Concrete-filled Basalt and Carbon FRP Tubes. (Submitted).

[5] Xie, T., and Ozbakkaloglu, T. (2015). Behavior of steel fiber-reinforced high-strength concrete-filled FRP tube columns under axial compression. *Engineering Structures, 90*, 158-171.

PUBLICATIONS

THIS PAGE HAS BEEN LEFT INTENTIONALLY BLANK

JOURNAL ARTICLE 1

THIS PAGE HAS BEEN LEFT INTENTIONALLY BLANK

Statement of Authorship

Title of Paper	Behaviour of low-calcium fly and bottom ash-based geopolymer concrete cured at ambient temperature
Publication Status	☑ Published ☐ Accepted for Publication ☐ Submitted for Publication ☐ Publication Style
Publication Details	Ceramics International, 41(4), 5945-5958.

Author Contributions

Name of Principal Author (Candidate)	Tianyu Xie		
Contribution to the Paper	Analysis of test results, and preparation of manuscript		
Signature		Date	2/9/2015

Name of Co-Author	Dr Togay Ozbakkaloglu		
Contribution to the Paper	Supervision of experimental tests, and review of manuscript		
Signature		Date	2/9/2015

Available online at www.sciencedirect.com

ScienceDirect

Ceramics International 41 (2015) 5945–5958

CERAMICS INTERNATIONAL

www.elsevier.com/locate/ceramint

Behavior of low-calcium fly and bottom ash-based geopolymer concrete cured at ambient temperature

Tianyu Xie, Togay Ozbakkaloglu*

School of Civil, Environmental and Mining Engineering, University of Adelaide, Australia

Received 31 December 2014; accepted 7 January 2015
Available online 12 January 2015

Abstract

This paper presents the results of an experimental study on the behavior of fly ash-, bottom ash- and blended fly and bottom ash-based geopolymer concrete (GPC) cured at ambient temperature. A total of 10 bathes of GPC and a single batch of ordinary Portland cement concrete (OPC) were manufactured. The tests of compressive strength, elastic modulus, flexural strength, workability, drying shrinkage and absorption capacity were carried out to determine the properties of fresh concrete and mechanical and durability-related properties of hardened concrete. Test parameters included the mass ratio of fly ash-to-bottom ash, liquid alkaline-to-coal ash binder ratio, coal ash content and concrete type. The results indicate that the selected parameters significantly affect the microstructure and the behavior of GPCs. It is seen that bottom ash-based GPCs exhibited significantly lower geopolymerization than that of the fly ash-based GPCs, resulting in the inferior behavior of the former compared to the latter.

Keywords: Geopolymer concrete (GPC); Bottom ash; Fly ash; Alkali-activated cement; Ambient temperature

1. Introduction

It is well-understood that the manufacture of ordinary Portland cement (OPC)-based concretes requires large quantities of fuel and raw materials, which are obtained through resource exhausting, energy intensive processes that generate emission of large amounts of greenhouse gases (essentially CO_2 and NO_X) into atmosphere. For every ton of OPC produced, nearly one ton of CO_2 is generated and around 2.5 tons of materials, including fuel and other raw materials, are consumed [1–8]. It is estimated that the emission of CO_2 resulting from the production of OPC adds to about 1.35 billion tons per annum, or about 7% of the total greenhouse gas emissions to the earth's atmosphere [9,10]. It is also predicted that global demand of the OPC will have increased by almost 200% by 2050 from 2010 levels [8], and hence the impact of the OPC industry on the environment is believed to become a real issue. With the aim of reducing the handicap of the production of OPCs, a new type of green and environment-friendly concrete, namely, geopolymer concrete (GPC) has recently received some research attention. The term 'geopolymer' was first introduced by Davidovits in 1970s to represent the mineral polymers resulting from geochemistry, as alternative building materials [11,12]. The production of geopolymers takes place through the geopolymerization process and it requires source materials that are rich in silica (Si^{4+}) and alumina (Al^{3+}) content, such as coal ash, kaolin or metakaolin.

Current global production of coal ashes is estimated to be over 600 Mt per annum, of which the fly ash, which is recognized as one of the world's top 5 raw material sources [13], represents 75–80%. A by-product of coal-fired power stations, fly ash is widely used as the source material to manufacture geopolymer products, owing to its aluminosilicate composition, fine size, significant amount of glassy content and availability across the world. However, it is estimated that 70–80% of the produced fly ash is still being disposed of as waste, which causes the coal-fired power industry significant

*Corresponding author. Tel.: +618 8313 6477; fax: +618 8313 4359.
E-mail address: togay.ozbakkaloglu@adelaide.edu.au (T. Ozbakkaloglu).

http://dx.doi.org/10.1016/j.ceramint.2015.01.031
0272-8842/

concern in relation to environmental issues, while also demonstrating the surplus availability of the material [14].

In the geopolymerization process of the fly ash-based GPC, the reaction of aluminosilicate source (i.e. fly ash) and alkali polysiliates results in the formation of a hardened material with three dimensional polymeric chain and ring structure consisting of Si–O–Al–O bond structure [15–21]. A review of the existing literature indicates that most of the existing studies on the behavior of coal ash- based geopolymer concrete have focused on the use fly ash as the aluminosilicate source (i.e. [15–36]). These studies found that such geopolymer concretes have better durability-related (i.e. [21,22,24,34]) and mechanical properties (i.e. [26,27,29]) compared to those of OPCs. Another type of coal ash material, namely the bottom ash, which is produced during the combustion of coal and has similar chemical composition to fly ash, in contrast, has received less research attention in the area of geopolymers. As reported in the literature, bottom ash contains relatively large and irregularly shaped particles with pores and cavities, which results in lower reactivity when used in GPC [37–42]. As a result, at the moment, most of the bottom ash products are being buried in landfills due to lack of development in recycling technologies [43]. Given the similar chemical composition of the material to that of the fly ash and its higher worldwide availability, the utilization of bottom ash in production of geopolymer concrete might form an attractive recycling option. However, only a limited number of studies have been reported in literature to date on the development of bottom ash-based geopolymers, with the majority of these studies focusing on the behavior of geopolymer pastes (i.e. [34,39,44–47]) and mortars (i.e. [37,38,40–43,48–50]) and only a single study reporting on the behavior of bottomash-based geopolymer concretes (i.e. [51]).

The majority of the studies reported to date on fly- and bottom-ash based geoploymers have been concerned with geopolymer products cured under higher temperatures (i.e. curing temperatures over 40 °C), with only a few studies investigating the behavior of fly ash- (i.e. [30,52–56]) and bottom ash- (i.e. [34,43,47]) based geopolymers cured at ambient temperature. Furthermore, the studies on bottom ash-based geopolymers all focused on the behavior of geopolymer pastes or mortars and no study reported to date on bottom ash-based geopolymer concrete cured at ambient temperature. The ambient environment is the typical curing condition of concrete in the majority of the standard construction sites, and hence understanding the behavior of GPCs cured under ambient conditions is of significant interest. Furthermore, it is well known that the stress-related mechanical properties and other long- and short-term behavior of concrete not only depends on the behavior of each constituent materials but the interactions among them. A few studies have been reported to date on the behavior of blended coal ash-based geopolymers (i.e. [38–40,42,48,51]), with the majority of these studies concerned with the behavior of geopolymer mortars and pastes and not concrete. It is revealed by the careful review of the existing literature that no study has been reported to date on the behavior of blended fly and bottom ash-based geopolymer concrete cured at ambient temperature, and the only existing study on the behavior of blended coal ash-based geopolymer concrete adopted curing temperatures of over 60 °C [51].

As the first experimental study reported to date on the behavior of bottom ash- and blended fly and bottom ash-based geopolymer concrete cured under ambient temperature, the study presented in this paper was aimed at examining the microstructure and mechanical and durability-related properties of fly ash-, bottom ash- and blended fly and bottom ash-based GPC. To establish relative performance of GPCs with respect to OPCs, a companion OPC mix was also designed and manufactured. The paper initially provides a summary of the experimental program, including material properties, specimen properties and testing procedures. Following this, the results of the experimental program are presented. Finally, a detailed discussion on the results of the experimental study is provided, where the influences of mass ratio of fly ash-to-bottom ash, liquid alkaline-to-coal ash binder ratio, coal ash content and concrete type are presented along with other key experimental observations.

2. Test program

2.1. Test specimens

A total of 11 batches of concrete, including a single batch of OPC and 10 batches of GPCs, were manufactured in the presented study. A series of tests were undertaken on each batch to establish the properties of the fresh and hardened concrete, including workability, compressive strength, elastic modulus, flexural strength, drying shrinkage, and absorption capacity. In addition, microstructures of the hardened concretes were examined using scanning electron microscopy (SEM). Two types of specimens were used in specimen testing, namely, cylinders and beams. The cylinder specimens were 100 mm in diameter and 200 mm in height, whereas the beam specimens were 100 mm in width, 100 mm in depth and 500 mm in length. To study the behavior of blended coal ash- and bottom ash-based GPCs, some of the specimens were designed to have partial or complete replacement of fly ash with bottom ash. All of the specimens were cured under ambient conditions. The test parameters included: mass ratio of fly ash-to-bottom ash ($M_{FA:BA}$), liquid alkaline-to-binder ratio (l/b), coal ash content (M_A) and concrete type (i.e. OPC or GPC). Three nominally identical specimens were tested for each unique specimen configuration in every type of test.

2.2. Materials

2.2.1. Coal ash

Two types of coal ashes, including fly ash and bottom ash, were blended in different mass ratios and utilized in the present study. The fly ash and the bottom ash were obtained from Port Augusta Power Station, South Australia. These coal ashes were added at different fly ash- to-bottom ash mass ratios ($M_{FA:BA}$) of 100:0, 50:50, 25:75 and 0:100 for the GPC mixes. Both the fly ash and the bottom ash were pre-oven dried for 24 h and cooled at room temperature for more than 3 h before the casting to reduce their moisture content.

Table 1
Mix proportions of concrete.

	OPC	Bottom ash-based GPC		Blended coal ash-based GPC			Fly ash-based GPC				
Label	OPC	B100-1.1	B100-0.5	B50F50-0.5	B50F50-0.3	B25F75-0.5	F100-0.5A	F100-0.5B	F100-0.25	F100-0.3	F100-0.35
FA (kg/m^3)	0	0	0	200	200	300	400	400	475	475	475
BA (kg/m^3)	0	220	400	200	200	100	0	0	0	0	0
Cement (kg/m^3)	400	0	0	0	0	0	0	0	0	0	0
Aggregate (kg/m^3)	1265	1325	1269	1269	1329	1280	1280	1280	1253	1248	1235
Sand (kg/m^3)	542	567	543	550	550	547	547	547	539	535	529
$NaOH+Na_2SiO_3$ (kg/m^3)	0	240	200	200	123	200	200	200	119	140	166
Water (kg/m^3)	200	0	0	0	0	0	0	0	0	0	0
Liquid/binder ratio (*l*/*b*)	0.5	1.1	0.5	0.5	0.3	0.5	0.5	0.5	0.25	0.3	0.35
Slump (mm)	35	160	150	220	185	165	250	260	60	140	235
Hardened density (kg/m^3)[1]	2389	2088	2035	2282	2286	2345	2377	2393	2378	2372	2382

1. At concrete age of 28 days.

Table 2
Chemical compositions of the cement fly ash and the bottom ash (XRF analysis).

Compositions	Cement (%)	Fly ash (%)	Bottom ash (%)
SiO_2	21	49	54
Al_2O_3	6	31	25
Fe_2O_3	3	3	4
CaO	64	5	5
MgO	2	3	2
Na_2O	0	4	3
K_2O	1	1	1
SO_3	1	0	0
TiO_2	—	2	2
P_2O_5	—	1	1
SrO	—	<0.1	<0.1
Mn_2O_3	—	0	0
LOI*	—	0	2

1. Loss on Ignition.

2.2.2. Alkaline activator solution

The multi-compound alkaline activators applied in the present study were premixed by a local supplier and they consisted of distilled water, sodium hydroxide (NaOH) solution and sodium silicate (Na_2SiO_3) solution. The proportions of the three components of the alkaline activator solution were 65.3% water, 24.8% Na_2SiO_3 and 9.9% NaOH by weight. The sodium hydroxide (NaOH) solution at 14 M concentration was used in all GPC mixes. The sodium silicate solution used in the alkaline solution had a silicon dioxide to sodium oxide ratio (SiO_2/Na_2O) of 3.22 in weight (3.33 in molar) and had 62% water by the total weight. The alkaline activator solution was premixed and left to rest for 24 h at ambient temperature prior to casting.

2.2.3. Ordinary Portland cement (OPC)

The ordinary Portland cement (OPC) used in this research was classified as general purpose blended cement and was obtained from a local supplier. The mix proportions of OPC concrete are given in Table 1, and the chemical composition of the OPC is supplied in Table 2.

2.2.4. Aggregates

The coarse and fine aggregates of the present study consisted of crushed bluestone gravel with 7 mm and graded sand with 0.4 mm maximum nominal particle sizes, which were respectively sourced from the McLaren Vale Quarry (Fleurieu Peninsula) and Price Pit (Yorke Peninsula). The same aggregates were used in all concrete mixes and their amounts are supplied in Table 1.

2.3. Mix designs and specimen preparation

As shown in Table 1, seven of the 11 concrete mixes prepared in the present study were designed to contain a single type of coal ash (i.e. either fly ash or bottom ash). These mixes had different alkaline liquid-to-binder (*l*/*b*) ratios and the coal ash contents (M_A). The remaining three GPC mixes were manufactured as blended fly and bottom ash-based GPCs. Two fly ash-to-bottom ash mass ratios (i.e. $M_{FA:BA}=50:50$ or 75:25) were considered. As can be seen in Table 1, $M_{FA:BA}=50:50$ series GPCs contained sister mixes with different *l*/*b* ratios of 0.5 and 0.3 (i.e. B50F50-0.5 and B50F50-0.3). The F100-0.5A and F100-0.5B series adopted an exact same mix design and they were considered as repeat specimens to verify the results were reproducible. The single OPC mix was designed with a water to cement (*w*/*c*) ratio of 0.5 as a companion to GPC mixes with a liquid-to-binder (*l*/*b*) ratio of 0.5.

In the preparation of the OPC and GPC mixes, all the dry materials including the fine and coarse aggregates and binder (i.e. coal ash or Portland cement) were initially mixed in an 80 L capacity rotating pan mixer with fixed blades for approximately three minutes. Subsequently, the liquid components (i.e. premixed alkaline activator solution for the GPCs or water for the OPC) were gradually added to the mixes and wet mixing continued for approximately five minutes to form the concrete. Gentle external vibration was used throughout the pouring processes of all OPC and GPC mixes to ensure proper placement of concrete. All mixing and pouring processes were conducted under the ambient temperature for both OPC and GPC mixes.

Hardened GPC and OPC specimens were demolded after 24 h after casting. Any GPC specimens those were not fully hardened

Table 3
Temperatures of GPCs and ambient temperature during early curing ages.

Concrete series	T_c (°C)[1]/T_a (°C)[2] after mixing			
	1-h	2-h	3-h	4-h
B100-0.5	17.6/17.4	17.7/17.6	17.4/17.5	17.5/17.3
B50F50-0.5	17.5/17.5	17.4/17.4	17.4/17.4	18.2/18.5
B25F75-0.5	16.4/16.2	16.3/16.1	16.3/16.3	16.4/16.1
F100-0.5 A	17.4/17.5	17.3/17.5	17.2/17.7	17.4/17.5
F100-0.25	17.5/17.1	17.5/17.7	17.4/17.0	16.7/17.7

1. Surface temperature of the concrete.
2. Ambient temperature.

after these 24 h periods were allowed extra time to cure in their molds. The demolded specimens were then covered with plastic bags at the top and they were left to cure at ambient temperatures until testing. The strength gain of the OPC and GPCs with age was monitored by compression test at the ages of 3, 7, 28, 56 and 70 days. The temperature of the specimens and ambient environment were monitored during the early stages of curing.

2.4. Specimen designation

The concrete series in Tables 1, 3–5 were labeled as follows: the letters B (for bottom ash) and F (for fly ash) were used to represent the coal ash types used in the GPCs. Each letter was followed by a number that was used to represent the particular mass ratio of fly ash-to-bottom ash used in the mix in percentage. The letter combination OPC was used to indicate the ordinary Portland cement concrete mix. Finally, the last number in the specimen designation was used to make a distinction among the mixes with the same amount of coal ash proportion but different *l/b* ratios. For F100-0.5 series specimens, additional letters A and B were used at the end of the specimen designation to distinguish between the two repeat batches. For instance, B50F50-0.5 is a GPC mix that contained a blend of 50% bottom ash and 50% fly ash with an *l/b* ratio of 0.5.

2.5. Instrumentation and testing

The mechanical properties, including: compressive strength, flexural strength and elastic modulus of concrete were tested using the universal testing machine in the Materials Laboratory of the University of Adelaide. Prior to the compression tests, all cylinder specimens were first ground and then capped at both ends to ensure uniform distribution of the applied pressure. The drying shrinkage of the concrete was monitored up to 70 days of concrete age through measurement of shrinkage strains and related weight losses of the specimens.

3. Test results and experimental observations

3.1. X-ray fluorescence (XRF) analysis of the coal ashes

The chemical compositions and the loss on ignition (LOI) of the fly ash and the bottom ash were determined by using XRF

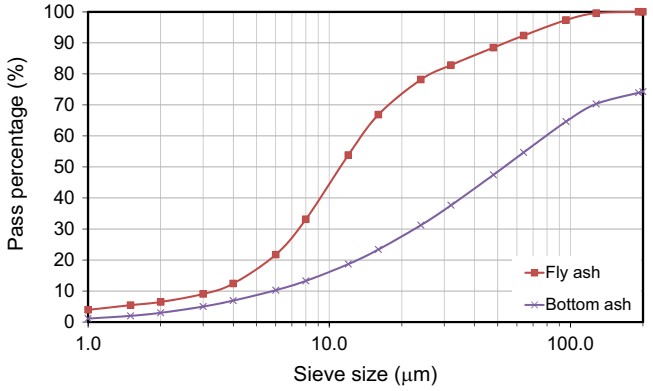

Fig. 1. Sieving test results of fly ash and bottom ash: Particle Size Distribution (PSD).

(X-ray fluorescence). As can be seen from the results of the XRF analysis given in Table 2, both the fly ash and bottom ash had no more than 5% calcium oxide (CaO) and the most abundant oxides in these coal ashes were those of Si^{4+} and Al^{3+}, which represented approximately 80% of the content by weight. Based on these results, the fly ash used in the present study can be classified as type 'F' low-calcium fly ash according to ASTM standard C618-12a [57]. Due to the low CaO and significant SiO_2 and Al_2O_3 contents of the coal ashes, the GPCs of the present study contained mainly sodium aluminosilicate hydrates (N–A–S–H) with only an insignificant amount of calcium silicate hydrates (C–S–H). The chemical composition of the bottom ash reported in Table 2 indicates that the bottom ash had a higher content of SiO_2 and a lower content of Al_2O_3 compared to those of the fly ash from the same source, which resulted in a significantly higher SiO_2/Al_2O_3 ratio of the bottom ash compared to that of the fly ash (i.e. 2.16 vs 1.58 in weight).

3.2. Grading of FA and BA

The Particle Size Distribution (PSD) of the fly and bottom ashes were obtained through the sieving test using a Malvern particle size analyzer. Fig. 1 illustrates the PSD results for both ashes. It is evident from the figure that compared to the fly ash the bottom ash contained coarser particles. The median particle size of the fly ash was 12 μm, whereas that of the bottom ash was 54 μm.

3.3. Morphological characterization of the coal ashes by scanning electron microscopy (SEM)

The scanning electron microscopy (SEM) micrographs were evaluated to investigate the microstructure of the coal ashes, as present in Fig. 2(a) and (b). It can be seen from the Fig. 2(a) that the particles of the fly ash appear to be spherical and with varying sizes. As reported previously [41], these tiny spheres are known as the cenospheres, which have perfectly rounded and intact shapes. In addition, the micrograph of the fly ash also shows that there are no evidently visible pores in the microstructure of the fly ash particles. Fig. 2(b) demonstrates the SEM micrograph of the bottom ash. When compared with the SEM micrograph of the fly ash with the same magnification (i.e. 2000X), the micrograph of

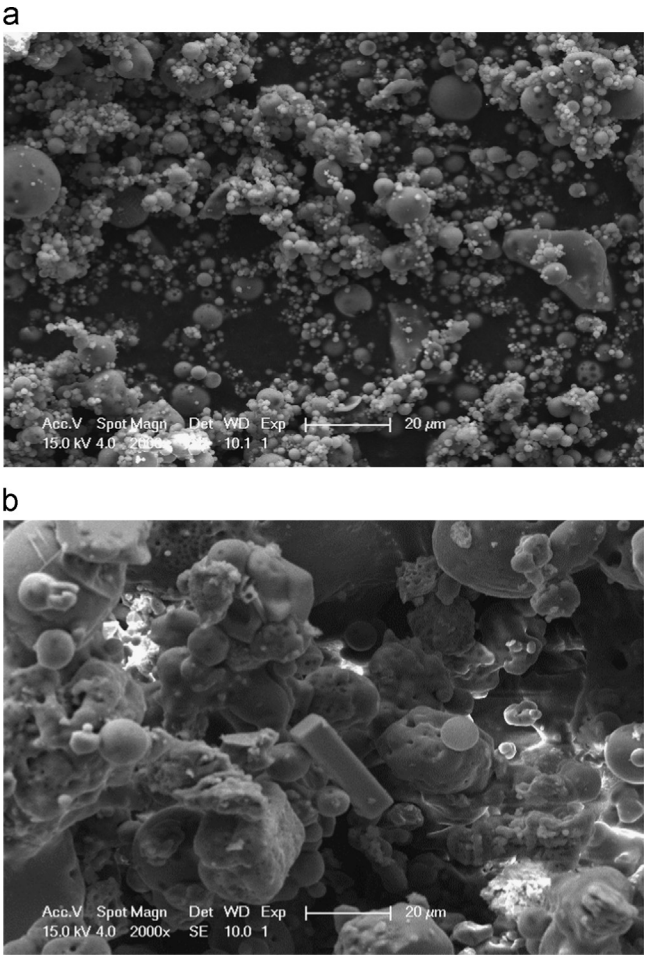

Fig. 2. SEM images of the coal ashes (2000X magnification): (a) fly ash; and (b) bottom ash.

the bottom ash illustrates that the particles of the bottom ash were significantly larger and angular, with plenty of irregular fragments and only a small amount of semi-spheres. The figure also shows some visible pores in the microstructure of the bottom ash. These observations are in agreement with those reported previously on the microstructure of the bottom ash [37,41]. In addition, some foreign objects were observed in the microstructure of the bottom ash samples, for instance, the rectangular shaped foreign object shown in Fig. 2(b). A composition test undertaken indicated the object primarily as Radium – a radioactive earth–metal found in uranium ores. On the other hand, no foreign objects or impurities were observed under SEM for the fly ash samples. These observations clearly indicate that the bottom ash contains more impurities compared to the fly ash, and this can be explained by the fact that the bottom ash is extracted from the base of the furnace, where larger and foreign objects can fall and accumulate.

3.4. Observations of GPC during the curing process

3.4.1. Workability

The workability of each batch of concrete was obtained through slump tests performed in accordance with ASTM standard C143/C143 M [58]. As can be seen from the slump test results summarized in Table 1, the workability of the GPC was found to increase with an increase in the *l/b* ratio. This observation is in general agreement with those previously reported on the coal ash-based geopolymer [38,48], and the increased workability can be explained by the fact that, with an increase in fluid content, the interaction among the coal ash particles decreases due to an increase in the interparticle distance, which in turn results in a lower interference among particles. In addition, for the specimen series B100-0.5, B50F50-0.5, B25F75-0.5, F100-0.5A and F100-0.5B with identical liquid-to-binder ratio (i.e. *l/b*=0.5), it was observed that the slump value increases with an increase in the mass ratio of fly ash-to-bottom ash ($M_{FA:BA}$). This observation indicates that the spherical particle shape and smooth surface of the fly ash provide significant ball-bearing effects, as was also noted previously [1,30], which in turns result in an increase in workability compared to that of the GPCs manufactured with bottom ash. The results also show that the OPC with a *w/c* ratio that was equal to the *l/b* ratio of companion GPC mixes exhibited a significantly lower slump compared to those of the GPCs.

3.4.2. Density

The hardened densities of the OPC and GPCs are reported in Table 1. The densities were established from concrete cylinders at 28 days of age. It is evident from the results given Table 1 that the density of the GPCs increased with an increase in the mass ratio of fly ash-to-bottom ash ($M_{FA:BA}$). The results show that, with an otherwise identical mix design, the 100% bottom ash-based GPCs exhibited significantly lower densities compared to those of the 100% fly ash-based GPCs. This can be attributed to the more porous structure and larger and more irregularly shaped particles of the bottom ash, which results in a GPC with a less dense and homogeneous microstructure. This finding is in agreement with those reported in previous studies on GPCs [37,41] and it can be attributed to that the bottom ash-based concrete contains significant amount of residual liquid (i.e. water and alkaline solution) that remains in its structure after casting. This free liquid subsequently evaporates during the curing process, which results in significantly lower densities of the hardened concrete. The observations presented in this section are also useful in explaining the drying shrinkage and weight loss of GPCs during the shrinkage process, which are discussed later in the paper.

3.4.3. Exothermic reaction

It is well established in the previous studies on OPC that the cement hydration reaction of OPC is exothermic [59–61]. For GPCs, some of the existing studies on coal ash-based geopolymer reported that the mechanism of geopolymerization consists of three phases, including dissolution, transportation/orientation and polycondensation, and it takes place through an exothermic process [9,62–64]. In addition, the exothermic reactions of the GPC were also experimentally observed in some of the previous studies on coal ash- based GPCs those are cured at higher temperatures (i.e. [37,65,66]). Therefore, to examine the exothermic reaction of GPCs cured under ambient conditions, the surface temperature (T_c) of each GPC series and the ambient temperature (T_a) were monitored at early stages of curing. It can be seen from the T_c and T_a values reported in Table 3 that no significant

difference was observed between T_c and T_a. This can be attributed to lower degree of geopolymerization experienced by GPCs at ambient temperature, which resulted in an insignificant exothermic reaction of the GPCs. The above observation is in support of a previous experimental study done by Hardjito and Rangan [2], which found that fly ash-based GPC did not experience a significant exothermic reaction at around 60 °C curing condition. However, this finding is not in general agreement with the theory of geopolymer concrete that geopolymers are formed through an exothermic reaction. This seemingly unexpected observation can be explained by the slow chemical reactions experienced in GPCs at lower ambient temperatures [47,54], which resulted in a less severe heat release process.

3.4.4. Efflorescence

It is well known that, in OPCs, the efflorescence is caused by the formation of carbonate deposits through the reaction of soluble calcium with the water and CO_2 near the surface of concrete [67,68]. The efflorescence is generally not harmful for the OPCs except for the surface discoloration and it is often seen as a 'skin problem rather than a deep-seated disease' [69]. However, previous research established that the efflorescence is detrimental to the durability and mechanical properties of geopolymer materials [31,70–72]. It is well known that, the efflorescence formation in GPC is mainly caused by the reaction of the atmospheric CO_2 with the residual soluble alkalis at the surface of resultant products of geopolymer binders, when the concrete products are exposed to humid air or they get in contact with water [52,73–75]. The mechanism of the efflorescence formation in GPC can be described through the expressions given in Eqs. (1) and (2).

$$CO_2(g) + 2OH^-(aq) \rightarrow CO_3^{2-}(aq) + H_2O \quad (1)$$

$$2Na^+(aq) + CO_3^{2-}(aq) + 7H_2O \rightarrow Na_2CO_3 \cdot 7\,H_2O\,(s) \quad (2)$$

In the present study, the GPC specimens were cast and cured at ambient temperature and they were exposed to the air. As Fig. 3 (a) and (b) show, visible efflorescence formations were observed in some of the GPC specimens. With the aim of reducing the efflorescence, some of the subsequent GPC specimens were cured under sealed conditions. As illustrated in Fig. 3(b), appearance of efflorescence was not observed in the sealed F100-0.5A series specimens, whereas efflorescence was visible in the companion unsealed specimens manufactured using the same concrete mix design. Fig. 4 illustrates the influence of the efflorescence on the 7-day compressive strength (f'_c) of the F100-0.5A and F100-0.25 series. The comparisons indicate that the unsealed specimens exhibited higher 7-day compressive strengths than those of the companion sealed specimens. This observation can be attributed to that the sealed curing prevented the evaporation of water from the GPC, and the presence of excess water in turn resulted in a lower compressive strength. In addition, as shown in Fig. 5, for F100-0.25, F100-0.3 and F100-0.35 series, which contained around 20% additional fly ash content compared to that of F100-0.5A and B series, no significant efflorescence was observed even under the unsealed curing condition. This observation can be explained by the presence of higher amount of the coal ashes in these mixes, which resulted in full utilization of the alkaline solution during the geopolymerization process.

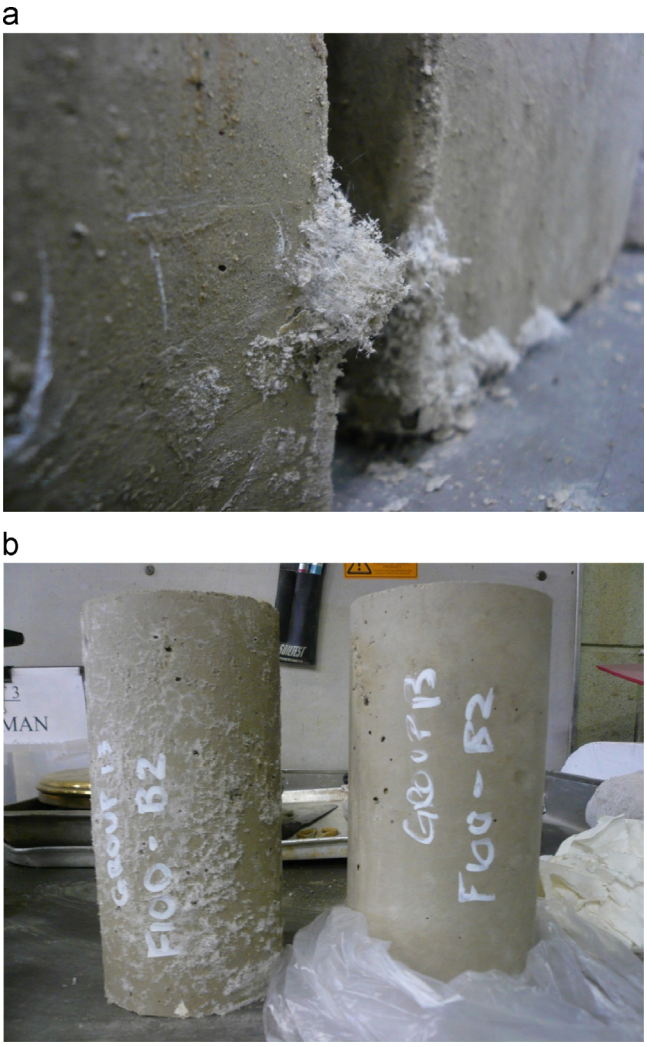

Fig. 3. Efflorescence in geopolymer concrete: (a) efflorescence at the edge of the beam specimen and (b) comparison between a cylinder with efflorescence present (on the left) and a sealed cylinder that exhibits no efflorescence (on the right).

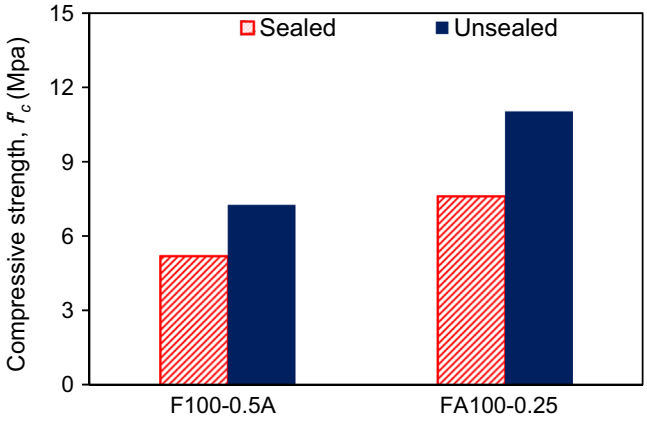

Fig. 4. 7-day compressive strength of sealed and unsealed F100-0.5 and F100-0.25 series of GPCs.

Fig. 5. Appearances of F100-0.25, F100-0.3 and F100-0.35 series: no visible efflorescence.

3.5. Scanning electron microscope (SEM) analysis of the coal ashbased concrete

The SEM micrographs of the hardened GPCs with different fly ash and bottom ash contents are shown in Fig. 6(a)–(e) and Fig. 7 (a)–(e) in 200X and 3500X magnifications, respectively. These SEM micrographs present the microstructures of the B100-0.5, B50F50-0.5, F100-0.5A and FA100-0.25 series of GPCs. Continuous mass of aluminosilicate can be observed from the SEM micrographs shown in Fig. 6(a)–(e) with 200X magnifications. The comparisons of the SEM micrographs of the different GPC mixes in the same figure indicate that the denseness and homogeneity of the GPC microstructure, as the indication of the degree of geopolymerization of GPCs, increase with an increase in the mass ratio of fly ash-to-bottom ash ($M_{FA:BA}$). This finding is in support of those reported in previous studies that compared fly and bottom ash-based GPCs, where it was found that the smaller and more regular particle shape of the fly ash resulted in a higher degree of geopolymerization [37,41]. Another important observation that can be made based on the SEM micrographs at 3500X magnification presented in Fig. 7(a)–(e) is that, in all GPC mixes, a certain amount of coal ash did not fully react during the geopolymerization process and remained in the structure of the hardened concrete. This phenomenon can be explained by the previously noted observation that the reaction of coal ash was relatively slow at ambient temperature.

4. Influence of test parameters on observed behavior

4.1. Mechanical properties of hardened concrete

4.1.1. Axial compressive strength

The compressive strengths (f'_c) of the OPC and GPCs of the present study were obtained through axial compression tests that were performed in accordance with ASTM standard C39/C39M-05 [76]. Table 4 presents the compressive strength (f'_c) of each concrete mix, where the results were averaged from compression tests on three 100 × 200 mm cylinders. Influences of liquid-to-coal ash binder ratio (*l*/*b*), mass ratio of fly ash-to-bottom ash ($M_{FA:BA}$), and coal ash content (M_A) on the compressive strength (f'_c) of GPCs are discussed in the following sections.

4.1.1.1. Effect of alkaline liquid-to-coal ash binder ratio. The influence of alkaline liquid-to-coal ash binder (*l*/*b*) ratio on the compressive strength (f'_c) of GPCs is investigated through the comparison of the GPCs with different *l*/*b* ratios. As can be seen from the results presented in Table 4 and Fig. 8, in general, B100-0.3, F100-0.25 and F100-0.3 series GPCs with lower *l*/*b* ratios developed higher compressive strengths (f'_c) compared to those of the companion mixes with higher *l*/*b* ratios at a given age. This can be explained by the fact that the increase in the *l*/*b* ratio leads to an increase in the water content of the reaction medium, thereby reducing the friction between the particles, which in turn results in a decrease in the compressive strength (f'_c) [48,77]. The above observation is in agreement with those reported previously on coal ash-based GPCs, which noted that the compressive strength (f'_c) of GPCs increases with a decrease in the *l*/*b* ratio [21,22,48,53,77]. It should be noted that the F100-0.25 series with lower *l*/*b* ratio, in contrast, developed a slightly lower compressive strength (f'_c) compared to that of the F100-0.3 series with higher *l*/*b* ratio. This seemingly unexpected observation can be explained by the fact that F100-0.25 series had relatively lower workability compared to that of the F100-0.3 series, which caused problems during the placement of concrete that affected the compressive strength negatively.

It can be seen from the results shown in Table 4 and Fig. 8 that the compressive strengths of the companion fly ash-based specimens, F100-0.5 A and F100-0.5B, were similar to each other, and they were significantly higher than that of their bottom ash-based counterpart, B100-0.5, which had the same mix proportions. As mentioned in Section 3.1, the bottom ash used in the present study had a higher SiO_2/Al_2O_3 ratio compared to that of the companion fly ash. It was noted in previous studies on GPCs that the coal ash-based geopolymers manufactured using an ash with a higher SiO_2/Al_2O_3 ratio tend to develop higher compressive strengths (f'_c) [21,32]. However, the results of the present study indicate that the influence of the lower degree of geopolymerization of the bottom ash had a much more pronounced influence on the compressive strength compared to that of the higher SiO_2/Al_2O_3 ratio of the bottom ash.

The compressive strengths (f'_c) given in Table 4 and Fig. 8 also indicate that the compressive strength (f'_c) of OPC was significantly higher than those of the companion GPCs. As mentioned in the previous section, the OPC used in the presented study was designed to have the same liquid-to-binder ratio (*l*/*b*) and similar mix proportions with that of the B100-0.5, F100-0.5A and F100-0.5B series GPCs. This pronounced difference between the compressive strengths of OPC and GPC can be attributed to the differences in chemical reactions experienced by the two types of concretes, namely hydration in OPC and geopolymerization in GPC. This observation indicates that GPCs cured ambient temperature tends to develop lower compressive strengths than those of OPCs.

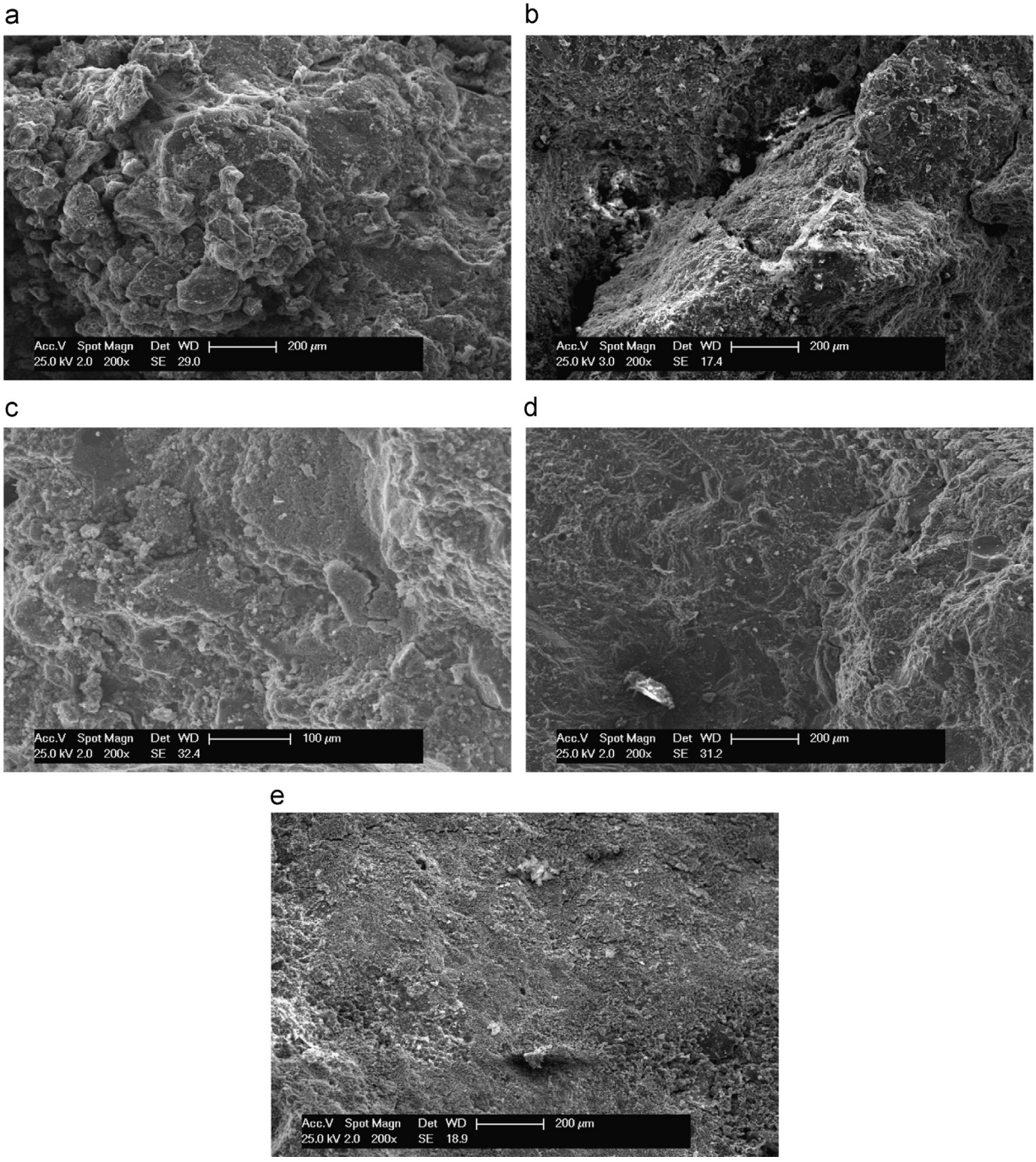

Fig. 6. SEM micrographs (200X magnificantion): (a) B100-0.5 series; (b) B50F50-0.5 series and (c) B25F75-0.5 series; FA100-0.5A series and F100-0.25 series.

4.1.1.2. Effect of mass ratio of fly ash-to-bottom ash. To investigate the influence of mass ratio of fly ash-to-bottom ash on the compressive strength of GPCs, comparisons were conducted among B100-0.5, B50F50-0.5, B25F75-0.5, F100-0.5A and F100-0.5B series GPCs, which had an identical liquid-to-binder ratio (*l*/*b*) but different fly ash-to-bottom ash mass ratios ($M_{FA:BA}$). The results shown in Table 4 and Fig. 8 indicate that the compressive strength (f'_c) increased with an increase in the mass ratio of fly ash-to-bottom ash ($M_{FA:BA}$) used in GPCs. As the properties and quantities of the coarse and fine aggregates used in the companion mixes remained nearly the same among these mixes, this observation indicates that GPC mixes with a higher $M_{FA:BA}$ developed stronger geopolymer mortars. This observation is in agreement with those reported in previous studies on blended fly and bottom ash-based geopolymer mortars [38–40,42,49], and it can be explained by the fact that the degree of polymerization of the bottom ash-based geopolymer is lower than that of the fly ash-based geopolymer [38–40,42,49]. This results in a large amount of unreacted bottom ash particles in the structure of the hardened GPCs, which adversely affect the compressive strength of the bottom ash-based GPCs [37–42]. In addition, as

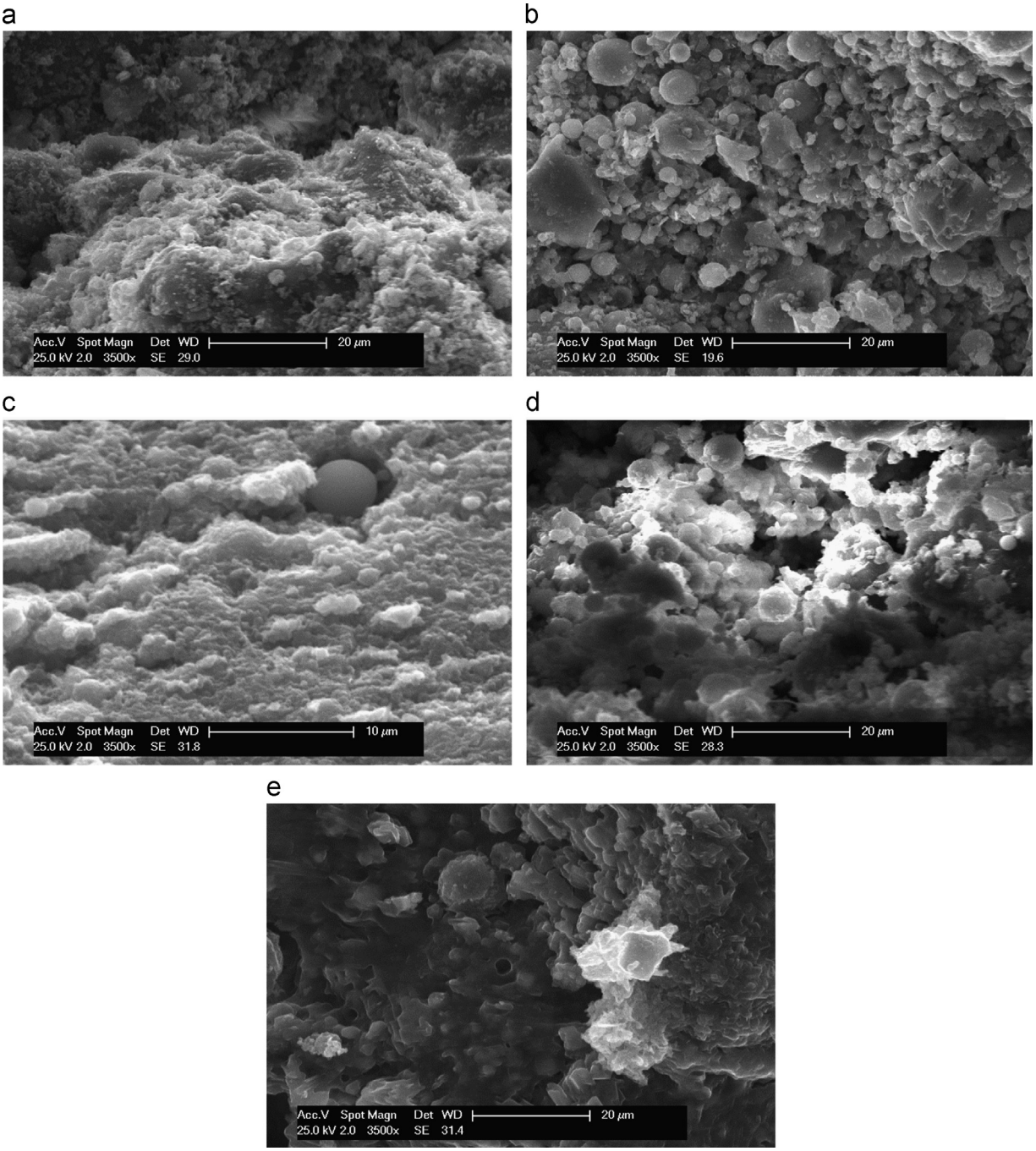

Fig. 7. SEM micrographs (3500X magnification): (a) B100-0.5 series; (b) B50F50-0.5 series and (c) B25F75-0.5 series; F100-0.5A series and FA100-0.25 series.

illustrated in the SEM micrographs shown in Fig. 2(a) and (b), the structure of bottom ash-based GPCs contained micro-cracks and they were less uniform compared to that of the fly ash-based GPCs, which also contributed to their lower compressive strengths.

4.1.1.3. Effect of coal ash content. The influence of coal ash content (M_A) on the compressive strength of GPCs can be studied through the comparison of the F100-0.5A, F100-0.5B, F100-0.25, F100-0.3 and F100-0.35 series of GPCs. As noted previously, F100-0.25, F100-0.3 and F100-0.35 series contained around 20% more fly ash compared to those of F100-0.5 series. It is evident from the results shown in Table 4 and Fig. 8 that the GPCs with higher coal ash content (M_A) developed higher compressive strengths (f'_c) than their companions. As mentioned previously, the efflorescence formations were observed in F100-0.5A and F100-0.5B series, but no visible efflorescence appeared on the F100-0.25, F100-0.3 and F100-0.35 series of GPC specimens, which indicates that the alkalis were completely consumed in the later mixes. These observations suggest that the degree of geopolymerization was relatively higher in F100-0.25, 0.3, 0.35 series compared to that in F100-0.5A, B

Table 4
Axial compressive strength of concrete at different curing ages.

Concrete series	f'_c (7-day) (MPa)	f'_c (28-day) (MPa)	f'_c (56-day) (MPa)	f'_c (70-day) (MPa)
OPC	28.4	38.3	38.9	39.1
B100-1.1[1]	—	0.3	0.6	1.1
B100-0.5	0.2	0.6	—	—
B50F50-0.5	0.8	1.1	1.5	1.8
B50F50-0.3	1.4	3.5	5.4	6.2
B25F75-0.5	3.6	8.4	10.2	12.7
F100-0.5A	7.3	18.8	29.3	32.1
F100-0.5B	7.1	19.5	29.7	33.2
F100-0.25	11.0	30.4	44.4	48.2
F100-0.3	12.6	34.3	—	—
F100-0.35	9.4	27.2	—	—

1. The B100-0.5 series of GPC was too soft for testing at the age of 7 days.

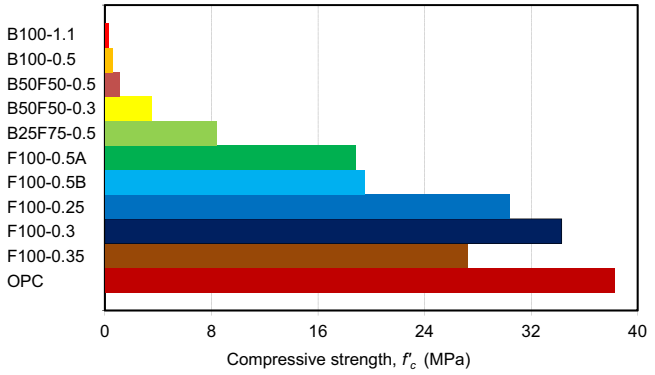

Fig. 8. Compressive strength of concrete at 28 days.

series, which contributed to the higher compressive strength (f'_c) of the former group.

4.1.2. Elastic modulus of GPC

The elastic moduli (E_c) of the selected series of GPC specimens were obtained through the compression tests performed in accordance with ASTM standard C469/C469M-14 [78]. Fig. 9 illustrates the comparison of elastic moduli of B50F50-0.5, B25F75-0.5 and F100-0.5A, which had identical *l/b* ratio and coal ash content (M_A). It can be seen from the Fig. 9 that the elastic modulus of GPCs increased with an increase in the fly ash-to-bottom ash, mass ratio ($M_{FA:BA}$). The results also indicate that there is a strong correlation between the elastic modulus (E_c) and the compressive strength (f'_c) of GPCs, with the elastic modulus of the concrete increasing with an increase in the compressive strength. This observation was expected and it is in accordance with the well-established relationship between elastic modulus (E_c) and compressive strength (f'_c) in OPCs.

4.1.3. Flexural strength of GPC

The flexural strengths ($f'_{r,exp}$) of OPC and B100-0.5, B50F50-0.5, B25F75-0.5 and F100-0.5A series GPC mixes of the present study were obtained through three-point bending tests performed in accordance with ASTM standard C293/C293M-10 [79]. Three 100 mm × 100 mm × 500 mm beams were tested for each mix at three different concrete ages (i.e. 7-day, 28-day and 70-day). It is evident from the results summarized in Table 5 that, at a given concrete age, flexural strengths ($f'_{r,exp}$) of GPCs increased with an increase in the fly ash-to-bottom ash mass ratio ($M_{FA:BA}$). The results also indicate that the relationship between the compressive (f'_c) and flexural strengths ($f'_{r,exp}$) of GPCs are similar to that in OPC, with an increase in the compressive strength (f'_c) resulting in an increase in the flexural strength ($f'_{r,exp}$). The theoretical 28-day flexural strengths ($f'_{r,theo}$) of the OPC and GPCs, calculated from Eq. (3) as per ACI-318-08 [80], are also reported in Table 5.

$$f_{r,theo}' = 0.623\sqrt{f_c'} \quad (3)$$

where both $f'_{r,theo}$ and f'_c are in MPa.

The comparisons of the experimental and theoretical flexural strengths ($f'_{r,exp}$ and $f'_{r,theo}$) at the concrete age of 28 days show that the ACI-318-08 expression provides accurate estimates of the flexural strengths of the OPC and GPCs with a higher fly ash mass ratio (i.e. $M_{FA} > 75\%$). Conversely, in GPCs that contained higher amounts of bottom ash (i.e. B100-0.5 and B50F50-0.5), the differences between the theoretical and experimental values of flexural strengths were pronounced, with the ACI-318 expression underestimating the flexural strengths of the GPCs with higher bottom ash mass ratios (M_{BA}).

4.2. Durability-related properties of concrete

4.2.1. Drying shrinkage

Figs. 10 and 11 respectively illustrate the shrinkage and related weight loss during the drying progress of the OPC mix and B50F50-0.5, B25F75-0.5 and F100-0.5A series GPC mixes, which were cured under constant moisture and ambient temperature up to the age of 70 days. It is evident from Figs. 10 and 11 that the shrinkage strains and associated weight losses of the GPCs were higher than that of the OPC. This is due to the lower degree of geopolymerization experienced by GPCs at ambient temperature, which resulted in structures containing unreacted porous coal ashes. These unreacted coal ashes were filled with water, which was subsequently released during the chemical reaction process of geopolymers. In ambient curing conditions, this water evaporated over a period of time resulting in higher drying shrinkage of GPCs. It was also observed that GPCs with a lower fly ash-to-bottom ash mass ratio ($M_{FA:BA}$) exhibited significantly higher drying shrinkage compared to that of GPCs

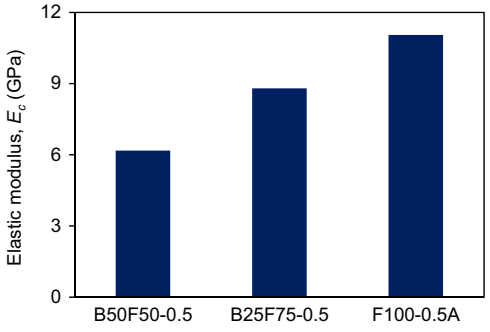

Fig. 9. Elastic modulus of GPCs at the age of 28 days.

Table 5
Flexural strength of concrete at different curing ages.

Concrete series	$f'_{r,exp}$ (7-day) (MPa)	$f'_{r,exp}$ (28-day) (MPa)	$f'_{r,exp}$ (70-day) (MPa)	$f'^{1}_{r,theo}$ (MPa)
B100-0.5	0.30	0.58	—	0.48
B50F50-0.5	0.67	0.83	1.42	0.65
B25F75-0.5	1.01	1.69	2.69	1.80
F100-0.5A	1.52	2.56	3.58	2.70
OPC	—	3.67	—	3.85

1. The theoretical values of flexural strength were calculated by the expression given in ACI-380-08.

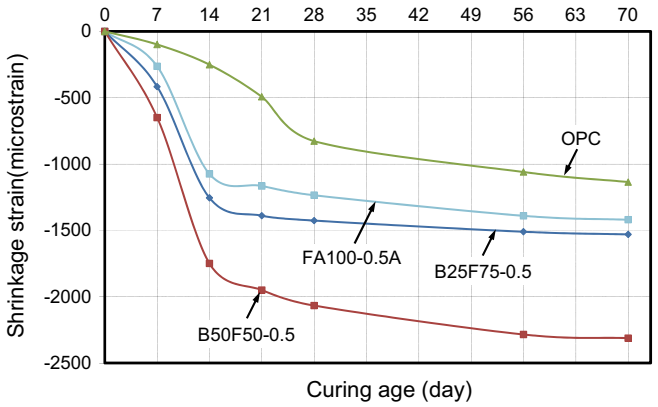

Fig. 10. Drying shrinkage of geopolymer concrete (shrinkage strain).

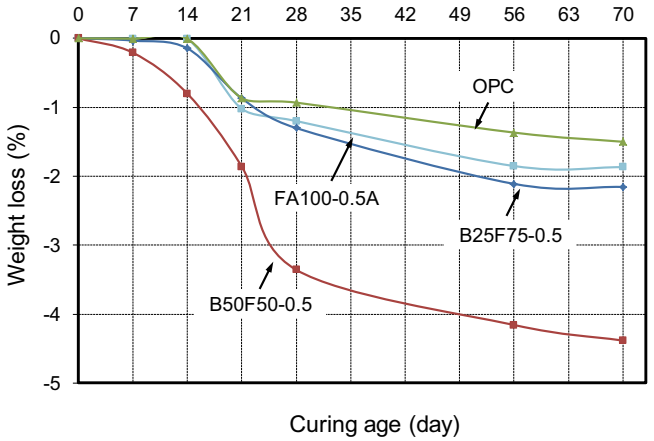

Fig. 11. Weight loss of geopolymer concrete during the shrinkage process.

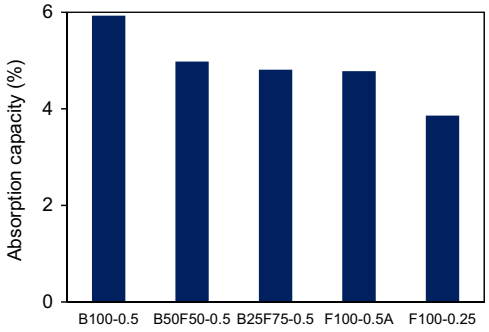

Fig. 12. Absorption capacity of GPCs.

with a higher fly ash to bottom ash mass ratio ($M_{FA:BA}$). As explained in Section 3.4.4, the bottom ash contained particles that are larger, more porous and more irregularly shaped compared to the particles of fly ash, resulting in a higher 'water holding' effect of bottom ash-based GPCs.

4.2.2. Absorption capacity

Absorption tests were carried out on B100-0.5, B50F50-0.5, B25F75-0.5, F100-0.5A and F100-0.25 series GPCs in accordance with ASTM standard C642-13 [81]. 48 h after casting in ambient temperature, the hardened GPC specimens were initially dried in the oven at a temperature of 105 °C over 24 h, and then they were subsequently cooled at the room temperature to determine their oven-dried masses (M_O). Following this, the specimens were immersed in water for 48 h to establish their saturated surface-dry masses (M_S). The absorption capacity (Ai) of GPCs was determined from Eq. (4), as per ASTM C642-13 [81], and the calculated values are shown in Fig. 12.

$$A_i = (M_S - M_O)/M_O \times 100 \quad (4)$$

It can be seen from the results given in Fig. 12 that the absorption capacities of GPCs increase with a decrease in the mass ratio of fly ash-to-bottom ash ($M_{FA:BA}$). As was discussed in previous sections, this can be explained by the lower degree of geopolymerization observed in bottom-based GPC, which in turns leads to a more porous structure and higher absorption capacity.

5. Conclusions

This paper has presented the results of an experimental study on the behavior fly ash-, bottom ash- and blended fly and bottom ash-based geopolymer concrete cured at ambient temperature. Based on the results and discussions presented in this study, the following conclusions can be drawn:

1. The workability of the coal ash-based GPCs is directly related to the mass ratio of fly ash-to-bottom ash ($M_{FA:BA}$) and the liquid-to-binder ratio (l/b), and mixes with a higher fly ash content and l/b ratio exhibit a better workability.
2. No significant exothermic reactions were observed during the curing of the GPCs at the ambient temperature. This indicates that GPCs cured at ambient temperature do not undergo exothermic processes to the extent that are experienced by conventional OPCs.
3. Efflorescence of GPCs can be reduced by using sealed curing method. However, these curing conditions also tend to decrease the early-age compressive strength of GPCs. It is also found that increasing the coal ash content (M_A) with respect to the activator solution can also eliminate efflorescence.
4. SEM micrographs show that the density and homogeneity of the GPC increase with an increase in the mass ratio of fly ash-to-bottom ash ($M_{FA:BA}$). This indicates that fly ash undergoes a higher degree of geopolymerization compared to that seen in bottom ash. SEM micrographs also show that a large amount

of coal ash remains in the hardened GPC structures, which suggests that at the ambient temperature coal ash-based GPCs undergo a lower degree of geopolymerization.

5. Compressive strength (f'_c) of coal ash-based GPCs increases with a decrease in the liquid-to-binder ratio (l/b) or an increase in the mass ratio of the fly ash-to-bottom ash ($M_{FA:BA}$).
6. OPC exhibits a higher compressive strength (f'_c) than that of a companion GPC that is manufactured with the same liquid-to-binder ratio (l/b) and cured under ambient conditions.
7. Both the elastic modulus (E_c) and flexural strength (f'_r) of GPCs have strong correlations to their compressive strength (f'_c), and they both increase with an increase in fly ash-to-bottom mass ratio ($M_{FA:BA}$). ACI-380 model, which is given to predict the flexural strength of OPCs, also provides reasonable estimates of flexural strengths of GPCs manufactured with fly ash mass ratios (M_{FA}) higher than 75%.
8. The ambient temperature cured coal ash-based GPCs exhibit a higher drying shrinkage compared to that of OPCs due to the large amount of unreacted coal ash particles in the hardened GPC structure that results from a lower degree of geopolymerization when coal ash-based GPC is cured at ambient temperature.
9. GPCs with a lower fly ash-to-bottom ash mass ratio ($M_{FA:BA}$) develop higher drying shrinkage due to the lower degree of geopolymerization they experience, and the presence of large, porous and irregularly shaped unreacted bottom ash particles they contain. Likewise, GPCs with a lower $M_{FA:BA}$ exhibits a higher absorption capacity.

Acknowledgments

The authors would like to extend their gratitude to Ms. Poon and Messrs. Chong, James and Warren, who performed the experimental procedures presented in this paper. The authors would also like to thank Adelaide Brighton Pty Ltd. for their generous donation of the test materials used in the study reported in this paper.

References

[1] V.M. Malhotra, Introduction: sustainable development and concrete technology, ACI Concr. Int. 24 (7) (2002) 22.
[2] D. Hardjito, B.V. Rangan, Development and Properties of Low-Calcium Fly Ash-Based Geopolymer Concrete, Curtin University of Technology, Perth, Australia, 2005.
[3] J.M. Miranda, A. Fernández-Jiménez, J.A. González, A. Palomo, Corrosion resistance in activated fly ash mortars, Cem. Concr. Res. 35 (6) (2005) 1210–1217.
[4] F. Pacheco-Torgal, J. Castro-Gomes, S. Jalali, Alkali-activated binders: a review: Part 1. Historical background, terminology, reaction mechanisms and hydration products, Constr. Build. Mater. 22 (7) (2008) 1305–1314.
[5] P. Chindaprasirt, T. Chareerat, S. Hatanaka, T. Cao, High-strength geopolymer using fine high-calcium fly ash, J. Mater. Civ. Eng. 23 (3) (2010) 264–270.
[6] X. Guo, H. Shi, W.A. Dick, Compressive strength and microstructural characteristics of class C fly ash geopolymer, Cem. Concr. Compos. 32 (2) (2010) 142–147.
[7] G. Habert, J.B. D'Espinose de Lacaillerie, N. Roussel, An environmental evaluation of geopolymer based concrete production: reviewing current research trends, J. Clean. Prod. 19 (11) (2011) 1229–1238.
[8] F. Pacheco-Torgal, D. Moura, Y. Ding, S. Jalali, Composition, strength and workability of alkali-activated metakaolin based mortars, Constr. Build. Mater. 25 (9) (2011) 3732–3745.
[9] C. Meyer, The greening of the concrete industry, Cem. Concr. Compos. 31 (8) (2009) 601–605.
[10] X.S. Shi, F.G. Collins, X.L. Zhao, Q.Y. Wang, Mechanical properties and microstructure analysis of fly ash geopolymeric recycled concrete, J. Hazard. Mater. 237 (2012) 20–29.
[11] J. Davidovits, SPE PATEC '79, Society of Plastic Engineering, Brookfield Center, USA, 1979.
[12] J. Davidovits, Chemistry of geopolymeric systems, terminology, in: Proceedings of the 2nd International Conference on the Geopolymere '99, Saint Quentin, vol. 99, 1999, pp. 9–40.
[13] M. Drechsler, A. Graham, Geopolymers- an innovative materials technology bringing resource sustainability to construction and mining industries, in: Proceedings of the IQA Annual Conference 12–15, 2005.
[14] M. Ahmaruzzaman, A review on the utilization of fly ash, Prog. Energy Combust. Sci. 36 (3) (2010) 327–363.
[15] J. Davidovits, Geopolymers, J. Therm. Anal. Calorim. 37 (8) (1991) 1633–1656.
[16] A. Palomo, F.P. Glasser, Chemically-bonded cementitious materials based on metakaolin, Br. Ceram. Trans. J. 91 (4) (1992) 107–112.
[17] J.G.S. Van Jaarsveld, J.S.J. Van Deventer, L. Lorenzen, The potential use of geopolymeric materials to immobilise toxic metals: Part I. Theory and applications, Miner. Eng. 10 (7) (1997) 659–669.
[18] J.G.S. Van Jaarsveld, J.S.J. Van Deventer, G.C. Lukey, The effect of composition and temperature on the properties of fly ash-and kaolinite-based geopolymers, Chem. Eng. J. 89 (1) (2002) 63–73.
[19] D. Hardjito, S.E. Wallah, D.M.J. Sumajouw, B.V. Rangan, Brief review of development of geopolymer concrete, in: Proceedings of the 8th CANMET/ACI International Conference on Fly Ash, Silica Fume, Slag and Natural Pozzolans in Concrete, Las Vegas (USA), May 2004.
[20] P. Duxson, J.L. Provis, G.C. Lukey, J.S. Van Deventer, The role of inorganic polymer technology in the development of 'green concrete', Cem. Concr. Res. 37 (12) (2007) 1590–1597.
[21] D. Khale, R. Chaudhary, Mechanism of geopolymerization and factors influencing its development: a review, J. Mater. Sci. 42 (3) (2007) 729–746.
[22] D. Hardjito, S.E. Wallah, D.M. Sumajouw, B.V. Rangan, On the development of fly ash-based geopolymer concrete, ACI Mater. J. 101 (6) (2004) 467–472.
[23] A. Fernández-Jiménez, A. Palomo, I. Sobrados, J. Sanz, The role played by the reactive alumina content in the alkaline activation of fly ashes, Microporous Mesoporous Mater. 91 (1) (2006) 111–119.
[24] S.E. Wallah, B.V. Rangan, Low-Calcium Fly Ash-Based Geopolymer Concrete: Long-Term Properties. Research Report-GC2, Curtin University, Australia, 2006, pp. 76–80.
[25] P. Chindaprasirt, T. Chareerat, V. Sirivivatnanon, Workability and strength of coarse high calcium fly ash geopolymer, Cem. Concr. Compos. 29 (3) (2007) 224–229.
[26] S. Kumar, R. Kumar, T.C. Alex, A. Bandopadhyay, S.P. Mehrotra, Influence of reactivity of fly ash on geopolymerisation, Adv. Appl. Ceram. 106 (3) (2007) 120–127.
[27] R. Kumar, S. Kumar, S.P. Mehrotra, Towards sustainable solutions for fly ash through mechanical activation, Resour. Conserv. Recycl. 52 (2) (2007) 157–179.
[28] G. Kovalchuk, A. Fernández-Jiménez, A. Palomo, Alkali-activated fly ash: effect of thermal curing conditions on mechanical and microstructural development–Part II, Fuel 86 (3) (2007) 315–322.
[29] X. Fu, Q. Li, J. Zhai, G. Sheng, F. Li, The physical–chemical characterization of mechanically-treated CFBC fly ash, Cem. Concr. Compos. 30 (3) (2008) 220–226.
[30] J. Temuujin, R.P. Williams, A. Van Riessen, Effect of mechanical activation of fly ash on the properties of geopolymer cured at ambient temperature, J. Mater. Process. Technol. 209 (12) (2009) 5276–5280.
[31] J. Temuujin, A. van Riessen, K.J.D. MacKenzie, Preparation and characterisation of fly ash based geopolymer mortars, Constr. Build. Mater. 24 (10) (2010) 1906–1910.

[32] S. Thokchom, K.K. Mandal, S. Ghosh, Effect of Si/Al ratio on performance of fly ash geopolymers at elevated temperature, Arab. J. Sci. Eng. 37 (4) (2012) 977–989.
[33] G.S. Ryu, Y.B. Lee, K.T. Koh, Y.S. Chung, The mechanical properties of fly ash-based geopolymer concrete with alkaline activators, Constr. Build. Mater. 47 (2013) 409–418.
[34] R.A. Antunes Boca Santa, A.M. Bernardin, H.G. Riella, N.C. Kuhnen, Geopolymer synthesized from bottom coal ash and calcined paper sludge, J. Clean. Prod. 57 (2013) 302–307.
[35] B. Nematollahi, J. Sanjayan, Effect of different superplasticizers and activator combinations on workability and strength of fly ash based geopolymer, Mater. Des. 57 (2014) 667–672.
[36] M. Zhang, T. El-Korchi, G. Zhang, J. Liang, M. Tao, Synthesis factors affecting mechanical properties, microstructure, and chemical composition of red mud–fly ash based geopolymers, Fuel 134 (2014) 315–325.
[37] P. Chindaprasirt, C. Jaturapitakkul, W. Chalee, U. Rattanasak, Comparative study on the characteristics of fly ash and bottom ash geopolymers, Waste Manag. 29 (2) (2009) 539–543.
[38] P. Chindaprasirt, U. Rattanasak, Utilization of blended fluidized bed combustion (FBC) ash and pulverized coal combustion (PCC) fly ash in geopolymer, Waste Manag. 30 (4) (2010) 667–672.
[39] K. Boonserm, V. Sata, K. Pimraksa, P. Chindaprasirt, Improved geopolymerization of bottom ash by incorporating fly ash and using waste gypsum as additive, Cem. Concr. Compos. 34 (7) (2012) 819–824.
[40] Q. Li, H. Xu, F. Li, P. Li, L. Shen, J. Zhai, Synthesis of geopolymer composites from blends of CFBC fly and bottom ashes, Fuel 97 (2012) 366–372.
[41] S. Kunjalukkal Padmanabhan, A. Licciulli, Synthesis and characteristics of fly ash and bottom ash based geopolymers–a comparative study, Ceram. Int. 40 (2) (2014) 2965–2971.
[42] D.K. Sinha, A. Kumar, S. Kumar, Development of geopolymer concrete from fly ash and bottom ash mixture, Trans. Indian Ceram. Soc. 73 (2) (2014) 143–148.
[43] S.H. Kim, G.S. Ryu, K.T. Koh, J.H. Lee, Flowability and strength development characteristics of bottom ash based geopolymer, World Acad. Sci. Eng. Technol. 70 (2012) 53–59.
[44] R. Slavik, V. Bednarik, M. Vondruska, A. Nemec, Preparation of geopolymer from fluidized bed combustion bottom ash, J. Mater. Process. Technol. 200 (1) (2008) 265–270.
[45] H. Xu, Q. Li, L. Shen, W. Wang, J. Zhai, Synthesis of thermostable geopolymer from circulating fluidized bed combustion (CFBC) bottom ashes, J. Hazard. Mater. 175 (1) (2010) 198–204.
[46] I.B. Topcu, M.U. Toprak, Properties of geopolymer from circulating fluidized bed combustion coal bottom ash, Mater. Sci. Eng.: A 528 (3) (2011) 1472–1477.
[47] S. Geetha, K. Ramamurthy, Properties of geopolymerised low-calcium bottom ash aggregate cured at ambient temperature, Cem. Concr. Compos. 43 (2013) 20–30.
[48] A. Sathonsaowaphak, P. Chindaprasirt, K. Pimraksa, Workability and strength of lignite bottom ash geopolymer mortar, J. Hazard. Mater. 168 (1) (2009) 44–50.
[49] P. Chindaprasirt, U. Rattanasak, C. Jaturapitakkul, Utilization of fly ash blends from pulverized coal and fluidized bed combustions in geopolymeric materials, Cem. Concr. Compos. 33 (1) (2011) 55–60.
[50] V. Sata, A. Sathonsaowaphak, P. Chindaprasirt, Resistance of lignite bottom ash geopolymer mortar to sulfate and sulfuric acid attack, Cem. Concr. Compos. 34 (5) (2012) 700–708.
[51] M.B.J. Mathew, M.M. Sudhakar, C. Natarajan, Strength, economic and sustainability characteristics of coal ash–GGBS based geopolymer concrete, Int. J. Comput. Eng. Res. (ijceronline.com) 3 (2013) 207–212.
[52] J. Temuujin, A. Van Riessen, R. Williams, Influence of calcium compounds on the mechanical properties of fly ash geopolymer pastes, J. Hazard. Mater. 167 (1) (2009) 82–88.
[53] J. Wongpa, K. Kiattikomol, C. Jaturapitakkul, P. Chindaprasirt, Compressive strength, modulus of elasticity, and water permeability of inorganic polymer concrete, Mater. Des. 31 (10) (2010) 4748–4754.
[54] K. Somna, C. Jaturapitakkul, P. Kajitvichyanukul, P. Chindaprasirt, NaOH-activated ground fly ash geopolymer cured at ambient temperature, Fuel 90 (6) (2011) 2118–2124.
[55] D.L. Kong, J.G. Sanjayan, K. Sagoe-Crentsil, Comparative performance of geopolymers made with metakaolin and fly ash after exposure to elevated temperatures, Cem. Concr. Res. 37 (12) (2007) 1583–1589.
[56] S. Kumar, R. Kumar, Mechanical activation of fly ash: effect on reaction, structure and properties of resulting geopolymer, Ceram. Int. 37 (2) (2011) 533–541.
[57] ASTM, Standard Specification for Coal Fly Ash and Raw or Calcined Natural Pozzolan for Use in Concrete, C618-12a, West Conshohocken, PA, 2012.
[58] ASTM, Standard Test Method for Slump of Hydraulic-Cement Concrete, C143/C143M-12, West Conshohocken, PA, 2012.
[59] F.A. Branco, P. Mendes, E. Mirambell, Heat of hydration effects in concrete structures, ACI Mater. J. 89 (2) (1992) 139–145.
[60] G. De Schutter, L. Taerwe, Degree of hydration-based description of mechanical properties of early age concrete, Mater. Struct. 29 (6) (1996) 335–344.
[61] S. Swaddiwudhipong, D. Chen, M.H. Zhang, Simulation of the exothermic hydration process of Portland cement, Adv. Cem. Res. 14 (2) (2002) 61–69.
[62] A. Palomo, M.W. Grutzeck, M.T. Blanco, Alkali-activated fly ashes: a cement for the future, Cem. Concr. Res. 29 (8) (1999) 1323–1329.
[63] H. Xu, J.S.J. Van Deventer, The geopolymerisation of alumino-silicate minerals, Int. J. Miner. Process. 59 (3) (2000) 247–266.
[64] E. Álvarez-Ayuso, X. Querol, F. Plana, A. Alastuey, N. Moreno, M. Izquierdo, M. Barra, Environmental, physical and structural characterisation of geopolymer matrixes synthesised from coal (co-) combustion fly ashes, J. Hazard. Mater. 154 (1) (2008) 175–183.
[65] L. Weng, K. Sagoe-Crentsil, Dissolution processes, hydrolysis and condensation reactions during geopolymer synthesis: Part I—low Si/Al ratio systems, J. Mater. Sci. 42 (9) (2007) 2997–3006.
[66] F. Škvára, L. Kopecký, V. Šmilauer, Z. Bittnar, Material and structural characterization of alkali activated low-calcium brown coal fly ash, J. Hazard. Mater. 168 (2) (2009) 711–720.
[67] K. Kobayashi, Y. Uno, Influence of alkali on carbonation of concrete, Part 2-influence of alkali in cement on rate of carbonation of concrete, Cem. Concr. Res. 20 (4) (1990) 619–622.
[68] C. Dow, F.P. Glasser, Calcium carbonate efflorescence on Portland cement and building materials, Cem. Concr. Res. 33 (1) (2003) 147–154.
[69] Z. Zhang, H. Wang, J.L. Provis, A. Reid, Efflorescence: a critical challenge for geopolymer applications?, in: Proceedings of the Concrete 2013, 2013.
[70] R.P. Williams, A. Van Riessen, Determination of the reactive component of fly ashes for geopolymer production using XRF and XRD, Fuel 89 (12) (2010) 3683–3692.
[71] Y. Huang, M. Han, R. Yi, Microstructure and properties of fly ash-based geopolymeric material with 5A zeolite as a filler, Construct. Build. Mater. 33 (2012) 84–89.
[72] B. Pandey, S.D. Kinrade, L.J. Catalan, Effects of carbonation on the leachability and compressive strength of cement-solidified and geopolymer-solidified synthetic metal wastes, J. Environ. Manag. 101 (2012) 59–67.
[73] František Škvára, Lubomír Kopecký, Lenka Myšková, V. Šmilauer, L. Alberovska, Lenka Vinšová, Aluminosilicate polymers–influence of elevated temperatures, efflorescence, Ceram.–Silik. 53 (4) (2009) 276–282.
[74] E. Najafi Kani, A. Allahverdi, J.L. Provis, Efflorescence control in geopolymer binders based on natural pozzolan, Cem. Concr. Compos. 34 (1) (2012) 25–33.
[75] Z. Zhang, J.L. Provis, A. Reid, H. Wang, Fly ash-based geopolymers: the relationship between composition, pore structure and efflorescence, Cem. Concr. Res. 64 (2014) 30–41.
[76] ASTM, Standard Test Method for Compressive Strength of Cylindrical Concrete Specimens, C39/C39M-05, West Conshohocken, PA, 2005.
[77] D. Hardjito, V. Jong, The use of fly ash and bottom ash in geopolymer mortar, Doctoral dissertation, Petra Christian University, 2011.

[78] ASTM, Standard Test Method for Static Modulus of Elasticity and Poisson's Ratio of Concrete in Compression, C469 / C469M-14, West Conshohocken, PA, 2014.
[79] ASTM, Standard Test Method for Flexural Strength of Concrete (Using Simple Beam With Center-Point Loading), ASTM C293/C293M-10, West Conshohocken, PA, 2010.
[80] Portland Cement Association, and ACI Committee 318, Building Code Requirements for Structural Concrete and Commentary, PCA notes on ACI 318-02: with design applications, Farmington Hills, Michigan: ACI International, 2004.
[81] ASTM, Standard Test Method for Density, Absorption, and Voids in Hardened Concrete, ASTM C642-13, West Conshohocken, PA, 2013.

JOURNAL ARTICLE 2

THIS PAGE HAS BEEN LEFT INTENTIONALLY BLANK

Statement of Authorship

Title of Paper	Influence of Coal Ash Properties on Compressive Behavior of FA-and BA-based GPC
Publication Status	☑ Published ☐ Accepted for Publication ☐ Submitted for Publication ☐ Publication Style
Publication Details	Magazine of Concrete Research, 10.1680/macr.14.00429

Author Contributions

Name of Principal Author (Candidate)	Tianyu Xie		
Contribution to the Paper	Analysis of test results, and preparation of manuscript		
Signature		Date	2/9/2015

Name of Co-Author	Dr Togay Ozbakkaloglu		
Contribution to the Paper	Supervision of experimental tests, and review of manuscript		
Signature		Date	2/9/2015

Magazine of Concrete Research
http://dx.doi.org/10.1680/macr.14.00429
Paper 1400429
Received 17/12/2014; revised 24/04/2015; accepted 24/04/2015

ice Institution of Civil Engineers
publishing

Influence of coal ash properties on compressive behaviour of FA- and BA-based GPC

Tianyu Xie
MPhil Candidate, School of Civil, Environmental and Mining Engineering, University of Adelaide, Adelaide, Australia

Togay Ozbakkaloglu
Senior Lecturer, School of Civil, Environmental and Mining Engineering, University of Adelaide, Adelaide, Australia

This paper presents the results of an experimental study on the behaviour of fly ash (FA) and bottom ash (BA) based geopolymer concretes (GPCs) cured at ambient temperature. A total of 11 batches of coal-ash-based GPCs were manufactured. Axial compression tests were carried out to determine the compressive behaviour and strength development of hardened GPCs. Test parameters included the type, particle size and chemical composition of coal ash, the alkaline liquid to binder ratio and concentration of sodium hydroxide solution. The results indicate that the chemical composition of BA has a pronounced influence on the compressive behaviour of GPCs, with concretes manufactured with BA with a higher silicon dioxide/aluminium oxide ratio developing higher strengths. The results also indicate that milling of the coal ash and the increased calcium oxide content of the BA both lead to significant improvements in the compressive strength of GPCs. It was also found that strength gain of ambiently cured coal-ash-based GPCs continues beyond a concrete age of 28 d and is significantly influenced by the type, particle size and chemical composition of the coal ash and the concentration of sodium hydroxide solution.

Notation

d_{50}	median coal ash particle size
E_c	elastic modulus
f_c'	concrete compressive strength
l/*b*	alkaline liquid to coal ash binder ratio
ε_{co}	peak axial strain

Introduction

Owing to its favourable material properties and economic benefits, concrete is the most commonly used construction material in the world. Ordinary Portland cement (CEMI) is conventionally used as the primary binder to produce concrete. However, according to statistics, the production of 1 t of CEMI generates nearly 1 t of carbon dioxide and consumes approximately 2·5 t of materials, including fuel and other raw materials (Arellano-Aguilar *et al.*, 2014; Guo *et al.*, 2010; Hardjito and Rangan, 2005; Pacheco-Torgal *et al.*, 2008, 2011). Global carbon dioxide emissions from the production of CEMI amount to around 1·35 billion tonnes annually, which is 5–8% of total anthropogenic greenhouse gas emissions (Chotetanorm *et al.*, 2012; Habert *et al.*, 2011; Meyer, 2009; Reed *et al.*, 2014; Shi *et al.*, 2012; Topçu *et al.*, 2014). Increasing environmental awareness has seen recent research attention turn to geopolymer concrete (GPC), which is currently being investigated as a sustainable and environmentally friendly alternative to CEMI-based concrete. The term 'geopolymer' was first coined by Davidovits in the 1970s to represent the mineral polymers resulting from geochemistry as potential alternative binders to CEMI (Davidovits, 1979, 1999). The chemical reaction process for producing geopolymers is commonly known as 'geopolymerisation', and it requires source materials that are rich in silica (Si^{4+}) and alumina (Al^{3+}) content such as coal ash, kaolin or metakaolin.

In the geopolymerisation of coal-ash-based geopolymers, the reaction of the aluminosilicate source (i.e. coal ash) and alkali polysilicates results in the formation of a hardened material with a three-dimensional polymeric chain and ring structure consisting of a Si–O–Al–O bond structure (Davidovits, 1991; Duxson *et al.*, 2007; Hardjito *et al.*, 2004a; Khale and Chaudhary, 2007; Palomo and Glasser, 1992; Van Jaarsveld *et al.*, 1997, 2002).

Fly ash (FA), a type of coal ash material that accounts for over 70% of the global production of coal ash per annum (Ahmaruzzaman, 2010; Nassar *et al.*, 2013), is widely accepted across the world as a source material to produce geopolymers owing to its rich aluminosilicate composition, fine size, significant glassy content and high availability (Chindaprasirt *et al.*, 2007; Cwirzen *et al.*, 2014; Ferreira *et al.*, 2013; Fu *et al.*, 2008; Hardjito *et al.*, 2004b; Kovalchuk *et al.*, 2007; Pan *et al.*, 2011; Rattanasak and Chindaprasirt, 2009; Ryu *et al.*, 2013; Temuujin *et al.*, 2009b, 2010; Thokchom *et al.*, 2012; Wallah and Rangan, 2006; Zhang *et al.*, 2014b).

Bottom ash (BA) is a byproduct produced during the combustion of coal, which shares a similar chemical composition

to FA but, in contrast, has received significantly less research attention in the area of geopolymers. As established in previous studies, when compared with FA, BA contains relatively large and irregularly shaped particles with pores and cavities, which results in lower reactivity when used in geopolymers (Boonserm *et al.*, 2012; Chindaprasirt and Rattanasak, 2010; Chindaprasirt *et al.*, 2009; Kunjalukkal and Licciulli, 2014; Li *et al.*, 2012; Sinha *et al.*, 2014). Currently, most BA products are being buried in landfills due to lack of development in recycling technologies (Kim *et al.*, 2012). However, given its similar chemical composition to FA and its greater worldwide availability, BA might provide an attractive option for use as the raw material in the production of geopolymers.

A review of existing studies on FA- and BA-based geopolymers revealed that the majority were concerned with geopolymer products cured at higher temperatures (i.e. over 40°C), with only a few studies focusing on the behaviour of FA-based (e.g. Kong *et al.*, 2007; Kumar and Kumar, 2011; Somna *et al.*, 2011; Temuujin *et al.*, 2009a, 2009b; Wongpa *et al.*, 2010) and BA-based (e.g. Antunes *et al.*, 2013; Geetha and Ramamurthy, 2013) geopolymers cured at ambient temperature. In the majority of engineering applications, concrete is typically cured under ambient conditions, and hence evaluation of the performance of concrete in practice requires an understanding of the behaviour of geopolymers cured under such conditions. The literature review also revealed that, among the reported studies on the use of BA to develop geopolymers, most have focused on the behaviour of geopolymer pastes (e.g. Antunes *et al.*, 2013; Boonserm *et al.*, 2012; Chen *et al.*, 2012; Geetha and Ramamurthy, 2013; Slavik *et al.*, 2008; Topçu and Toprak, 2011; Topçu *et al.*, 2014; Xu *et al.*, 2010) and mortars (e.g. Chindaprasirt and Rattanasak, 2010; Chindaprasirt *et al.*, 2009, 2011; Chotetanorm *et al.*, 2012; Kim *et al.*, 2012; Kunjalukkal and Licciulli, 2014; Li *et al.*, 2012; Sata *et al.*, 2012; Sathonsaowaphak *et al.*, 2009; Sinha *et al.*, 2014), with only one reported study on the behaviour of BA-based GPCs (e.g. Mathew *et al.*, 2013). It is well known that the stress-related behaviour of concrete not only depends on the behaviour of each constituent material but also on the interactions among them. Further research is thus needed to fully investigate the behaviour of geopolymer 'concrete', which is manufactured using coarse and fine aggregates together with geopolymer paste.

Furthermore, existing studies on BA-based geopolymers have focused on using BA from a single source – there are no reported studies on the relative performance of geopolymers manufactured using BAs obtained from different sources. Due to differences in the design of coal-fired boilers and the characteristics of the coals and raw mineral materials in different coal ash sources, the chemical composition and physical condition of coal ashes vary from one power station to another, which in turn could affect the properties of the resulting geopolymer products. It is therefore important to gain an understanding of the influence of the coal ash source on the mechanical properties of GPC. In addition, as revealed in several previous studies (e.g. Antunes *et al.*, 2013; Boonserm *et al.*, 2012; Chindaprasirt and Rattanasak, 2010; Chindaprasirt *et al.*, 2009; Kiattikomol *et al.*, 2001; Kim *et al.*, 2012; Kong *et al.*, 2007; Sathonsaowaphak *et al.*, 2009; Somna *et al.*, 2011; Temuujin *et al.*, 2009b; Topçu and Toprak, 2011; Topçu *et al.*, 2014), reducing the particle size of FA (e.g. Kiattikomol *et al.*, 2001; Somna *et al.*, 2011; Temuujin *et al.*, 2009b) and BA (e.g. Antunes *et al.*, 2013; Boonserm *et al.*, 2012; Chindaprasirt and Rattanasak, 2010; Chindaprasirt *et al.*, 2009; Kim *et al.*, 2012; Kong *et al.*, 2007; Sathonsaowaphak *et al.*, 2009; Topçu and Toprak, 2011; Topçu *et al.*, 2014) through grinding can promote the reactivity of coal ashes, thereby significantly improving the mechanical properties of the resulting geopolymer products. However, research on the use of milled coal ash in ambiently cured GPC is so far extremely limited, with only a few studies reported on ambiently cured FA-based GPCs (e.g. Somna *et al.*, 2011; Temuujin *et al.*, 2009b) and BA-based GPCs (e.g. Antunes *et al.*, 2013; Kim *et al.*, 2012). Further research is needed to better understand the influence of milling on the compressive behaviour of FA- and BA-based GPCs.

The study presented in this paper aimed at examining the compressive behaviour and strength development of BA-based GPCs. To establish the relative performance of BA-based GPCs with respected to FA-based GPCs, four batches of FA-based GPCs were also designed and manufactured. The paper initially provides a summary of the experimental programme, including material properties, specimen properties and testing procedures. Following this, the experimental results are presented and discussed in detail. The influences of coal ash type (FA or furnace BA), particle size (as-received or milled) and chemical composition (considering ashes obtained from different power plants), alkaline liquid to coal ash binder ratio ($l/b = 0{\cdot}25$ to $1{\cdot}1$) and concentration of sodium hydroxide (NaOH) solution (10M or 14M) are presented along with other key experimental observations.

Test programme

Test specimens

A total of 11 batches of GPC – four batches of FA-based GPC and seven batches of furnace BA-based GPC – were manufactured. The specimens were tested under axial compression to establish the mechanical properties of the hardened GPCs including compressive strength, peak axial strain and modulus of elasticity. The cylindrical specimens used in the compression tests were 100 mm in diameter and 200 mm in height. The compressive strength of each GPC mix was monitored up to 70 d to investigate the strength development of the coal-ash-based GPCs cured at ambient temperature. Three nominally identical specimens were tested for each unique specimen configuration in each test. In addition, the microstructures of the raw and milled coal ashes were examined using scanning electron microscopy (SEM) to investigate the effect of milling on the coal ash particles.

Materials

Fly ash

The FA used in the present study was sourced from Port Augusta Northern power station in South Australia. To study the effect of FA particle size on the compressive behaviour of FA-based GPCs, two different particle sizes were used in the GPC mixes – the as-received FA and FA that was milled for 3 min. To reduce its moisture content, the FA was oven dried for 24 h at 105°C. It was subsequently cooled at ambient temperature for more than 3 h before mixing of the concrete.

Bottom ash

The furnace BAs used in the presented study were sourced from three different power stations in Australia, namely Port Augusta Northern power station in South Australia, Bayswater power station in New South Wales and Tarong power station in Queensland. The effect of a reduction in BA particle size on the compressive behaviour of GPCs was studied through the use of as-received BA and BA that was milled for 3 min. As with the FAs, BAs were also oven dried for 24 h at 105°C and cooled at ambient temperature for more than 3 h before mixing.

Alkaline activator solutions

The multi-compound alkaline activator liquid used in the present study was premixed by a local supplier and consisted of distilled water, sodium hydroxide solution and sodium silicate solution. The proportions of the three different components were 65·3% water, 24·8% sodium silicate and 9·9% sodium hydroxide by weight before mixing. Two different concentrations of sodium hydroxide solution (i.e. 10M or 14M) were used. The sodium silicate solution used in the alkaline solution had a constant silicon dioxide to sodium oxide ratio of 3·22 in mass ratio (3·33 in molar ratio) and contained 62% water by total weight. The alkaline activator solution was premixed and rested for 24 h in the ambient environment prior to GPC mixing.

Aggregates

The coarse and fine aggregates used consisted of crushed bluestone gravel of a maximum nominal particle size of 7 mm and graded sand of 0·4 mm maximum nominal particle size, respectively sourced from the McLaren Vale Quarry (Fleurieu peninsula) and Price Pit (Yorke peninsula). The same aggregates were used in all the concrete mixes, and the amounts used are listed in Table 1.

Specimen designation

The specimens were labelled as follows. The first letter indicates the coal ash type used in the GPC – B represents bottom ash and F represents fly ash. The second letter in each specimen designation represents the type of coal ash used in the GPCs – P means the ash was sourced from Port Augusta Northern power station, B represents Bayswater power station and T is used for Tarong power station. The third letter indicates if the coal ash was used in the concrete mix as-received (A) or after milling (M). These letters are followed by two numbers that respectively indicate the molar concentration of sodium hydroxide solution used in the activator liquid (i.e. either 10M or 14M) and the alkaline liquid to ash binder ratio (*l*/*b*) of the mix. For example, BPM10-0·5 is a GPC mix manufactured using milled BA sourced from Port Augusta power station, and had a sodium hydroxide concentration of 10M and an *l*/*b* ratio of 0·5.

Mix design and specimen preparation

As shown in Table 1, four of the concrete mixes prepared in the present study were designed as FA-based mixes. These mixes had different *l*/*b* ratios, coal ash particle sizes and sodium hydroxide concentrations. The remaining seven mixes were manufactured as BA-based GPCs.

In the preparation of concrete mixes, all the dry materials (fine and coarse aggregates and binder (i.e. coal ash)) were initially mixed in an 80 l capacity rotating pan mixer with fixed blades for approximately 3 min. Subsequently, the liquid component (i.e. premixed alkaline activator solution) was gradually added to the mixes and wet mixing was continued for approximately 5 min to form the concrete. After the slump test, additional superplasticiser was added to the mixes that were found to exhibit lower slumps based on the initial slump tests, in order to attain workable mixes. Gentle external vibration was used throughout the pouring processes of all GPC mixes to ensure proper placement of the concrete. All mixing and pouring processes were conducted at ambient temperature.

Hardened specimens were demoulded 24 h after casting. Any specimens that were not fully hardened after this 24 h period were allowed extra time to cure in their moulds. The demoulded specimens were then covered at the top with plastic bags, and they were left to cure at ambient temperature until testing. Strength development of the GPCs was monitored by compression tests undertaken at ages of 7, 28, 56 and 70 d.

Instrumentation and testing

A LabTechnics LM5-P mechanical grinder (Figure 1) was used to grind the coal ashes to reduce their particle sizes. The axial compression tests were undertaken in accordance with ASTM C39/C39M-05 (ASTM, 2005), using a universal testing machine in the Materials Laboratory of the University of Adelaide. The elastic modulus (E_c) of the selected specimens was established according to ASTM C469/C469M-14 (ASTM, 2014). Prior to the compression tests, all cylinder specimens were first milled and then capped at both ends to ensure uniform distribution of the applied pressure.

Experimental observations and results

X-ray fluorescence (XRF) analysis of the coal ashes

The chemical composition and loss on ignition of the FAs and BAs were determined using XRF. As shown in Table 2, the

Label	FA-based GPCs				BA-based GPCs						
	FPM10-0·5	FPM14-0·5	FPA14-0·5	FPA14-0·25	BPM10-0·5	BPA10-0·5	BPA14-0·5	BPA14-1·1	BBM10-0·5	BBA10-0·5	BTM10-0·5
FA: kg/m^3	400	400	400	475	0	0	0	0	0	0	0
BA: kg/m^3	0	0	0	0	400	400	400	220	400	400	400
Aggregate: kg/m^3	1280	1280	1280	1253	1280	1280	1280	1325	1280	1280	1280
Sand: kg/m^3	547	547	547	539	547	547	547	567	547	547	547
Sodium hydroxide + sodium silicate: kg/m^3	200	200	200	119	200	200	200	240	200	200	200
Superplasticiser: kg/m^3	5	7	0	0	0	0	0	0	7	8·5	0
Liquid to binder ratio, *l*/*b*	0·5	0·5	0·5	0·25	0·5	0·5	0·5	1·1	0·5	0·5	0·5
Sodium hydroxide concentration: M	10	14	14	14	10	10	14	14	10	10	10
Slump: mm[a]	110	60	250	60	160	90	150	160	70	20	190
Hardened density: kg/m$^{3[b]}$	2315	2365	2377	2378	2109	2088	2035	2039	2378	2372	2382

[a]Measured before addition of superplasticiser
[b]At concrete age 28 d

Table 1. Mix proportions of FA- and BA-based GPCs

Figure 1. Mechanical grinder used to grind the coal ash

coal ashes had less than 5% calcium oxide and the most abundant oxides were silicon dioxide and aluminium oxide, which represented over 80% of the content by weight. Based on the XRF results, the FA used in the present study can be classified as 'type-F' low-calcium FA according to ASTM C618-12a (ASTM, 2012a). Due to the low calcium oxide content and significant silicon dioxide and aluminium oxide contents of the coal ashes, the GPC products in the present study are expected to mainly include sodium aluminosilicate hydrates with only insignificant amounts of calcium silicate hydrates. Closer inspection of the XRF results in Table 2 indicates that the chemical composition of the BA varied from one type to another. This can be attributed to differences in the design of the coal-fired boilers used in the different power plants, and the characteristics of the coals and raw mineral materials. As shown in Table 2, type-B BA had a higher content of silicon dioxide and a lower content of aluminium oxide than the type-P BA, resulting in a higher silicon dioxide/aluminium oxide mass ratio for the type-B BA (2·46) than for the type-P BA (2·18). In addition, the BA obtained from Tarong power station had the highest silicon dioxide content of the three types of BAs used, being 68·4% by weight compared with 54·1% for type-P BA and 56·6% for type-B BA. With an aluminium oxide content nearly identical to that of the other BAs and a significantly higher silicon dioxide content, the type-T BA had the highest silicon dioxide/aluminium oxide mass ratio among the BAs used in the present study.

	FA		BA	
	Type-P (Port Augusta)	Type-P (Port Augusta)	Type-B (Bayswater)	Type-T (Tarong)
Silicon dioxide (SiO_2): wt%	49·0	54·1	56·6	68·4
Aluminium oxide (Al_2O_3): wt%	31·0	24·8	23·0	24·3
Iron oxide (Fe_2O_3): wt%	2·8	3·9	9·9	2·9
Calcium oxide (CaO): wt%	5·0	4·9	4·3	0·2
Magnesium oxide (MgO): wt%	2·5	2·4	1·2	0·2
Sodium oxide (Na_2O): wt%	3·8	3·5	0·3	0·0
Potassium oxide (K_2O): wt%	1·2	0·7	1·1	0·5
Sulfur trioxide (SO_3): wt%	0·3	0·1	<0·1	<0·1
Titanium dioxide (TiO_2): wt%	2·1	2·2	1·3	1·2
Phosphorus pentoxide (P_2O_5): wt%	0·9	0·6	0·2	<0·1
Strontium oxide (SrO): wt%	<0·1	<0·1	<0·1	<0·1
Manganese(III) oxide (Mn_2O_3): wt%	<0·1	0·1	0·1	<0·1
Loss on ignition: wt%	0·3	1·8	1·8	1·3

Table 2. Chemical composition of FA and furnace BA as determined by XRF analysis

The calcium oxide content of the type-T BA was also significantly lower than that of the type-P and type-B BAs.

Grading of fly ash and bottom ash

The particle size distributions (PSDs) of the as-received and milled coal ashes (Figure 2) were obtained through sieving tests using a Malvern particle size analyser. It is evident from Figure 2 that the as-received (raw) BAs contained much coarser particles than the raw FA. The median size (d_{50}) of the raw type-P FA was 12 μm, whereas that of the raw type-P BA was 54 μm. The figure also shows that the d_{50} of BAs decreased significantly after grinding. For example, for the as-received type-B BA, d_{50} was 48 μm whereas d_{50} for ground type-B BA was 13 μm. As is also evident from Figure 2, the three different BAs used in this study had nearly identical PSDs after milling.

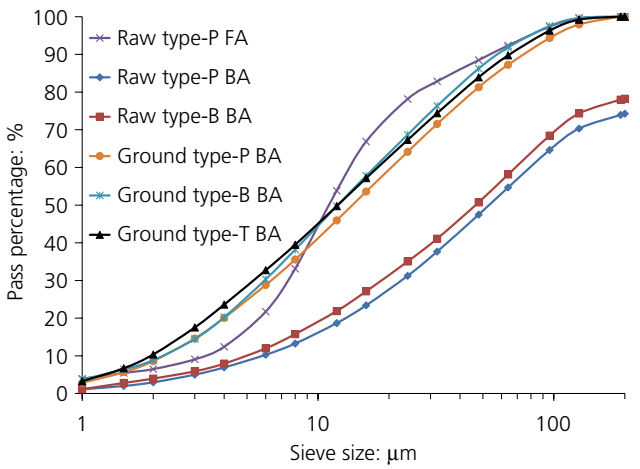

Figure 2. Particle size distributions of FA and furnace BA

Scanning electron microscopy analysis

Scanning electron microscopy images (Figure 3) were evaluated to investigate the microstructure of the raw coal ashes. Figure 3(a) shows that the FA particles appear to be spherical and of varying size. As reported previously (Kunjalukkal and Licciulli, 2014), these tiny spheres are known as cenospheres and have perfectly rounded and intact shapes. In addition, the micrograph shows that there are no evidently visible pores in the microstructure of the FA particles. SEM micrographs of the three types of raw BA are shown in Figures 3(b)–3(d). When compared with the SEM micrograph of the FA under the same magnification (i.e. 5000×), the micrographs of the BAs show that the BA particles were significantly larger and angular, with plenty of irregular fragments and only a small amount of semi-spheres. Some pores are also visible in the microstructure of the BAs. These findings are in agreement with previously reported microstructural observations of BA (Chindaprasirt *et al.*, 2009; Kunjalukkal and Licciulli, 2014). Some foreign objects were also observed in the microstructure of the BA samples, such as the rectangular-shaped object shown in Figure 3(b). A composition test undertaken indicated that this object was primarily radium, a radioactive earth-metal found in uranium ores. No foreign objects or impurities were observed in the SEM images of the FA samples. These observations clearly indicate that the furnace BA contained more impurities than the FA, and this can be explained by the fact that BA is extracted from the base of a furnace where larger and foreign objects can fall and accumulate.

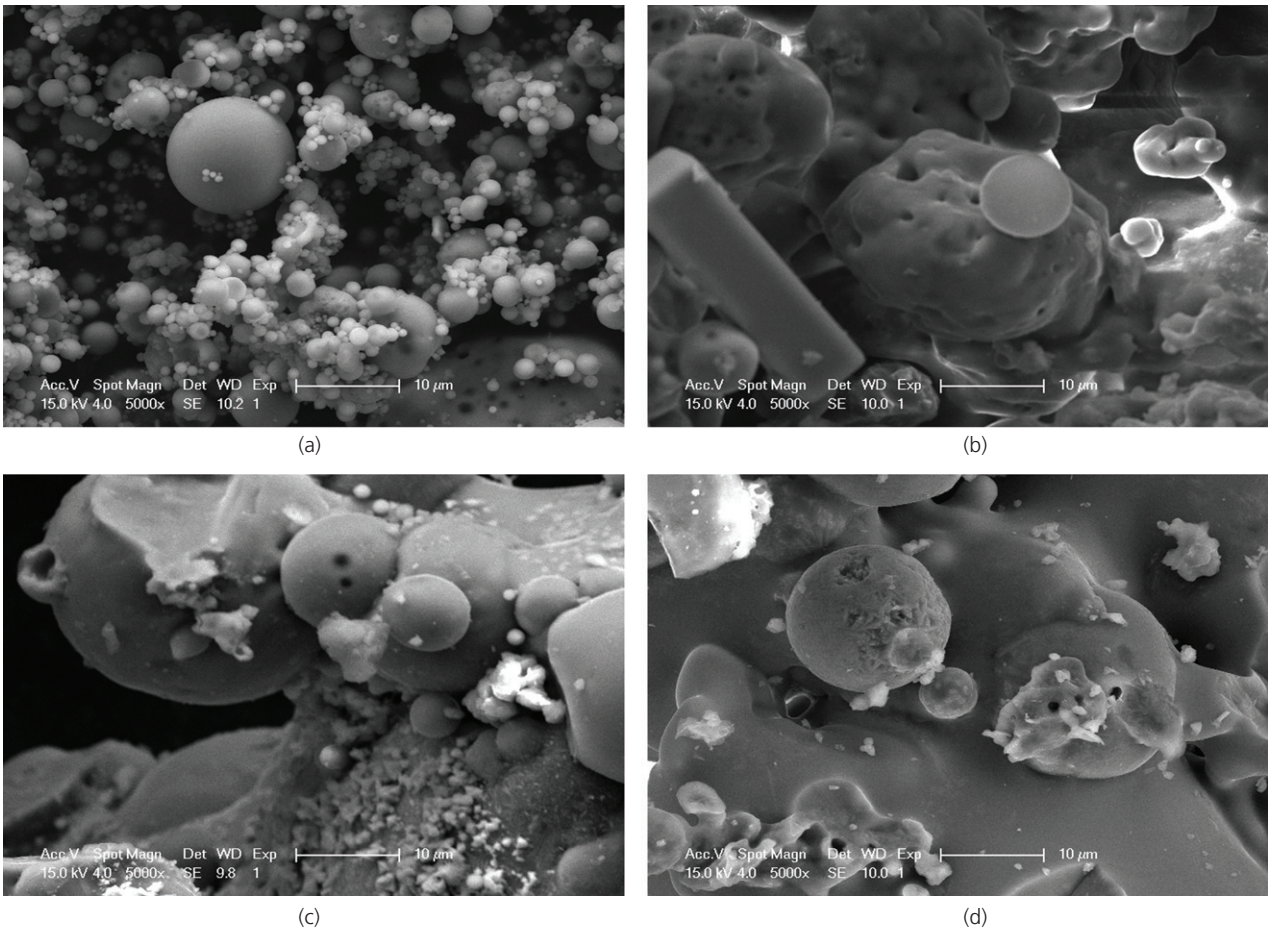

Figure 3. SEM images of as-received coal ashes (5000× magnification): (a) type-P FA; (b) type-P furnace BA; (c) type-B furnace BA; (d) type-T furnace BA

The SEM micrographs of the milled BAs are shown in Figures 4(a)–4(c). Comparing these with the SEM images of the as-received BAs shown in Figures 3(b) and 3(c) indicates that milling of the BA significantly reduced the number of large particles, and helped break the agglomerations seen in the raw BAs. However, some large particles were still present after milling. As shown in Figure 2, the PSDs of the BAs became closer to that of the raw FA after milling. However, comparison of the micrographs of the as-received FA with images of the milled BAs indicates that the milled BAs contained larger and more angular particles and plenty of and pores and cavities were present.

Observations of GPCs during curing

Workability

The workability of each batch of GPC was obtained through slump tests performed in accordance with ASTM C143/C143M (ASTM, 2012b). The slump test results are summarised in Table 1, which shows that the workability of the FA- and BA-based GPCs increased with an increase in *l*/*b* ratio. This observation is in general agreement with previously reported results on coal-ash-based geopolymers (Chindaprasirt and Rattanasak, 2010; Sathonsaowaphak *et al*., 2009) and can be explained by the fact that, with an increase in fluid medium content, the interactions among the coal ash particles decrease with an increase in interparticle distance, which in turn results in lower interference among those particles. Furthermore, the slump values shown in Table 1 indicate that the workability of the FA- and BA-based GPCs increased with a decrease in the concentration of the sodium hydroxide solution used in the alkaline liquid activator. This observation is in agreement with other works (Chindaprasirt and Rattanasak, 2010; Chindaprasirt *et al*., 2007) and can be explained by the fact that the viscosity of alkaline activator liquid generally increases with an increase in concentration of the sodium hydroxide solution, which in turn reduces the workability of concrete. In addition, the slump values in Table 1 show that milling the

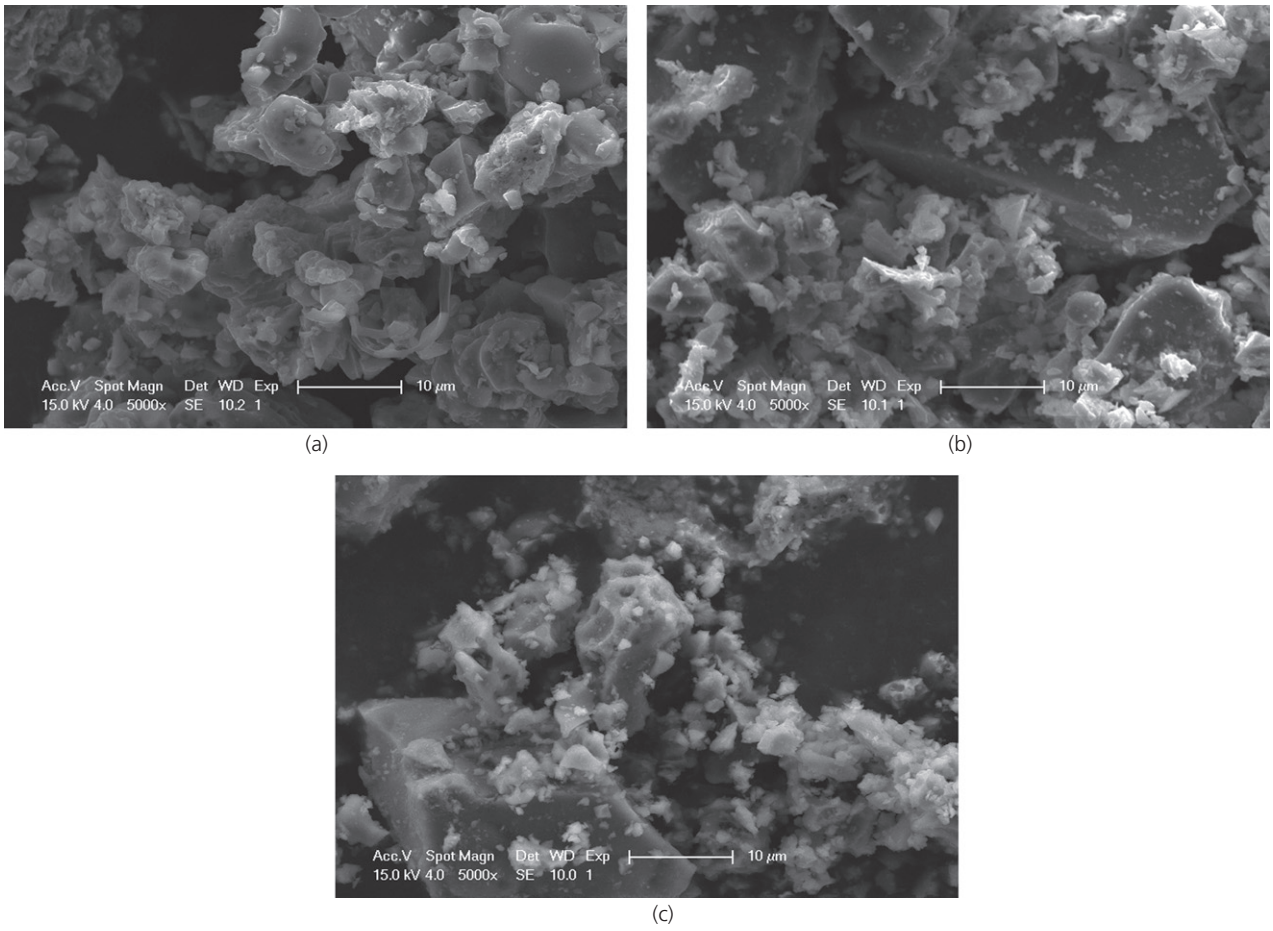

Figure 4. SEM images of furnace BAs after 3 min grinding (5000× magnification): (a) type-P BA; (b) type-B BA; (c) type-T BA

FA adversely affected the workability of the FA-based concretes. This reduction in workability is attributable to the change in shape of FA particles from spherical to angular due to milling, which leads to a reduced 'ball-bearing effect' (Temuujin *et al.*, 2009b). Conversely, milling of the BAs resulted in significant improvements to the workability of BA-based GPCs. This observation can be explained by the fact that milling reduced the amount of pores inside the BA particles, which in turn resulted in lower liquid absorption of these particles during the mixing process. Moreover, as shown in Table 1, the workability of the FA-based GPCs was much higher than that of the BA-based GPCs. This observation indicates that the spherical particle shape and smooth surface of the FA provide significant ball-bearing effects, as has also been noted previously (Bai *et al.*, 2004; Malhotra, 2002; Temuujin *et al.*, 2009b), which translates into improved workability. Furthermore, as shown in Figure 5, numerous small balls of wet paste were formed during the mixing process of some of the BA-based GPC mixes. This can be attributed to insufficient liquid content as a result of the higher absorption capacity of BAs. In order to attain workable mixes, some polycarboxylic ether polymer based superplasticiser was subsequently added to the GPC mixes that exhibited low slump values, as noted in Table 1.

Efflorescence

Previous research has established that efflorescence is detrimental to the durability and mechanical properties of geopolymer materials as it consumes residual alkalis (Huang *et al.*, 2012; Pandey *et al.*, 2012; Temuujin *et al.*, 2010; Williams and Van Riessen, 2010). It is well known that efflorescence formation in GPC is mainly caused by the reaction of atmospheric carbon dioxide with residual soluble alkalis at the surface of resultant products of geopolymer binders when the concrete is exposed to humid air or contact with water occurs (Najafi *et al.*, 2012; Škvára *et al.*, 2009; Temuujin *et al.*, 2009a; Zhang *et al.*, 2014a).

The specimens used in the present study were cast and cured at ambient temperature and were exposed to air. Visible efflorescence (Figure 6) was observed in all but one specimen series (i.e. FPA14-0·25): this can be explained by the presence of a

Figure 5. Balls of wet paste formed during the mixing of BA-based GPC

higher amount of coal ash in this mix, which resulted in full utilisation of the alkaline solution during the geopolymerisation process.

Density

The hardened densities of the GPCs are reported in Table 1. The densities were established from concrete cylinders at 28 d of age. It is evident from the results given in Table 1 that, with an otherwise identical mix design, the BA-based GPCs exhibited significantly lower hardened densities than the FA-based GPCs. This can be attributed to the more porous structure and larger and more irregularly shaped particles of the BA, which results in a GPC with a less dense and homogeneous microstructure. This finding is in agreement with previous studies on GPCs (Chindaprasirt *et al.*, 2009; Kunjalukkal and Licciulli, 2014). The BA-based concrete contains a significant amount of residual liquid (i.e. water and alkaline solution) that remains in its structure after casting. This free liquid subsequently evaporates during the curing process, which results in significantly lower densities of the hardened concrete.

Influence of test parameters on observed behaviour

Compressive behaviour

Effect of coal ash milling

The influence of milling the coal ash on the compressive behaviour of GPCs can be studied through a comparison of the companion specimen series that were manufactured using either as-received or milled coal ashes. For the FA-based GPCs, this comparison was made between FPM14-0·5 and FPA14-0·5 GPC series, which were manufactured using as-received and milled FA respectively. The results in Table 3 show that series FPM14-0·5 gained significantly higher compressive strength (f'_c) than series FPA14-0·5. This finding is in agreement with previous work on coal-ash-based GPCs (Diaz *et al.*, 2010; Temuujin *et al.*, 2009b), where it was found that the compressive strength of GPCs increased with a decrease in FA particle size. Table 3 also shows that the milled FA-based GPCs had a higher modulus of elasticity (E_c) but lower peak axial strain (ε_{co}) compared with the companion GPCs manufactured with as-received FA.

Figure 6. Efflorescence in GPC

A comparison of the results of BA-based GPCs (i.e. BBM10-0·5 with BBA10-0·5 and BPM10-0·5 with BPA10-0·5) in Table 3 shows findings similar to those obtained from

Series	f'_c: MPa	E_c: GPa	ε_{co}: %
FPM10-0·5	34·4	29·7	0·19
FPM14-0·5	42·3	35·9	0·14
FPA14-0·5	18·8	11·0	0·26
FPA14-0·25	30·4	25·4	0·21
BPM10-0·5	7·6	5·8	0·33
BPA10-0·5	0·8	—	—
BPA14-0·5	0·6	—	—
BPA14-1·1	0·3	—	—
BBM10-0·5	13·5	8·1	0·30
BBA10-0·5	4·8	2·2	0·46
BTM10-0·5	2·5	0·4	0·57

Table 3. Summary of axial compression test results at concrete age of 28 d

FA-based GPCs. That is, the compressive strength of BA-based GPCs increased with a decrease in BA particle size as a result of milling. Comparison of the compressive strengths of BBM10-0·5 and BBA10-0·5 indicates that using milled type-B BA in the concrete mixes led to an approximately three-fold increase in compressive strength. An even more significant strength improvement was observed in the GPCs manufactured with milled type-P BA, with series BPM10-0·5 exhibiting a compressive strength around ten times higher than that of series BPA10-0·5. These findings can be explained by the fact that milling increases the surface area of the coal ash particles, which results in an improvement in the reactivity of the coal ash in the GPC mixes (Diaz *et al*., 2010; Sathonsaowaphak *et al*., 2009; Somna *et al*., 2011; Temuujin *et al*., 2009b). Furthermore, milled coal ash particles also contain less capillary pores than the as-received coal ash (Diaz *et al*., 2010; Temuujin *et al*., 2009b), resulting in reduced absorption of alkaline liquid during the mixing process, which in turn contributes to a higher compressive strength of the mix.

Effect of chemical composition of coal ash

The influence of the chemical composition of the coal ash on the compressive behaviour of the GPC was investigated through a comparison of the concretes manufactured using BA from different sources. As noted previously, the three types of BA (type P, B and T) were obtained from three different power stations but their milled products had nearly identical PSDs. The test results indicate that series BBM10-0·5 specimens manufactured with type-B BA exhibited a significantly higher compressive strength than the companion BPM10-0·5 series manufactured with type-P BA. As noted earlier in the paper and shown in Table 2, type-B and type-P BAs had comparable calcium oxide contents, but the type-B BA had a slightly higher silicon dioxide/aluminium oxide ratio than type-P BA. Silva *et al*. (2007) and Thokchom *et al*. (2012) also reported that the compressive strength of coal-ash-based GPC increases with an increase in the silicon dioxide/aluminium oxide ratio of the coal ash.

However, in contrast with the above observation, series BTM10-0·5, manufactured using type-T BA with the highest silicon dioxide content and the highest silicon dioxide/aluminium oxide ratio of all the BAs used, exhibited a lower compressive strength than the companion series BBM10-0·5 and BPM10-0·5. The significantly lower strength of the GPC manufactured with the type-T BA can be attributed to the extremely low calcium oxide content of the type-T BA (Table 2). Temuujin *et al*. (2009a) reported that the addition of calcium compounds to a coal-ash-based GPC mix can accelerate the dissolution of coal ashes, leading to a more homogeneous microstructure of the GPC and in turn resulting in an increase in compressive strength: they showed that the addition of calcium compounds up to 3% by weight of coal ash led to an approximate doubling of GPC compressive strength. It is believed, therefore, that the low calcium oxide content of the type-T BA adversely affected the compressive strength of the resulting concrete. Furthermore, the results of the present study suggest that the calcium oxide content of the BA has a much more pronounced influence on GPC compressive strength than the silicon dioxide/aluminium oxide ratio of the BA used.

Effect of alkaline liquid to ash ratio (*l*/*b*)

The influence of *l*/*b* ratio on the compressive behaviour of the coal-ash-based GPCs was also investigated. For the FA-based GPCs, it is evident from Table 3 that, at a given age, series FPA14-0·25 with a lower *l*/*b* ratio showed significantly higher compressive strength than the companion FPA14-0·5 series with a higher *l*/*b* ratio. Table 3 also shows that the concrete modulus of elasticity decreased and peak axial strain increased with an increase in *l*/*b* ratio. A similar relationship between axial compressive strength and *l*/*b* ratio was also observed for the BA-based GPCs: comparison of series BPA14-1·1 and BPA14-0·5 indicates that BA-based GPCs with a higher *l*/*b* ratio developed a lower compressive strength than the companion specimens with a lower *l*/*b* ratio. Due to restrictions of the testing apparatus it was not possible to measure the peak axial strains of series BPA14-1·1 and BPA14-0·5, with very low compressive strengths.

These findings (i.e. compressive strength decreases with an increase in *l*/*b* ratio) are in agreement with previous work on coal-ash-based GPCs (Hardjito and Jong, 2011; Sathonsaowaphak *et al*., 2009) and can be explained by the fact that an increase in *l*/*b* ratio leads to an increase in the water content of the reaction medium, thereby reducing friction between particles, which in turn results in a decrease in compressive strength and other mechanical properties of GPCs (Hardjito and Jong, 2011; Hardjito *et al*., 2004b; Nassar *et al*., 2013; Sathonsaowaphak *et al*., 2009; Wongpa *et al*., 2010).

Effect of coal ash type

To investigate the influence of coal ash type on the compressive behaviour of coal-ash-based GPCs, comparisons were conducted between series FPA14-0·5 and BPA14-0·5 and series FPM10-0·5 and BPM10-0·5: the specimens in each comparison pair had an identical mix proportion but were manufactured using either FA or BA supplied from the same source. Table 3 shows that series FPA14-0·5 and FPM10-0·5 both showed significantly higher compressive strengths than their BA-based counterparts. This observation is consistent with other reports (Chindaprasirt *et al*., 2009; Kunjalukka and Licciulli, 2014; Li *et al*., 2012) and can be explained by the fact that the degree of polymerisation in BA-based GPC is lower than that in FA-based GPC, resulting in a large number of unreacted BA particles remaining in the structure of the hardened concrete.

Effect of sodium hydroxide concentration

Companion specimens prepared using different concentrations of sodium hydroxide solutions were compared to study the influence of sodium hydroxide concentration on the compressive behaviour of coal-ash-based GPCs. Comparing the results of specimens FPM10-0·5 and FPM14-0·5 in Table 3, an increase in sodium hydroxide concentration led to an increase in compressive strength of the FA-based GPCs. Sodium hydroxide solution at a higher concentration can promote the leaching of silicon and aluminium from the coal ash particles into the solution and hence promote the reaction of the aluminosilicate source with the solution, resulting in improved compressive strength as was also noted previously (Hanjitsuwan *et al.*, 2014; Mishra *et al.*, 2008; Rattanasak and Chindaprasirt, 2009). However, no significant influence of sodium hydroxide concentration was seen on the compressive strengths of the companion BA-based GPCs (i.e. BPA10-0·5 and BPA14-0·5), with both groups exhibiting very low compressive strengths.

Variation of compressive strength with time

The variations of compressive strength of the GPCs with curing age are illustrated in Figure 7, and the relative increases in strengths are listed in Table 4. These results indicate that, unlike CEMI-based concretes, the compressive strengths of the ambiently cured coal-ash-based GPCs showed significant increases after a curing age of 28 d. This can be attributed to the low degree of geopolymerisation that takes place under ambient curing conditions (Geetha and Ramamurthy, 2013; Somna *et al.*, 2011; Temuujin *et al.*, 2009b), which results in ongoing chemical reactions of the significant amounts of residual raw materials (i.e. alkalis and coal ashes) that remain in the concrete after 28 d. Comparison of these results with those reported in the literature for heat-cured geopolymers

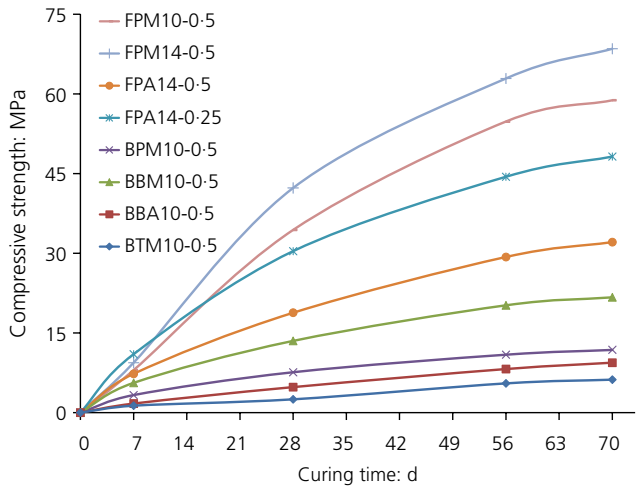

Figure 7. Variation of compressive strengths of GPCs with curing age

Series	Change in compressive strength: %		
	7 d to 28 d	28 d to 56 d	56 d to 70 d
FPM10-0·5	330	59	7
FPM14-0·5	350	49	9
FPA14-0·5	158	56	10
FPA14-0·25	176	46	9
BPM10-0·5	130	43	8
BPA10-0·5	100	75	14
BPA14-0·5	200	—	—
BPA14-1·1	—	100	83
BBM10-0·5	141	50	7
BBA10-0·5	182	71	15
BTM10-0·5	150	120	13

Table 4. Change in compressive strength with curing age

(Antunes *et al.*, 2013; Chen *et al.*, 2012; Chotetanorm *et al.*, 2012; Kim *et al.*, 2012) indicates that, compared with ambient curing, heat curing results in a significantly higher initial compressive strength, but a much less significant strength increase over time after 7 d. This can be explained by the fact that heat curing significantly accelerates the rate of geopolymerisation and the consumption of reactive materials. Influences of particle size, chemical composition and type of coal ash on variations in compressive strength over time are discussed in the remainder of this section.

As shown in Table 4, compared with the as-received FA-based GPC (i.e. FPA14-0·5), the milled FA-based GPC (i.e. FPM14-0·5) exhibited a more significant strength gain between the curing ages of 7 d and 28 d. On the other hand, a nearly identical level of strength change was observed in all FA-based GPCs after 28 d. A possible explanation for this is that the milled coal ash particles reacted with alkalis more rapidly during the earlier curing ages, resulting in a more significant strength gain of the concrete up to the age of 28 d. Beyond 28 d, the rate of reactions and the resulting strength gains of the milled coal-ash-based GPCs subsequently reduced and matched those of the companion as-received FA-based GPCs, once most of the milled and finer coal ash particles were fully consumed. Table 4 also indicates that the influence of milling was not as significant for BA-based GPCs during early curing (i.e. 7 d to 28 d), with the concretes prepared with as-received and milled BAs exhibiting similar increases in compressive strengths.

Table 4 also shows that no major difference was observed in the 7–28 d strength gains of series BPM10-0·5, BBM10-0·5 and BTM10-0·5 GPCs. However, during the curing ages of 28 d to 56 d, series BTM10-0·5 series showed a more pronounced strength gain than the other series. As discussed earlier, this can be attributed to the lower reactivity of the

type-T BA due to its lower calcium oxide content, resulting in a lower dissolution rate of the BA and in turn leading to an extended period of chemical reactions in the concrete beyond 28 d. Furthermore, comparison of the strength changes of the milled FA- and BA-based GPCs (i.e. FPM10-0·5 and BPM10-0·5) shows that the strength gain of the FA-based GPCs was more significant than that of the BA-based GPCs at 7–28 d. After 28 d, on the other hand, the FA- and BA-based GPCs exhibited similar changes in strengths. These observations can be explained by the higher reactivity of the FA particles, which results in a more significant strength gain in their concretes during the earlier curing ages. After consumption of the highly reactive particles beyond 28 d, the strength gains of the FA-based GPCs matched those of the companion BA-based GPCs.

Conclusions

The results of an experimental study on the behaviour of geopolymer concretes (GPCs) made with fly ash (FA) and furnace bottom ash (BA) cured at ambient temperature have been presented. The following conclusions are drawn from this study.

(*a*) The workability of coal-ash-based GPCs is strongly influenced by the liquid to binder (*l*/*b*) ratio, the concentration of sodium hydroxide solution and the type of coal ash. GPC mixes manufactured with a higher *l*/*b* ratio, a lower concentration of sodium hydroxide solution, and FA (instead of BA) exhibit better workability.

(*b*) Efflorescence of GPCs can be eliminated by increasing the coal ash content with respect to the activator solution.

(*c*) At a given curing age, otherwise identical GPCs manufactured using FA develop higher compressive strengths than GPCs produced using BA. The compressive strength of FA- and BA-based GPCs increases with a decrease in particle size of the coal ash used. Furthermore, GPCs manufactured using coal ashes with finer particles exhibit a higher modulus of elasticity but a lower peak axial strain.

(*d*) The compressive strengths of both FA- and BA-based GPCs increase with a decrease in *l*/*b* ratio. GPCs manufactured using a lower *l*/*b* ratio also exhibited a higher modulus of elasticity and a lower peak axial strain.

(*e*) An increase in the silicon dioxide/aluminium oxide ratio or calcium oxide content of the coal ash results in an increase in the compressive strength of the ash-based GPC.

(*f*) Within the range investigated in the present study, it was observed that an increase in sodium hydroxide concentration results in an increase in the compressive strength of FA-based GPCs.

(*g*) The compressive strength of ambiently cured coal-ash-based GPCs continues to increase after a concrete age of 28 d. GPCs manufactured using milled coal ash (instead of as-received coal ash) and FA (instead of BA) exhibited more significant compressive strength gains before the curing age of 28 d.

Acknowledgements

The authors extend their gratitude to Messrs Nguyen, Smith, Staniford and van Senden, who performed the experimental procedures presented in this paper. The authors also thank Adelaide Brighton Pty Ltd for their generous donation of the test materials used in the study reported here.

REFERENCES

Ahmaruzzaman M (2010) A review on the utilization of fly ash. *Progress in Energy and Combustion Science* **36(3)**: 327–363.

Antunes BS, Rozineide A, Bernardin AM, Riella HG and Kuhnen NC (2013) Geopolymer synthesized from bottom coal ash and calcined paper sludge. *Journal of Cleaner Production* **57**: 302–307.

Arellano-Aguilar R, Burciaga-Díaz O, Gorokhovsky A and Escalante-García JI (2014) Geopolymer mortars based on a low grade metakaolin: effects of the chemical composition, temperature and aggregate: binder ratio. *Construction and Building Materials* **50**: 642–648.

ASTM (2005) C39/C39M-05: Standard test method for compressive strength of cylindrical concrete specimens. ASTM, West Conshohocken, PA, USA.

ASTM (2012a) C618-12a: Standard specification for coal fly ash and raw or calcined natural pozzolan for use in concrete. ASTM, West Conshohocken, PA, USA.

ASTM (2012b) C143/C143M-12: Standard test method for slump of hydraulic-cement concrete. ASTM, West Conshohocken, PA, USA.

ASTM (2014) C469/C469M-14: Standard test method for static modulus of elasticity and Poisson's ratio of concrete in compression. ASTM, West Conshohocken, PA, USA.

Bai Y, Ibrahim R and Basheer PM (2004) Properties of lightweight concrete manufactured with fly ash, furnace bottom ash, and Lytag. In *Proceedings of International Workshop on Sustainable Development and Concrete Technology, Beijing, China*, pp. 77–88.

Boonserm K, Sata V, Pimraksa K and Chindaprasirt P (2012) Improved geopolymerization of bottom ash by incorporating fly ash and using waste gypsum as additive. *Cement and Concrete Composites* **34(7)**: 819–824.

Chen C, Li Q, Shen L and Zhai J (2012) Feasibility of manufacturing geopolymer bricks using circulating fluidized bed combustion bottom ash. *Environmental Technology* **33(11)**: 1313–1321.

Chindaprasirt P and Rattanasak U (2010) Utilization of blended fluidized bed combustion (FBC) ash and pulverized coal combustion (PCC) fly ash in geopolymer. *Waste Management* **30(4)**: 667–672.

Chindaprasirt P, Chareerat T and Sirivivatnanon V (2007) Workability and strength of coarse high calcium fly ash

geopolymer. *Cement and Concrete Composites* **29(3)**: 224–229.

Chindaprasirt P, Jaturapitakkul C, Chalee W and Rattanasak U (2009) Comparative study on the characteristics of fly ash and bottom ash geopolymers. *Waste Management* **29(2)**: 539–543.

Chindaprasirt P, Rattanasak U and Jaturapitakkul C (2011) Utilization of fly ash blends from pulverized coal and fluidized bed combustions in geopolymeric materials. *Cement and Concrete Composites* **33(1)**: 55–60.

Chotetanorm C, Chindaprasirt P, Sata V, Rukzon S and Sathonsaowaphak A (2012) High-calcium bottom ash geopolymer: sorptivity, pore size, and resistance to sodium sulfate attack. *Journal of Materials in Civil Engineering* **25(1)**: 105–111.

Cwirzen A, Engblom R, Punkki J and Habermehl-Cwirzen K (2014) Effects of curing: comparison of optimised alkali-activated PC-FA-BFS and PC concretes. *Magazine of Concrete Research* **66(6)**: 315–323.

Davidovits J (1979) *SPE PATEC '79*. Society of Plastic Engineering, Brookfield Center, OH, USA, pp. 151–154.

Davidovits J (1991) Geopolymers. *Journal of Thermal Analysis and Calorimetry* **37(8)**: 1633–1656.

Davidovits J (1999) Chemistry of geopolymeric systems, terminology. *Proceedings of 2nd International Conference. Geopolymere '99, Saint Quentin, France* **99**: 9–40.

Diaz EI, Allouche EN and Eklund S (2010) Factors affecting the suitability of fly ash as source material for geopolymers. *Fuel* **89(5)**: 992–996.

Duxson P, Provis JL, Lukey GC and Van Deventer JSJ (2007) The role of inorganic polymer technology in the development of 'green concrete'. *Cement and Concrete Research* **37(12)**: 1590–1597.

Ferreira LFB, Costa HSS, Barata IIA *et al.* (2013) Precast alkali-activated concrete towards sustainable construction. *Magazine of Concrete Research* **66(12)**: 618–626.

Fu X, Li Q, Zhai J, Sheng G and Li F (2008) The physical–chemical characterization of mechanically-treated CFBC fly ash. *Cement and Concrete Composites* **30(3)**: 220–226.

Geetha S and Ramamurthy K (2013) Properties of geopolymerised low-calcium bottom ash aggregate cured at ambient temperature. *Cement and Concrete Composites* **43**: 20–30.

Guo X, Shi H and Dick WA (2010) Compressive strength and microstructural characteristics of class C fly ash geopolymer. *Cement and Concrete Composites* **32(2)**: 142–147.

Habert G, D'Espinose de Lacaillerie JB and Roussel N (2011) An environmental evaluation of geopolymer based concrete production: reviewing current research trends. *Journal of Cleaner Production* **19(11)**: 1229–1238.

Hanjitsuwan S, Hunpratub S, Thongbai P *et al.* (2014) Effects of NaOH concentrations on physical and electrical properties of high calcium fly ash geopolymer paste. *Cement and Concrete Composites* **45**: 9–14.

Hardjito D and Jong V (2011) *The Use of Fly Ash and Bottom Ash in Geopolymer Mortar*. Doctoral dissertation, Petra Christian University, Surabaya, Indonesia.

Hardjito D and Rangan BV (2005) *Development and Properties of Low-calcium Fly Ash-based Geopolymer Concrete*. Curtin University of Technology, Perth, Australia.

Hardjito D, Wallah SE, Sumajouw DMJ and Rangan BV (2004a) Brief review of development of geopolymer concrete. In *8th CANMET/ACI International Conference on Fly Ash, Silica Fume, Slag and Natural Pozzolans in Concrete, Las Vegas, USA*.

Hardjito D, Wallah SE, Sumajouw DM and Rangan BV (2004b) On the development of fly ash-based geopolymer concrete. *ACI Materials Journal* **101(6)**: 467–472.

Huang Y, Han M and Yi R (2012) Microstructure and properties of fly ash-based geopolymeric material with 5A zeolite as a filler. *Construction and Building Materials* **33**: 84–89.

Khale D and Chaudhary R (2007) Mechanism of geopolymerization and factors influencing its development: a review. *Journal of Materials Science* **42(3)**: 729–746.

Kiattikomol K, Jaturapitakkul C, Songpiriyakij S and Chutubtim S (2001) A study of ground coarse fly ashes with different finenesses from various sources as pozzolanic materials. *Cement and Concrete Composites* **23(4)**: 335–343.

Kim SH, Ryu GS, Koh KT and Lee JH (2012) Flowability and strength development characteristics of bottom ash based geopolymer. *World Academy of Science, Engineering and Technology* **70**: 53–59.

Kong DL, Sanjayan JG and Sagoe-Crentsil K (2007) Comparative performance of geopolymers made with metakaolin and fly ash after exposure to elevated temperatures. *Cement and Concrete Research* **37(12)**: 1583–1589.

Kovalchuk G, Fernández-Jiménez A and Palomo A (2007) Alkali-activated fly ash: effect of thermal curing conditions on mechanical and microstructural development – Part II. *Fuel* **86(3)**: 315–322.

Kumar S and Kumar R (2011) Mechanical activation of fly ash: effect on reaction, structure and properties of resulting geopolymer. *Ceramics International* **37(2)**: 533–541.

Kunjalukkal PS and Licciulli A (2014) Synthesis and characteristics of fly ash and bottom ash based geopolymers – a comparative study. *Ceramics International* **40(2)**: 2965–2971.

Li Q, Xu H, Li F *et al.* (2012) Synthesis of geopolymer composites from blends of CFBC fly and bottom ashes. *Fuel* **97**: 366–372.

Malhotra VM (2002) Sustainability – introduction: sustainable development and concrete technology – some goals of ACI's board task group on sustainable development. *Concrete International – Design and Construction* **24(7)**: 22.

Mathew MBJ, Sudhakar MM and Natarajan C (2013) Strength, economic and sustainability characteristics of coal ash–GGBS based geopolymer concrete. *International Journal of Computational Engineering Research* **3(1)**: 207–212.

Meyer C (2009) The greening of the concrete industry. *Cement and Concrete Composites* **31(8)**: 601–605.

Mishra A, Choudhary D, Jain N *et al.* (2008) Effect of concentration of alkaline liquid and curing time on strength and water absorption of geopolymer concrete. *ARPN Journal of Engineering and Applied Sciences* **3(1)**: 14–18.

Najafi KE, Allahverdi A and Provis JL (2012) Efflorescence control in geopolymer binders based on natural pozzolan. *Cement and Concrete Composites* **34(1)**: 25–33.

Nassar RUD, Soroushian P and Ghebrab T (2013) Field investigation of high-volume fly ash pavement concrete. *Resources, Conservation and Recycling* **73**: 78–85.

Pacheco-Torgal F, Castro-Gomes J and Jalali S (2008) Alkali-activated binders: a review: part 1. Historical background, terminology, reaction mechanisms and hydration products. *Construction and Building Materials* **22(7)**: 1305–1314.

Pacheco-Torgal F, Moura D, Ding Y and Jalali S (2011) Composition, strength and workability of alkali-activated metakaolin based mortars. *Construction and Building Materials* **25(9)**: 3732–3745.

Palomo A and Glasser FP (1992) Chemically-bonded cementitious materials based on metakaolin. *British Ceramic Transactions and Journal* **91(4)**: 107–112.

Pan Z, Sanjayan JG and Rangan BV (2011) Fracture properties of geopolymer paste and concrete. *Magazine of Concrete Research* **63(10)**: 763–771.

Pandey B, Kinrade SD and Catalan LJ (2012) Effects of carbonation on the leachability and compressive strength of cement-solidified and geopolymer-solidified synthetic metal wastes. *Journal of Environmental Management* **101**: 59–67.

Rattanasak U and Chindaprasirt P (2009) Influence of NaOH solution on the synthesis of fly ash geopolymer. *Minerals Engineering* **22(12)**: 1073–1078.

Reed M, Lokuge W and Karunasena W (2014) Fibre-reinforced geopolymer concrete with ambient curing for in situ applications. *Journal of Materials Science* **49(12)**: 4297–4304.

Ryu GS, Lee YB, Koh KT and Chung YS (2013) The mechanical properties of fly ash-based geopolymer concrete with alkaline activators. *Construction and Building Materials* **47**: 409–418.

Sata V, Sathonsaowaphak A and Chindaprasirt P (2012) Resistance of lignite bottom ash geopolymer mortar to sulfate and sulfuric acid attack. *Cement and Concrete Composites* **34(5)**: 700–708.

Sathonsaowaphak A, Chindaprasirt P and Pimraksa K (2009) Workability and strength of lignite bottom ash geopolymer mortar. *Journal of Hazardous Materials* **168(1)**: 44–50.

Shi XS, Collins FG, Zhao XL and Wang QY (2012) Mechanical properties and microstructure analysis of fly ash geopolymeric recycled concrete. *Journal of Hazardous Materials* **237**: 20–29.

Silva PD, Sagoe-Crenstil K and Sirivivatnanon V (2007) Kinetics of geopolymerization: role of Al_2O_3 and SiO_2. *Cement and Concrete Research* **37(4)**: 512–518.

Sinha DK, Kumar A and Kumar S (2014) Development of geopolymer concrete from fly ash and bottom ash mixture. *Transactions of the Indian Ceramic Society* **73(2)**: 143–148.

Škvára F, Kopecký L, Myšková L *et al.* (2009) Aluminosilicate polymers–influence of elevated temperatures, efflorescence. *Ceramics Silikáty* **53(4)**: 276–282.

Slavik R, Bednarik V, Vondruska M and Nemec A (2008) Preparation of geopolymer from fluidized bed combustion bottom ash. *Journal of Materials Processing Technology* **200(1)**: 265–270.

Somna K, Jaturapitakkul C, Kajitvichyanukul P and Chindaprasirt P (2011) NaOH-activated ground fly ash geopolymer cured at ambient temperature. *Fuel* **90(6)**: 2118–2124.

Temuujin J, Van Riessen A and Williams R (2009a) Influence of calcium compounds on the mechanical properties of fly ash geopolymer pastes. *Journal of Hazardous Materials* **167(1)**: 82–88.

Temuujin J, Williams RP and Van Riessen A (2009b) Effect of mechanical activation of fly ash on the properties of geopolymer cured at ambient temperature. *Journal of Materials Processing Technology* **209(12)**: 5276–5280.

Temuujin J, van Riessen A and MacKenzie KJD (2010) Preparation and characterisation of fly ash based geopolymer mortars. *Construction and Building Materials* **24(10)**: 1906–1910.

Thokchom S, Mandal KK and Ghosh S (2012) Effect of Si/Al ratio on performance of fly ash geopolymers at elevated temperature. *Arabian Journal for Science and Engineering* **37(4)**: 977–989.

Topçu IB and Toprak MU (2011) Properties of geopolymer from circulating fluidized bed combustion coal bottom ash. *Materials Science and Engineering A* **528(3)**: 1472–1477.

Topçu İB, Toprak MU and Uygunoğlu T (2014) Durability and microstructure characteristics of alkali activated coal bottom ash geopolymer cement. *Journal of Cleaner Production* **81**: 211–217.

Van Jaarsveld JGS, Van Deventer JSJ and Lorenzen L (1997) The potential use of geopolymeric materials to immobilise toxic metals: part I. Theory and applications. *Minerals Engineering* **10(7)**: 659–669.

Van Jaarsveld JGS, Van Deventer JSJ and Lukey GC (2002) The effect of composition and temperature on the properties of fly ash-and kaolinite-based geopolymers. *Chemical Engineering Journal* **89(1)**: 63–73.

Wallah SE and Rangan BV (2006) *Low-calcium Fly Ash-based Geopolymer Concrete: Long-term Properties*. Curtin University, Perth, Australia, Research report GC2, pp. 76–80.

Williams RP and Van Riessen A (2010) Determination of the reactive component of fly ashes for geopolymer production using XRF and XRD. *Fuel* **89(12)**: 3683–3692.

Wongpa J, Kiattikomol K, Jaturapitakkul C and Chindaprasirt P (2010) Compressive strength, modulus of elasticity, and water permeability of inorganic polymer concrete. *Materials and Design* **31(10)**: 4748–4754.

Xu H, Li Q, Shen L, Wang W and Zhai J (2010) Synthesis of thermostable geopolymer from circulating fluidized bed combustion (CFBC) bottom ashes. *Journal of Hazardous Materials* **175(1)**: 198–204.

Zhang M, El-Korchi T, Zhang G, Liang J and Tao M (2014a) Synthesis factors affecting mechanical properties, microstructure, and chemical composition of red mud–fly ash based geopolymers. *Fuel* **134**: 315–325.

Zhang Z, Provis JL, Reid A and Wang H (2014b) Fly ash-based geopolymers: the relationship between composition, pore structure and efflorescence. *Cement and Concrete Research* **64**: 30–41.

JOURNAL ARTICLE 3

THIS PAGE HAS BEEN LEFT INTENTIONALLY BLANK

Statement of Authorship

Title of Paper	Influence of Recycled Aggregate Size and Content on Behavior of Recycled Aggregate Concrete
Publication Status	☐ Published ☐ Accepted for Publication ☑ Submitted for Publication ☐ Publication Style
Publication Details	Journal of Cleaner Production, (tentatively accepted subject to final revisions).

Author Contributions

Name of Principal Author (Candidate)	Tianyu Xie		
Contribution to the Paper	Design of experimental tests, manufacture and laboratory testing of specimens, analysis of test results, and preparation of manuscript		
Signature		Date	2/9/2015

Name of Co-Author	Dr Togay Ozbakkaloglu		
Contribution to the Paper	Design of experimental tests, supervision of experimental tests, and review of manuscript		
Signature		Date	2/9/2015

Influence of Recycled Aggregate Size and Content on Behavior of Recycled Aggregate Concrete

Tianyu Xie[1] and Togay Ozbakkaloglu[2]

ABSTRACT

Over the past two decades, recycled concrete aggregate (RCA), which is obtained by crushing of old concrete elements from construction and demolition (C&D) waste, has been considered as an alternative aggregate material for use in structural concrete with the aim of achieving resource sustainability in construction industry. It is now recognized that the application of RCA as coarse aggregate to form recycled aggregate concrete (RAC) is a highly attractive and promising technology for conserving natural resources and reducing the environmental impact of the construction industry. This paper presents an experimental study that investigated the mechanical and durability-related properties of concretes manufactured with RCAs of different sizes and contents. A total of 14 batches of RACs were manufactured. Tests were undertaken to establish the compressive strength, elastic modulus, flexural strength, splitting tensile strength, workability, drying shrinkage and water absorption of each batch. Test parameters included the RCA replacement ratio, size of coarse aggregates and mixing method used in the preparation of concrete. The results indicate that the compressive strength is not the only decisive factor on mechanical and durability-related properties of RACs. It is seen that the size and content of recycled aggregates significantly affect the mechanical and durability-related properties of RACs.

Keywords: Recycled concrete aggregate (RCA); Recycled aggregate concrete (RAC); Compressive strength; Mechanical properties; Shrinkage; Water absorption.

[1] MPhil Candidate, School of Civil, Environmental and Mining Engineering, University of Adelaide, Australia.

[2] (Corresponding author) Senior Lecturer, School of Civil, Environmental and Mining Engineering, University of Adelaide, Australia. Tel : +618 8313 6477; Fax : +618 8313 4359; Email: togay.ozbakkaloglu@adelaide.edu.au

INTRODUCTION

Concrete is by far the most widely used construction material. In recent decades, the rapid increase in the rate of industrialization and urbanization due to parallel growths in economy and population has led to a great worldwide demand for concrete. Natural aggregates (NA), including both the coarse and fine grades, constitute around 70% of total concrete volume in a concrete mix. According to current estimates, the global demand for construction aggregates is over 20 billion tons per annum (Behera et al., 2014; Çakır 2014; Sonawane and Pimplikar, 2013). The increased use of concrete thereby leads to the depletion of the natural aggregates as well as to the consumption of large amounts of energy on the production, transportation and use of raw materials (Mefteh et al., 2013; Radonjanin et al., 2013). Meanwhile, the growth in the rate of demolition of old structures, as prompted by the limited availability of new construction sites, have resulted in generation of large amounts of construction and demolition (C&D) wastes. These C&D wastes, as the largest waste streams of solid waste in most of countries, are commonly and ineffectively disposed of in landfills at a significant cost, while also resulting in the depletion of landfill space, as was discussed in a number of recent studies on utilization of C&D wastes (Behera et al., 2014; Dilbas et al., 2014; Medina et al., 2014; Rodrigues et al., 2013; Torgal and Jalali, 2011; Tošić et al., 2015). For the conservation of natural resources and minimizing the impact of C&D waste on the environment, recycled concrete aggregate (RCA), which is obtained from C&D wastes, has been considered as an alternative aggregate in structural concrete over the past two decades. However, due to concerns regarding the inferior quality of RCA compared to that of NA, the use of RAC in construction industry as structural concrete remains limited.

RCA is a type of granular material created by crushing of old concrete elements sourced from C&D wastes. Recycled aggregate concrete (RAC) is produced with partially or fully substitution of NAs by RCAs in the concrete mix. To date, a significant volume of studies have been reported in the literature on the behavior of RACs. These studies have shown that RAC has a great potential to be a feasible alternative to natural aggregate concrete (NAC) in the construction industry. However, when compared with companion NACs, RACs manufactured with full replacement of NAs by RACs exhibit around 20 to 30% lower compressive strengths (Abd Elhakam et al., 2012; Barbudo et al., 2013; Limbachiya et al., 2012a; Limbachiya et al., 2012b; Mas et al., 2012; Sheen et al., 2013), 30 to 50% lower elastic moduli (Ajdukiewicz and Kliszczewicz, 2002; Beltrán et al., 2014; Kwan et al., 2012; Radonjanin et al., 2010; Rahal, 2007; Rao et al., 2007; Rao et al., 2011; Yang et al., 2008), up to 23% lower splitting tensile strengths (Katz, 2003; Kou et al., 2007; Kou et al., 2008; Kou et al., 2009; Tabsh and Abdelfatah, 2009; Yang et al., 2008), and 10% to 13% lower flexural strengths (i.e. Ajdukiewicz and Kliszczewicz, 2007; Bairagi et al., 1990; Kheder and Al-Windawi, 2005; Kou et al., 2008; Mefteh et al., 2013; Thomas et al., 2013). As reported in a recent review study (Behera et al., 2014), there are technologies available that can help enhance the quality of RACs. These include the addition of pozzolanic materials to the RAC mix and using slightly different concrete mixing methods. Tam et.al (2005) introduced a new mixing approach namely, two stage mixing approach (TSMA) and have shown that, compared to the conventional mixing approach (NMA), TSMA can significantly enhance mortar-RCA bond, resulting in improvements in both long- and short-term properties of RACs.

In the majority of the concrete design codes and standards (i.e. (ACI318, 2009; AS3600, 2009; BS, 1997)) compressive strength is used to predict the other mechanical properties (i.e.

modulus of elasticity, flexural strength and splitting tensile strength) of NACs. Therefore, the compressive strength of concrete is considered as the key indicator of mechanical properties of conventional concrete. As was previously shown experimentally (Ajdukiewicz and Kliszczewicz, 2002; Barbudo et al., 2013; Marie and Quiasrawi, 2012, Topcu, 1997), the compressive strength of RACs is generally lower than that of the companion NACs prepared using the same concrete mix proportions. Therefore, to maintain the same compressive strength between RAC and NAC, adjustments to the concrete mix proportions based on both the quality and quantity of RCAs are required. However, as revealed by a careful review of the existing literature on RACs, only a limited number of studies have been reported to date on the relative behavior of concretes of the same compressive strength prepared using different coarse RCA contents (Beltrán et al., 2014; Butler et al., 2013; Etxeberria et al., 2007; Limbachiya et al., 2000). These studies have indicated that there might be significant differences between the mechanical and durability-related properties of RACs and NACs having the same compressive strength. However, these studies on the relative performance of RACs and NACs of the compressive strength investigated only a limited numbers of parameters (i.e. RCA replacement ratio, aggregate to cement ratio), and no study to date has investigated the influence of particle size of coarse aggregate on the behavior of concretes of the same compressive strength that were prepared with different amounts of RCAs. The particle size of coarse aggregate is known to be an influential parameter for the behavior of NACs and has been widely studied previously (Akçaoğlu et al., 2002; Elices and Rocco, 2008; Miled et al., 2012; Sim et al., 2013; Tumidajski and Gong, 2006). Therefore, understanding the influence of coarse aggregate particle size on the behavior of RACs and NACs of the same compressive strength is of significant interest.

Moreover, the popularity of higher strength concretes in the construction industry has been currently on a steady incline due to the superior performance and economy offered by high-strength concrete (HSC) over normal-strength concrete (NSC) in a large number of structural engineering applications. However, to date, only two studies have investigated the behavior of high-strength RAC and NAC of the same compressive strength (Butler et al., 2013; Limbachiya et al., 2000). This demonstrates the need for additional experimental studies on HSCs that are manufactured using different RCA replacement ratios.

As the first experimental study reported to date on the behavior of concretes of the same compressive strength prepared with coarse RCAs of different sizes and contents, the study presented in this paper was aimed at investigating the variation of mechanical- and durability-related properties of concrete with the size and replacement ratio of RCAs. The paper initially provides a summary of the experimental program, including material properties, specimen properties and testing procedures. Following this, the results of the experimental program are presented. Finally, a detailed discussion on the results of the experimental study is provided, where the influences of RCA replacement ratio, particle size of coarse RCA and mixing method of concrete are presented along with other key experimental observations.

TEST PROGRAM

Test specimens

A total of 14 unique batches of concrete, including 3 batches of NAC and 11 batches of RAC, were manufactured in the present study. A series of tests were undertaken on each batch to establish the properties of the fresh and hardened concrete, including workability, compressive strength, modulus of elasticity, flexural strength, splitting tensile strength, drying shrinkage and water absorption. Three types of specimens were used in specimen

testing, namely, beams, prisms, and cylinders. The beam specimens were used for flexural strength tests and they were 100 mm in width, 100 mm in depth and 500 mm in length. The compressive strengths and moduli of elasticity of the concretes were established by the compression tests using cylinder specimens with 100 mm diameter and 200 mm height. The splitting tensile strength tests were conducted on larger cylinder specimens with 150 mm diameter and 300 mm height. To monitor the drying shrinkages of the concrete, prism specimens which were 75 mm in width, 75 mm in depth and 285 mm in length, were used. The test parameters included: RCA replacement ratio (*RCA %)*, maximum nominal aggregate size of RCA (*Φ*), and concrete mixing method (i.e. either NMA or TSMA). Three nominally identical specimens were tested for each unique specimen configuration in every type of test.

Recycled concrete aggregate (RCA)

The RCAs used in the present study were supplied by Adelaide Recycled Resource (ARR) in South Australia, which were produced by initially removing impurities from C&D wastes and subsequently crushing the demolition concrete using a jaw crusher and sieving it to separate the crushed concrete into different grades. As Figs.1 (a) and (b) illustrate, two different grades of coarse RCAs, including a finer RCA with 7-mm nominal maximum size (*Φ*) and a larger RCA with 12-mm nominal maximum size (*Φ*), were selected to study the influence of RCA particle size on the mechanical and durability-related properties of RACs. These RCAs were added at different RCA volume replacement ratios (*RCA %*) of 0, 25, 50 and 100 to represent NAC and concrete contained low, moderate and high amounts of RCAs, respectively. The physical properties of both grades of RCAs are given in Table 1. All coarse RCAs were initially washed to remove the impurities, and then pre-oven dried for 24 hours at 105˚C and subsequently cooled at ambient temperature for more than 3 hours before the mixing of the concrete.

Natural aggregate (NA)

The coarse NAs of the present study were crushed bluestone gravel and sourced from McLaren Vale Quarry (Fleurieu Peninsula). To maintain consistency in the coarse aggregate size of RAC and conventional concrete mixes, two grades of NAs with similar particle sizes to those of their companion RACs (i.e. 7 mm and 12 mm nominal maximum sizes) were selected. Figures 1 (c) and (d) illustrate these two types of coarse NAs. The physical properties of the coarse NAs are given in Table 1. All natural coarse aggregates were also pre-oven dried for 24 hours at 105˚C and subsequently cooled at ambient temperature for more than 3 hours before the mixing of the concrete. The natural sand with a maximum nominal size of 0.4 mm was supplied from Price Pit (Yorke Peninsula) and used as the fine aggregate for all concrete mixes. The physical properties of natural sand are also given in Table 1.

Cementitious binder

Two types of cementitious binder materials were used in this study, namely ordinary Portland cement and silica fume. The chemical compositions and physical properties of these binders are supplied in Table 2.

Mix designs and specimen preparation

As shown in Table 3, eleven of the 14 concrete mixes prepared in the present study were mixed by TSMA and designed to have different water-to-binder ratios (*w/b*), RCA replacement ratios (*RCA%*), and coarse aggregates grades. Through proper adjustments of the selected parameters in mix proportions of the concrete, an equivalent 28-day compressive strength (f'_c) of 40 MPa for NSC and 85 MPa for HSC were achieved. The remaining three

100% RCA-based concrete mixes were manufactured using the same concrete mix proportions as their companion RACs but a different mixing method (i.e. NMA). In Table 3, the term 'water-effective' is defined as the amount of water that was available for reaction with binder material. The 'water-total' reported in Table 3 was the total water added to each mix, and it consisted of the effective water and saturation water that was absorbed by fine and coarse aggregates. The effective *w/b* and total *w/b* ratios given in Table 3 were calculated based on the effective and total water amounts for each mix, respectively.

In the preparation of the RACs mixed using NMA, all the dry materials including the fine and coarse aggregates and binder (i.e. Portland cement and silica fume) were initially mixed in an 80-L capacity rotating pan mixer with fixed blades for approximately three minutes. Subsequently, the total amount of required water was gradually added to the mix and wet mixing continued for approximately five minutes to form the concrete. For the RACs prepared using TSMA, the fine and coarse aggregates were initially dry-mixed for 3 minutes and the water that saturated the fine and coarse aggregates together with one-half of the effective water was then added to the mix and the mixing continued for an additional 3 minutes. The binder was subsequently added to the mix and the mixing continued for 2 more minutes to finish the first stage of TSMA. In the second stage, the second half of the effective water was added together with a polycarboxylic ether polymer-based superplasticiser and the wet mixing continued for approximately five minutes to form the concrete. Gentle external vibration was used throughout the pouring processes of all concrete mixes to ensure proper placement of concrete.

Specimen designation

The concrete series in Tables 3 and 4 were labelled as follows: the letters N and H were used to label the normal-strength and high-strength concrete mix, respectively. The following letter was used to represent the coarse aggregate grade used in each mix, either C (for coarser aggregate) or F (for finer aggregate). This was followed by a number that indicated the replacement ratio of RAC to NA in the concrete. Finally, the last letters in the specimen designation was used to make a distinction between the mixes manufactured using different mixing methods, either TSMA (T) or NMA (N). For instance, NF-100-T is a normal strength RAC mix that contained smaller coarse aggregates with a RCA replacement ratio of 100%, which was prepared using the two-stage mixing approach.

Instrumentation and testing

The mechanical properties, including: compressive strength, modulus of elasticity, flexural strength and splitting tensile strength of concrete were tested using a universal testing machine in the Materials Laboratory of the University of Adelaide. Prior to the compression tests, all cylinder specimens were ground to ensure uniform distribution of the applied load at specimen ends. The drying shrinkage of all specimens was monitored up to 70 days of concrete age through the measurement of shrinkage strains.

TEST RESULTS AND EXPERIMENTAL OBSERVATIONS

Physical properties of RCAs and NAs

Table 1 presents the physical properties of the coarse RCAs and NAs used in this study. It is evident from these results that the RCAs had lower densities and significantly higher water absorption compared to those of the NAs. This can be explained by the porous nature of the RACs due to the higher amount of attached mortar on the aggregate (Behera et al., 2014; Rahal, 2007). It can also be seen from Table 1 that the water absorption of the finer RCA was

lower than that of the larger RCA. This can be explained by the lower amount of attached mortar that was present in the finer RCAs. The particle size distributions (PSDs) of the RCAs and NAs that were obtained by sieving tests are illustrated in Fig. 2.

Workability of fresh concrete

The workability of each concrete batch was obtained through slump tests performed in accordance with ASTM standard C143/C143M (ASTM International, 2012). As can been seen from the slump test results given in Table 3, the workability of RACs decreased with an increase in the *RCA%* ratio. A constant compressive strength among the mixes was maintained in each concrete grade through the adjustment of the effective *w/b* ratio with respect to the RCA replacement ratio (*RCA%*) in each concrete mix. Consequently, the effective *w/b* ratio was lower for both NSC and HSC mixes with a higher *RCA%*, which in turn resulted in lower slumps of these mixes. In addition, for a given RCA replacement ratio, NC series RAC exhibited higher workability compared to that of the companion NF series RAC. This is mainly due to the increased surface area of the finer coarse aggregates, which resulted in an increased water demand to coat the aggregate surface during the mix preparation. It can be seen from Table 3 that the slumps of the RAC mixes prepared using TSMA were higher than those of the RACs mixed by NMA. This finding can be explained by the fact that TSMA can reduce the water absorption of RCAs by filling the cracks and pores on the aggregate surface (Tam and Tam, 2007), which leaves more free water to interact with the binder.

Density of hardened concrete

The densities of the hardened concrete, established in a saturated dry condition at the concrete age of 28 days as per ASTM C642-13 (ASTM International, 2013), are reported in

Table 3. The results given in Table 3 indicate that using a higher *RCA%* in the concrete mix resulted in a lower hardened density of the RAC. This observation can be explained by the facts that the air content of RAC is higher than that of NAC due to the higher porosity of RCAs and the bulk density of the coarse RCAs is lower than that of the coarse NA (Katz, 2003; Rao et al., 2007; Topcu and Guencan, 1995). Furthermore, it is observed that the hardened densities of the NF series RACs were lower than those of the companion NC series RACs. This is attributable to the fact that the bulk density of the finer coarse aggregates was lower than that of the larger coarse aggregates used in this study, as shown in Table 1. The results given in Table 3 also indicate that the RACs prepared using TSMA had higher hardened densities than those of the companion RACs prepared using NMA. This observation can be attributed to the reduction in the porosity of RCAs through filling of their pores and cracks by the cement paste during the two stage mixing (TSM) process.

Mechanical properties of hardened concrete

Compressive strength

The compressive strengths (f'_c) of the concrete of the present study were obtained through axial compression tests that were performed in accordance with ASTM standard C39/C39M-05 (ASTM International., 2005). The loading was applied at a rate of 0.3 MPa per second, as per the ASTM standard. Table 4 presents the compressive strength (f'_c) of each concrete mix, where the results were averaged from compression tests on three 100 x 200 mm cylinders. As can be seen from test results given in Table 4, a comparable compressive strength (f'_c) was achieved for each concrete grade (i.e. 40 MPa for NSC and 80 MPa for HSC, respectively) at the concrete age of 28 days. It can also be seen in the same table that the compressive strength (f'_c) of mixes prepared by NMA was slightly lower than that of the companion mixes manufactured using TSMA. This can be attributed to the enhancement in the aggregate to

mortar bond by TSMA (Tam et al., 2007; Thomas et al., 2013). It has been established in previous studies that, for a given effective *w/b* ratio, the compressive strength of RAC decreases with an increase in the RCA replacement ratio (Belén et al., 2011; Choi and Yun, 2012; Ulloa et al., 2013; Wang et al., 2011). In addition, it has been shown that, for normal-strength concrete, a decrease in maximum aggregate size (Φ) results in a lower concrete compressive strength (Alexander and Mindess, 2010; Meddah et al., 2010; Solyman 2005). Therefore, in the present study, the *w/b* ratios of the concrete mixes were progressively reduced with an increase in *RCA%* and decrease in Φ of the mix. This can be seen in Table 3. Through the approach summarized in this section, a nearly identical 28-day compressive strength (f'_c) was achieved for companion for NSC (i.e. f'_c = 40 MPa) and HSC (i.e. f'_c = 80 MPa) mixes with different *RCA%* and Φ.

Modulus of elasticity

The modulus of elasticity (E_c) of the concrete was established through the compression tests performed in accordance with the ASTM standard C469/C469M-14 (ASTM International, 2014). The loading was applied at a rate of 275 kPa per second, in accordance with the ASTM standard. The results of these tests are given in Table 4. It is evident from these results that, at a same compressive strength, RACs with a lower *RCA%* exhibited a higher modulus of elasticity than the companion RACs with a higher *RCA%*. This observation is in agreement with those reported previously (Butler et al., 2013; Etxeberria et al., 2007). It is well understood that the modulus of elasticity has a strong correlation with the compressive strength of the concrete, as well as the volumetric proportion and quality of aggregates used in the concrete mix (Li et al., 1999; Yang, 1998; Zhou et al., 1995). Therefore, the reduction in the elasticity modulus of concretes of the same compressive strength with an increase in *RAC%* can be explained by the inferior mechanical properties of the RCAs compared to those

of the NAs. As can be seen in Table 4, the drop in the E_c value with an increase in *RCA%* was more significant in HSCs than that in NSCs. This phenomenon can be explained by the decreased compatibility between the mortar and coarse aggregate due to the increased difference in their strengths. In addition, comparisons of elastic moduli of NF and NC series mixes given in Table 4 indicate that an increase in the nominal particle size of coarse aggregates led to an increase in E_c. It was reported in previous studies that the E_c decreases with an increase in the volume fraction of the interfacial transition zone (ITZ) (Li et al., 1999; Simeonov and Ahmad, 1995; Vilardell et al., 1998). The decreased particle size (Φ) of coarse aggregate leads to an increase in the overall surface area of the aggregates, resulting in an increased volume fraction of ITZ, which explains the reduction in E_c with a decrease in Φ. The results in Table 4 also show that the modulus of elasticity (E_c) of the RACs manufactured using TSMA was slightly higher than that of the RACs manufactured using NMA, which is attributable to the fact that TSMA improves the aggregate-mortar bond of RACs (Tam et al., 2005; Tam et al., 2007).

Flexural and splitting tensile strength

The flexural strength (f'_r) of each concrete series was obtained through three-point bending tests performed in accordance with the ASTM standard C293/C293M-10 (ASTM, International 2010). The loading applied at a rate that increased the maximum stress recorded on the tension surface between 0.9 and 1.2 MPa per minute, in accordance with the ASTM standard. Three 100 mm × 100 mm × 500 mm beams were tested for each mix at the concrete age of 28 days. The splitting tensile strength (f'_{st}) of each concrete series was determined through the tests performed as per ASTM standard C496/C496M-04 (ASTM International, 2004). The loading was applied at a constant rate within the range of 0.7 to 1.4 MPa per minute as suggested by the ASTM standard. Three 150 mm × 300 mm cylinders

were tested for each mix at the concrete age of 28 days. It is evident from the comparisons shown in Figs. 3 and 4 that the flexural (f'_r) and the splitting tensile strengths (f'_{st}) of both NSC and HSC mixes decreased with an increase *RCA%*. This finding can be attributed to the decrease in the strength of the aggregate-mortar ITZs with an increase in the amount of RCA in the concrete, resulting in a lower mechanical strength under flexure and indirect tension (Akçaoğlu et al., 2002; Lee and Choi, 2013; Sidorova et al., 2014). Furthermore, as is evident from Figs. 3 and 4, the NSC mixes with smaller coarse aggregates exhibited a slightly higher flexural (f'_r) and splitting tensile strengths (f'_{st}) compared to that of their companion mixes with larger coarse aggregates. This observation can be explained by the fact that the increased aggregate size results in an increase in the roughness of aggregate surface, leading to increased stress concentrations and propagations of cracks within the ITZ, which in turn results in a lower strength of aggregate-mortar ITZs (Akçaoğlu et al., 2002; Elices and Rocco, 2008; Van Mier, 1996). It should also be noted that, in the present study the RACs manufactured with larger coarse aggregates had a lower mortar strength caused by their higher effective *w/b* ratios, which in turn contributed to their lower flexural and splitting tensile strengths. Moreover, as explained previously, with the enhancement of the bond strength between aggregates and mortar, flexural (f'_r) and splitting tensile strengths (f'_{st}) of the RACs prepared by TSMA were slightly higher than those of the RACs mixed using NMA.

Durability-related properties

Drying shrinkage

The drying shrinkage of the concrete mixes was monitored up to the concrete age of 70 days following the test method given in ASTM C596-07 (ASTM International, 2007). Figures 5 (a) to (c) illustrate the shrinkage during the drying process for concrete mixes of the present study. It is evident from the figure that the RCA replacement ratio (*RCA%*) had a pronounced

influence on the drying shrinkage, with the concretes containing higher amount of RCAs exhibiting a higher shrinkage strain at a given curing age in all mixes. This observation can be attributed to the lower capability of RCA compared to that of NA in restraining deformations in the cement paste due to the higher porosity of the RCA in the concrete (Ajdukiewicz and Kliszczewicz, 2002; Katz, 2003; Tam and Tam, 2007). As shown in Figs. 5 (a) and (b), the drying shrinkage of the RACs manufactured using finer RCAs was lower than that of the companion RACs manufactured using larger RCAs. This can be attributed to the decreased absorption of RCAs with smaller particle size (Φ) as evident from Table 1, due to reduced attached mortar amount. Furthermore, it can be seen from Figs. 5 (b) and (c) that, although HSC mixes had a higher early age shrinkage beyond the concrete age of 21 days, the drying shrinkage of NSC mixes continued at a higher rate compared to those of the companion HSC mixes. By the curing age of 70 days, the NSC mixes had a higher shrinkage than that of the companion HSC mixes. This phenomenon can be explained by the higher rate of chemical reactions experienced by HSCs during the earlier curing ages, resulting in significantly higher endogenous shrinkage of HSCs during this phase (Gilbert, 2001; Kovler and Zhutovsky, 2006; Tazawa, 1999). However, due to the presence of a larger amount of residual water in the structure of NSC after hydration (Gilbert, 2001), NSCs exhibited significantly higher shrinkage than that of the HSCs during the later stages of curing. The results shown in Figs. 5 (a) to (c) also indicate that only marginal differences existed between drying shrinkages of companion mixes prepared using TSMA and NMA

Water absorption

Absorption tests were carried out on all concrete mixes in accordance with ASTM standard C642-13 (ASTM International, 2013). 48 hours after casting in ambient temperature, the hardened concrete specimens were initially dried in the oven at a temperature of 105° C over

24 hours, and then they were subsequently cooled at the ambient temperature to determine their oven-dried masses (M_O). Following this, the specimens were immersed in water for 48 hours to establish their saturated surface-dry masses (M_S). The water absorption (Ai) of the concretes was determined from Eq. (1), as per ASTM C642-13 (ASTM International, 2013), and the calculated values are shown in Fig. 6.

$$A_i = (M_S - M_O)/M_O \times 100 \quad (1)$$

It can be seen from the results given in Fig. 6 that water absorption of NC and HC series mixes increased with an increase in their *RCA%*. On the other hand, as illustrated in Fig. 6, there was no clear influence of *RCA%* on water absorption of NF series mixes. As discussed previously, the RCAs had significantly higher water absorption than those of the NAs. This in turn resulted in the increased water absorption of concretes that contained higher amounts of RCAs. The differences between the observations from NC and NF series of mixes can be explained by the differences in water absorption of the larger and smaller RCAs used in the present study, as was discussed previously. This is also evident from the comparison of the relative water absorption of the companion NC and NF series specimens, which indicate that water absorption of RACs increased with an increase in the RCA particle size (Φ) used in the concrete mix. This observation is in agreement with those reported in previous studies on RAC (Katz, 2003; Tam and Tam, 2009), and it can be explained by the lower absorption of the finer RCAs compared to that of their larger counterparts, and the better compaction of concretes manufactured with finer coarse aggregates that potentially leads to a reduced volume of pores in concrete. Results shown in Fig. 6 also indicate that the water absorption of the HC series mixes was slightly lower than that of the companion NC series mixes. This is attributable to the denser structure of HSC owing to its lower *w/b* ratio. Finally, the results in Fig. 6 show that the NSC mixes manufactured using TSMA exhibited slightly lower water absorption compared to that of the companion NSC mixes prepared using NMA. On the other

hand, as can be seen from Fig. 6, no influence of the mixing method was evident on the water absorption of the HSC mixes.

CONCLUSIONS

This paper has reported the results of an experimental study on the mechanical and durability-related properties of concretes prepared with coarse RCAs of different sizes and contents. These results indicate that RACs exhibit close but slightly lower mechanical and durability-related properties compared to those of the companion NACs of the same compressive strength. These properties are satisfactory to allow the use of RAC as a feasible alternative to conventional concrete in structural applications, thereby enabling the significant environmental and economic benefits that result from the replacement of NACs with RACs materialize. It has been shown that through a proper adjustment of the effective *w/b* ratio with respect to the RCA replacement ratio and particle size of coarse aggregate, it is possible to achieve an equal compressive strength in concretes manufactured with different RCA grades and contents. The results of such concretes of a similar compressive strength show that an increase in the RCA replacement ratio results in a decrease in the elastic modulus and flexural and splitting tensile strengths of the concrete, whereas an increase in the coarse aggregate size results in an increase in the elastic modulus but a decrease in the flexural and splitting tensile strengths. It is also found that an increase in the RCA replacement ratio and coarse aggregate particle size results in an increase in the drying shrinkage and water absorption of concrete. Finally, the results indicate that in the preparation of RAC the use of TSMA leads to some improvements in mechanical and, to a lesser extent, durability properties of the concrete compared to those attained by companion mixes prepared using NMA.

REFERENCES

Abd Elhakam, A., Mohamed, A. E., Awad, E., 2012. Influence of self-healing, mixing method and adding silica fume on mechanical properties of recycled aggregates concrete. *Constr. Build. Mater. 35*, 421-427.

Ajdukiewicz, A., Kliszczewicz, A., 2002. Influence of recycled aggregates on mechanical properties of HS/HPC. *Cem. Concr. Comp. 24*(2), 269-279.

Ajdukiewicz, A. B., Kliszczewicz, A. T., 2007. Comparative tests of beams and columns made of recycled aggregate concrete and natural aggregate concrete. *J. Adv. Concr. Technol. 5*(2), 259-273.

Akçaoğlu, T., Tokyay, M., Çelik, T., 2002. Effect of coarse aggregate size on interfacial cracking under uniaxial compression. *Mater. Lett. 57*(4), 828-833.

Alexander, M., Mindess, S., 2010. *Aggregates in Concrete*. CRC Press, New York, U.S.A.

AS 3600-2009., 2009. Australian Standard for Concrete Structures. S. A, North Sydney.

ASTM International., 2004. Standard Test Method for Splitting Tensile Strength of Cylindrical Concrete Specimens, C496/C496M-04, West Conshohocken, PA.

ASTM International., 2005. Standard Test Method for Compressive Strength of Cylindrical Concrete Specimens, C39/C39M-05, West Conshohocken, PA**.**

ASTM International., 2007. Standard Test Method for Drying Shrinkage of Mortar Containing Hydraulic Cement, C596-07, West Conshohocken, PA.

ASTM International., 2010. Standard Test Method for Flexural Strength of Concrete (Using Simple Beam With Center-Point Loading), C293 / C293M -10, West Conshohocken, PA.

ASTM International., 2012. Standard Test Method for Slump of Hydraulic-Cement Concrete, C143/C143M-12, West Conshohocken.

ASTM International., 2013. Standard Test Method for Density, Absorption, and Voids in Hardened Concrete, C642-13, West Conshohocken, PA.

ASTM International., 2014. Standard Test Method for Static Modulus of Elasticity and Poisson's Ratio of Concrete in Compression, C469 / C469M - 14, West Conshohocken, PA

Bairagi, N. K., Vidyadhara, H. S., Ravande, K., 1990. Mix design procedure for recycled aggregate concrete. *Constr. Build. Mater. 4*(4), 188-193.

Barbudo, A., de Brito, J., Evangelista, L., Bravo, M., Agrela, F., 2013. Influence of water-reducing admixtures on the mechanical performance of recycled concrete. *J. Clean. Prod. 59*, 93-98.

Behera, M., Bhattacharyya, S. K., Minocha, A. K., Deoliya, R., Maiti, S., 2014. Recycled aggregate from C&D waste & its use in concrete–A breakthrough towards sustainability in construction sector: A review. *Constr. Build. Mater. 68*, 501-516.

Belén, G. F., Fernando, M. A., Diego, C. L., Sindy, S. P., 2011. Stress–strain relationship in axial compression for concrete using recycled saturated coarse aggregate. *Constr. Build. Mater. 25*(5), 2335-2342.

Beltrán, M. G., Barbudo, A., Agrela, F., Galvín, A. P., Jiménez, J. R., 2014. Effect of cement addition on the properties of recycled concretes to reach control concretes strengths. *J. Clean. Prod. 79*, 124-133.

Beshr, H., Almusallam, A. A., Maslehuddin, M., 2003. Effect of coarse aggregate quality on the mechanical properties of high strength concrete. *Constr. Build. Mater. 17*(2), 97-103.

Butler, L., West, J. S., Tighe, S. L., 2013. Effect of recycled concrete coarse aggregate from multiple sources on the hardened properties of concrete with equivalent compressive strength. *Constr. Build. Mater. 47*, 1292-1301.

Çakır, Ö., 2014. Experimental analysis of properties of recycled coarse aggregate (RCA) concrete with mineral additives. *Constr. Build. Mater. 68*, 17-25.

Choi, W. C.,Yun, H. D., 2012. Compressive behavior of reinforced concrete columns with recycled aggregate under uniaxial loading. *Eng. Struct. 41*, 285-293

Dilbas, H., Şimşek, M., Çakır, Ö., 2014. An investigation on mechanical and physical properties of recycled aggregate concrete (RAC) with and without silica fume. *Constr. Build. Mater. 61*, 50-59.

Elices, M., Rocco, C. G., 2008. Effect of aggregate size on the fracture and mechanical properties of a simple concrete. *Eng. Fract. Mech.75*(13), 3839-3851.

Etxeberria, M., Vázquez, E., Marí, A., Barra, M., 2007. Influence of amount of recycled coarse aggregates and production process on properties of recycled aggregate concrete. *Cem. Concr. Res. 37*(5), 735-742.

Gilbert, R. I., 2001. Shrinkage, cracking and deflection-the serviceability of concrete structures. *Electr. J Struct. Eng.1*(1), 2-14.

Katz, A., 2003. Properties of concrete made with recycled aggregate from partially hydrated old concrete. *Cem. Concr. Res. 33*(5), 703-711.

Kheder, G. F., Al-Windawi, S. A., 2005. Variation in mechanical properties of natural and recycled aggregate concrete as related to the strength of their binding mortar. *Mater. Struct. 38*(7), 701-709.

Kou, S. C., Poon, C. S., Chan, D., 2007. Influence of fly ash as cement replacement on the properties of recycled aggregate concrete. *J. Matr. Civ. Eng. 19*(9), 709-717.

Kou, S. C., Poon, C. S., Chan, D., 2008. Influence of fly ash as a cement addition on the hardened properties of recycled aggregate concrete. *Mater. Struct. 41*(7), 1191-1201.

Kou, S. C., Poon, C. S., 2009. Properties of self-compacting concrete prepared with coarse and fine recycled concrete aggregates. *Cem. Concr. Comp. 31*(9), 622-627.

Kovler, K., Zhutovsky, S., 2006. Overview and future trends of shrinkage research. *Mater. Struct. 39*(9), 827-847.

Kwan, W. H., Ramli, M., Kam, K. J., Sulieman, M. Z., 2012. Influence of the amount of recycled coarse aggregate in concrete design and durability properties. *Constr. Build. Mater. 26*(1), 565-573.

Lee, G. C., Choi, H. B., 2013. Study on interfacial transition zone properties of recycled aggregate by micro-hardness test. *Constr. Build. Mater. 40*, 455-460.

Li, G., Zhao, Y., Pang, S. S., Li, Y., 1999. Effective Young's modulus estimation of concrete. *Cem. Concr. Res. 29*(9), 1455-1462.

Limbachiya, M. C., Leelawat, T., Dhir, R. K., 2000. Use of recycled concrete aggregate in high-strength concrete. *Mater. Struct. 33*(9), 574-580.

Limbachiya, M., Meddah, M. S., Ouchagour, Y., 2012a. Use of recycled concrete aggregate in fly-ash concrete. *Constr. Build. Mater. 27*(1), 439-449.

Limbachiya, M., Meddah, M. S., Ouchagour, Y., 2012b. Performance of Portland/silica fume cement concrete produced with recycled concrete aggregate. *ACI. Mater. J.* 109 (1), 91-100.

Marie, I., Quiasrawi, H., 2012. Closed-loop recycling of recycled concrete aggregates. *J. Clean Prod. 37*, 243-248.

Mas, B., Cladera, A., Olmo, T. D., Pitarch, F., 2012. Influence of the amount of mixed recycled aggregates on the properties of concrete for non-structural use. *Constr. Build. Mater. 27*(1), 612-622.

Meddah, M. S., Zitouni, S., Belâabes, S., 2010. Effect of content and particle size distribution of coarse aggregate on the compressive strength of concrete. *Constr. Build. Mater. 24*(4), 505-512.

Medina, C., Zhu, W., Howind, T., de Rojas, M. I. S., Frías, M. 2014. Influence of mixed recycled aggregate on the physical–mechanical properties of recycled concrete. *J. Clean. Prod. 68*, 216-225.

Mefteh, H., Kebaïli, O., Oucief, H., Berredjem, L., Arabi, N., 2013. Influence of moisture conditioning of recycled aggregates on the properties of fresh and hardened concrete. *J. Clean. Prod. 54*, 282-288.

Miled, K., Limam, O., Sab, K., 2012. A probabilistic mechanical model for prediction of aggregates' size distribution effect on concrete compressive strength. *Physica. A. 391*(12), 3366-3378.

Özturan, T., Çeçen, C., 1997. Effect of coarse aggregate type on mechanical properties of concretes with different strengths. *Cem. Concr. Res. 27*(2), 165-170.

Portland Cement Association., and ACI Committee 318., 2009. *ACI 318-11: Building Code Requirements for Structural Concrete and Commentary, PCA notes on ACI 318-11: with design applications*. Farmington Hills, Mich: *ACI Int.*

Radonjanin, V., Malešev, M., Marinković, S., 2010. Recycled concrete as aggregate for structural concrete production. *Sustain. 2*(5), 1204-1225.

Radonjanin, V., Malešev, M., Marinković, S., Al Malty, A. E. S., 2013. Green recycled aggregate concrete. *Constr. Build. Mater. 47*, 1503-1511.

Rahal, K., 2007. Mechanical properties of concrete with recycled coarse aggregate. *Build. Environ. 42*(1), 407-415.

Rao, A., Jha, K. N., Misra, S., 2007. Use of aggregates from recycled construction and demolition waste in concrete. *Resources, Resour. Conserv. Recy. 50*(1), 71-81.

Rao, M. C., Bhattacharyya, S. K., Barai, S. V., 2011. Influence of field recycled coarse aggregate on properties of concrete. *Mater. Struct. 44*(1), 205-220.

Rodrigues, F., Carvalho, M. T., Evangelista, L., de Brito, J., 2013. Physical–chemical and mineralogical characterization of fine aggregates from construction and demolition waste recycling plants. *J. Clean. Prod. 52*, 438-445.

Sheen, Y. N., Wang, H. Y., Juang, Y. P., Le, D. H., 2013. Assessment on the engineering properties of ready-mixed concrete using recycled aggregates. *Constr. Build. Mater. 45*, 298-305.

Sidorova, A., Vazquez-Ramonich, E., Barra-Bizinotto, M., Roa-Rovira, J. J., Jimenez-Pique, E., 2014. Study of the recycled aggregates nature's influence on the aggregate–cement paste interface and ITZ. *Constr. Build. Mater. 68*, 677-684.

Sim, J. I., Yang, K. H., Jeon, J. K., 2013. Influence of aggregate size on the compressive size effect according to different concrete types. *Constr. Build. Mater. 44*, 716-725.

Simeonov, P., Ahmad, S., 1995. Effect of transition zone on the elastic behavior of cement-based composites. *Cem. Concr. Res. 25*(1), 165-176.

Solyman, M., 2005. Classification of recycled sands and their applications as fine aggregates for concrete and bituminous mixtures. *Doktor-Ingenieurs Dissertation, Fachbereich Bauingenieurwesen der Universität Kassel,* Kassel, Germany.

Sonawane, M. T. R., Pimplikar, S. S., 2013. Use of Recycled Aggregate in Concrete. *Int. J. Eng. Res. Technol. 2*, 1-9.

Structural use of concrete., 1997. Part 1: Code of practice for design and construction; Part 2: Code of practice for special circumstances, British Standard Institution, London.

Tabsh, S. W., Abdelfatah, A. S., 2009. Influence of recycled concrete aggregates on strength properties of concrete. *Constr. Build. Mater. 23*(2), 1163-1167.

Tam, V. W., Gao, X. F., and Tam, C. M., 2005. Microstructural analysis of recycled aggregate concrete produced from two-stage mixing approach. *Cem. Concr. Res. 35*(6), 1195-1203.

Tam, V. W., Tam, C. M., 2007. Assessment of durability of recycled aggregate concrete produced by two-stage mixing approach. *J.Mater. Sci. 42*(10), 3592-3602.

Tam, V. W., Tam, C. M., 2009. Parameters for assessing recycled aggregate and their correlation. *Waste Manag. Res. 27*(1), 52-58.

Tam, V. W., Tam, C. M., Wang, Y., 2007. Optimization on proportion for recycled aggregate in concrete using two-stage mixing approach. *Constr. Build. Mater. 21*(10), 1928-1939.

Tazawa, E. I. (Ed.)., 1999. *Autogenous Shrinkage of Concrete*. CRC Press, New York, U.S.A.

Thomas, C., Setién, J., Polanco, J. A., Alaejos, P., de Juan, M. S., 2013. Durability of recycled aggregate concrete. *Constr. Build. Mater. 40*, 1054-1065.

Topcu, I. B., 1997. Physical and mechanical properties of concretes produced with waste concrete. *Cem. Concr. Res. 27*(12), 1817-1823.

Topcu, I. B., Guencan, N. F., 1995. Using waste concrete as aggregate. *Cem. Concr. Res. 25*(7), 1385-1390.

Torgal, F. P., Jalali, S., 2011. Construction and Demolition (C&D) Wastes. In *Eco-efficient Construction and Building Materials.*(pp. 51-73). Springer London.

Tošić, N., Marinković, S., Dašić, T., Stanić, M., 2015. Multicriteria optimization of natural and recycled aggregate concrete for structural use. *J. Clean. Prod. 87*, 766-776.

Tumidajski, P. J., Gong, B., 2006. Effect of coarse aggregate size on strength and workability of concrete. *Canadian J. Civ. Eng*. *33*(2), 206-213.

Ulloa, V. A., García-Taengua, E., Pelufo, M. J., Domingo, A., Serna, P., 2013. New views on effect of recycled aggregates on concrete compressive strength. *ACI Mater. J. 110*(6).

Van Mier, J. G., 1996. *Fracture Processes of Concrete* (Vol. 12). CRC press, New York, U.S.A.

Vilardell, J., Aguado, A., Agullo, L., Gettu, R., 1998. Estimation of the modulus of elasticity for dam concrete. *Cem. Concr. Res. 28*(1), 93-101.

Wang, Z., Wang, L., Cui, Z., Zhou, M., 2011. Effect of recycled coarse aggregate on concrete compressive strength. *Transactions of Tianjin University*, *17*, 229-234.

Yang, C. C., 1998. Effect of the transition zone on the elastic moduli of mortar. *Cem. Concr. Res. 28*(5), 727-736.

Yang, K. H., Chung, H. S., Ashour, A. F., 2008. Influence of type and replacement level of recycled aggregates on concrete properties. *ACI Mater. J. 105*(3).

Zain, M. F. M., Mahmud, H. B., Ilham, A., Faizal, M., 2002. Prediction of splitting tensile strength of high-performance concrete. *Cem. Concr. Res.32*(8), 1251-1258.

Zhou, F. P., Balendran, R. V., Jeary, A. P., 1998. Size effect on flexural, splitting tensile, and torsional strengths of high-strength concrete. *Cem. Concr. Res. 28*(12), 1725-1736.

Zhou, F. P., Lydon, F. D., Barr, B. I. G., 1995. Effect of coarse aggregate on elastic modulus and compressive strength of high performance concrete. *Cem. Concr. Res. 25*(1), 177-186.

LIST OF TABLE CAPTIONS

Table 1. Properties of coarse and fine aggregates

Aggregate type	Nominal maximum particle size (mm)	Oven-dried bulk density (kg/dm^3)	Relative density (kg/dm^3)	Apparent density (kg/dm^3)	Water absorption (%)	Fineness modulus
Larger NA	12	1.54	2.71	2.86	2.01	5.16
Larger RCA	12	1.18	2.22	2.56	6.12	5.08
Finer NA	7.0	1.46	2.57	2.68	1.96	3.76
Finer RCA	7.0	1.14	2.15	2.45	4.08	3.48
Natural sand	0.40	1.52	2.62	-	0.820	-

Table 2. Chemical composition and physical properties of cementitious materials

Item	Cementitious materials (%)	
	Ordinary Portland cement	Silica fume
SiO_2	21.4	92.5
$ZrO_2 + HfO_2$	-	5.50
Al_2O_3	5.55	0.35
Fe_2O_3	3.46	0.40
P_2O_5	-	0.30
CaO	64.0	0.03
MgO	1.86	-
SO_3	1.42	0.90
K_2O	0.54	0.02
Na_2O	0.26	0.02
	Compounds	
C_3S	51.0	-
C_2S	23.1	-
C_3A	8.85	-
C_4AF	10.5	-
	Fineness	
Surface area (m^2/kg)	330	18,000

Table 3. Mix proportions of concrete

	Normal-Strength Concrete									High-Strength Concrete				
	NC-0-T	NC-25-T	NC-50-T	NC-100-T	NC-100-N	NF-0-T	NF-50-T	NF-100-T	NF-100-N	HC-0-T	HC-25-T	HC-50-T	HC-100-T	HC-100-N
RCA Replaced NA ratio	0%	25%	50%	100%	100%	0%	50%	100%	100%	0%	25%	50%	100%	100%
Cement (kg/m^3)	380	380	380	380	380	380	380	380	380	506	506	506	506	506
Silica Fume (kg/m^3)	0	0	0	0	0	0	0	0	0	44	44	44	44	44
Sand (kg/m^3)	710	710	710	710	710	710	710	710	710	710	710	710	710	710
Natural Aggregate (kg/m^3)	1065	799	533	0	0	1012	506	0	0	1065	799	533	0	0
Recycled Aggregate (kg/m^3)	0	204	408	816	816	0	394	787	787	0	204	408	816	816
Water- Effective (kg/m^3)	209	201	194	179	179	201	186	171	171	167	159	152	137	137
Water- Total (kg/m^3)	237	236	236	235	235	227	218	209	209	195	194	193	193	193
Superplasticizer (kg/m^3)	0	0	0	0	0	0	0	0	0	7	7	7	10	10
Effective *w/b* ratio*	0.55	0.53	0.51	0.47	0.47	0.53	0.49	0.45	0.45	0.31	0.30	0.29	0.26	0.26
Total *w/b* ratio*	0.62	0.62	0.62	0.62	0.62	0.60	0.57	0.55	0.55	0.36	0.36	0.36	0.36	0.36
Slump (mm)	220	180	125	115	105	235	155	125	110	180	170	130	100	85
Hardened density(kg/m^3)	2347	2289	2236	2199	2138	2287	2174	2147	2115	2518	2486	2425	2403	2378

* Including the water coming from the superplasticizer (i.e. 70% water by weight)

Table 4. Results of axial compression tests

Concrete series	f'_c (7-day) (MPa)	f'_c (28-day) (MPa)	E_c (28-day) (GPa)
N-C-0-T	29.4	40.9	29.3
N-C-25-T	29.9	41.0	29.0
N-C-50-T	29.0	40.5	28.2
N-C-100-T	29.3	40.3	27.2
N-C-100-N	26.7	38.0	26.7
N-F-0-T	28.8	40.1	28.1
N-F-50-T	29.8	41.2	27.9
N-F-100-T	30.2	40.8	25.7
N-F-100-N	28.3	39.2	25.1
H-C-0-T	69.0	82.6	36.5
H-C-25-T	68.6	83.5	34.8
H-C-50-T	68.7	84.1	32.7
H-C-100-T	67.9	82.4	31.3
H-C-100-N	68.5	79.3	30.8

LIST OF FIGURES

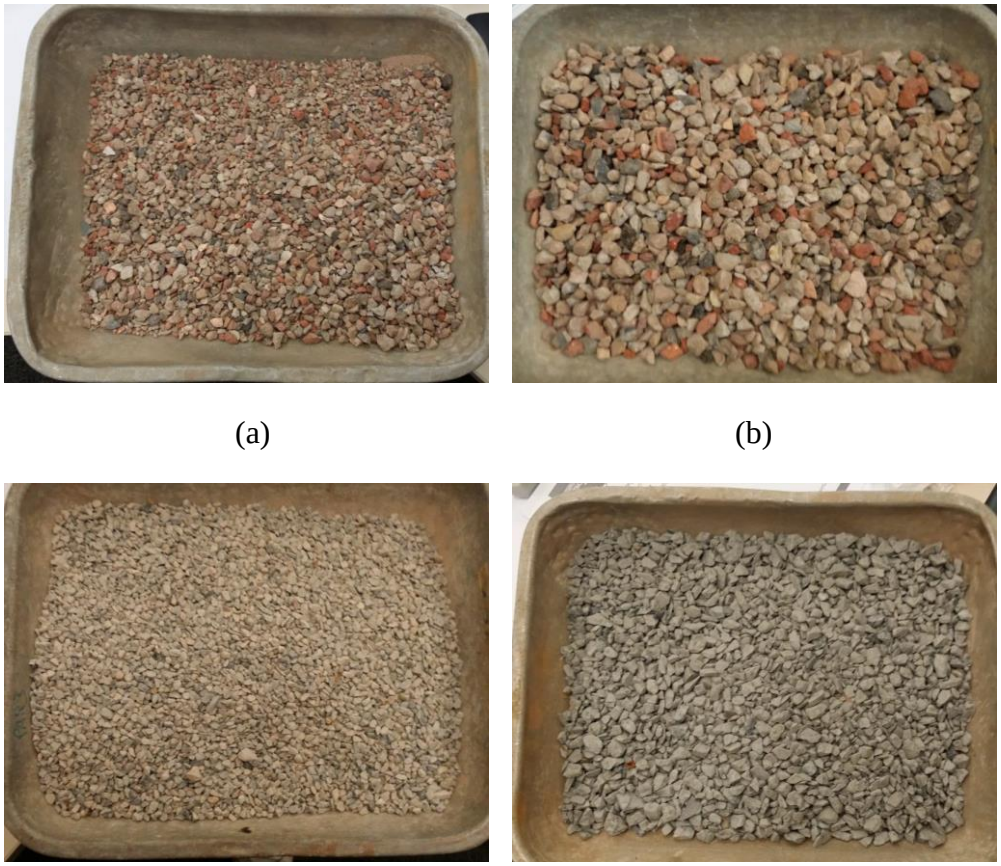

(a) (b)

(c) (d)

Figure 1. Coarse aggregates: a) finer coarse RCA (7-mm maximum size (Φ)); b) larger coarse RCA (12-mm maximum size (Φ)); c) finer coarse NA (7-mm maximum size (Φ)); d) larger coarse NA (12-mm maximum size (Φ))

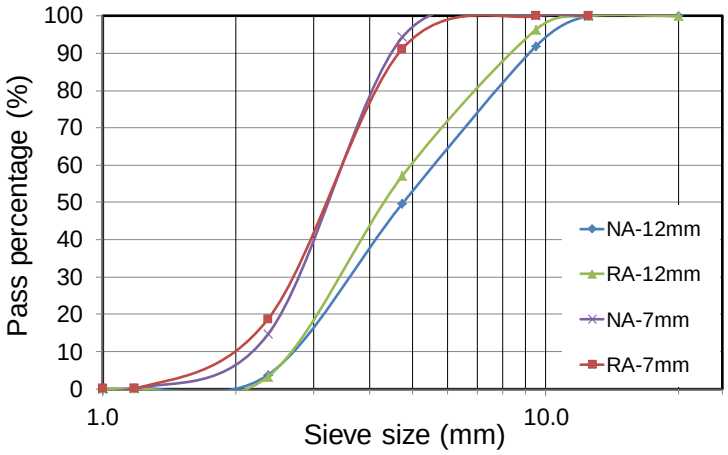

Figure 2. Sieving test results of coarse aggregates: Particle Size Distribution (PSD)

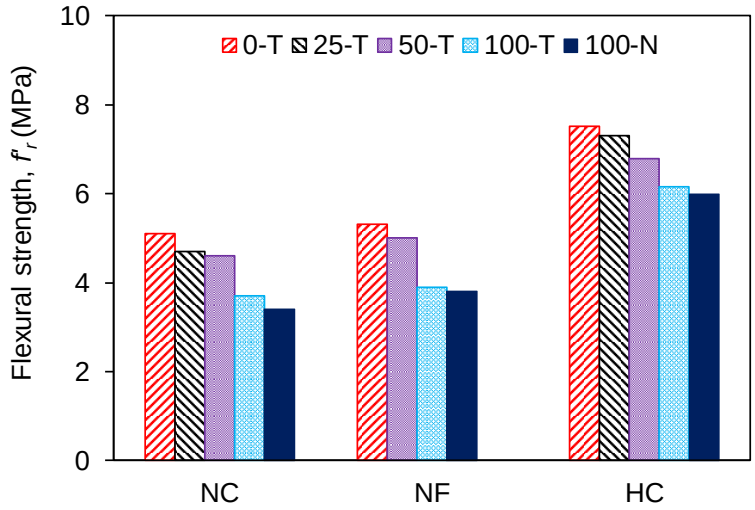

Figure 3. Flexural strength of concrete at 28 days

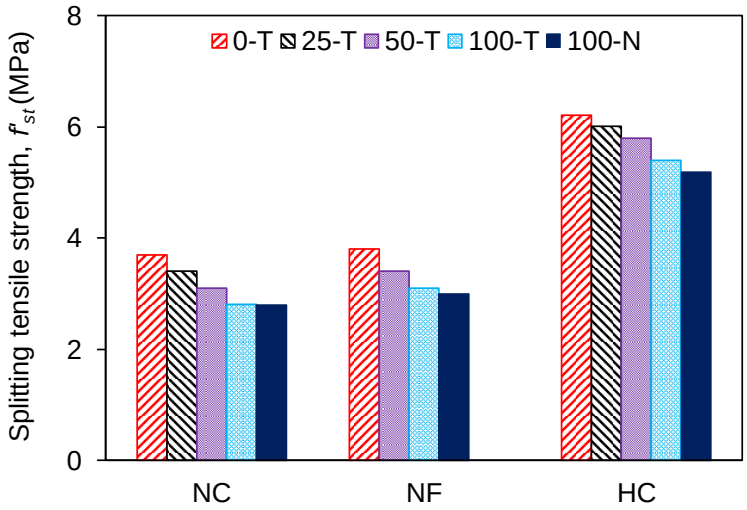

Figure 4. Splitting tensile strength of concrete at 28 days

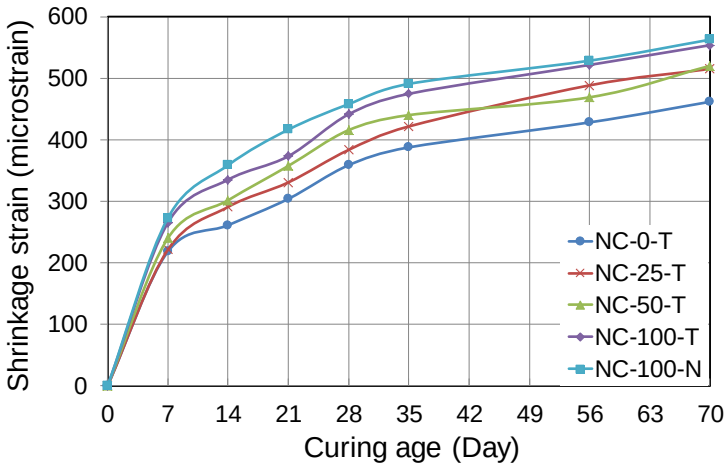

(a)

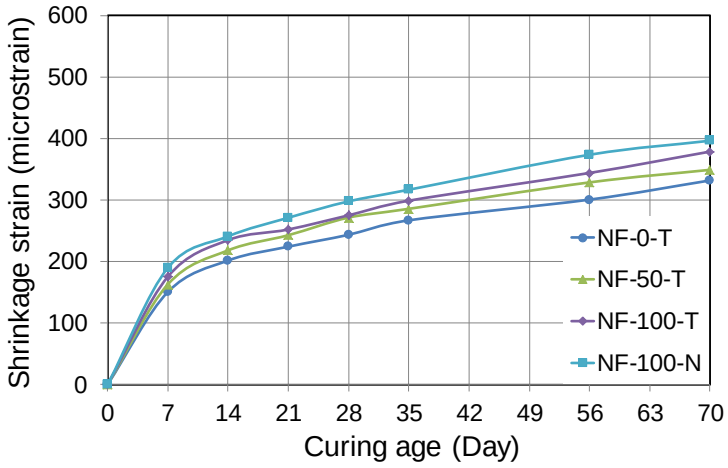

(b)

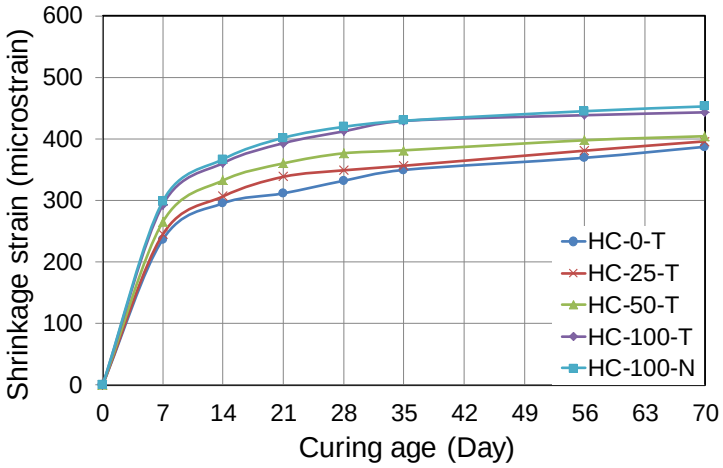

(c)

Figure 5. Shrinkage of concrete: a) NC series; b) NF series; c) HC series

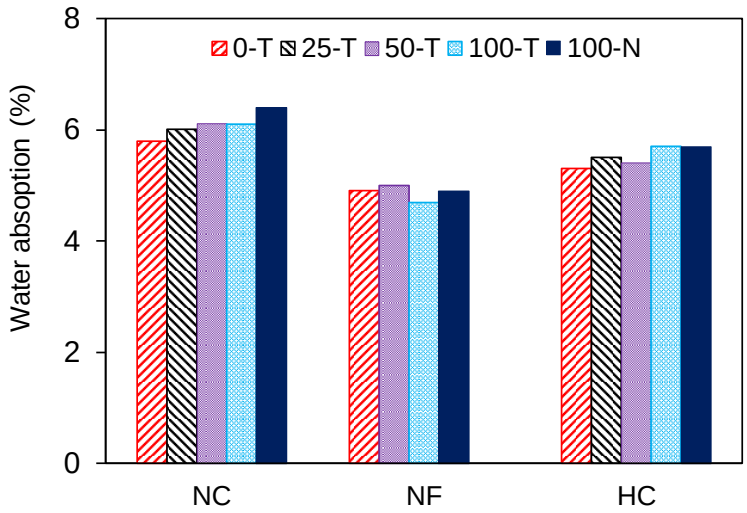

Figure 6. Water absorption of hardened concrete at 28 days

JOURNAL ARTICLE 4

THIS PAGE HAS BEEN LEFT INTENTIONALLY BLANK

Statement of Authorship

Title of Paper	Behavior of Recycled Aggregate Concrete-filled Basalt and Carbon FRP Tubes
Publication Status	☐ Published ☐ Accepted for Publication ☑ Submitted for Publication ☐ Publication Style
Publication Details	Submitted to Construction and Building Materials, year 2015

Author Contributions

Name of Principal Author (Candidate)	Tianyu Xie		
Contribution to the Paper	Supervision of experimental tests, analysis of test results, and preparation of manuscript		
Signature		Date	2/9/2015

Name of Co-Author	Dr Togay Ozbakkaloglu		
Contribution to the Paper	Design of experimental tests, supervision of experimental tests, and review of manuscript		
Signature		Date	2/9/2015

Behavior of Recycled Aggregate Concrete-filled Basalt and Carbon FRP Tubes

Tianyu Xie[1] and Togay Ozbakkaloglu[2]

ABSTRACT

Confinement of recycled aggregate concrete (RAC) with fiber-reinforced polymer (FRP) has shown its great potential as a high-performance structural element that also contributes to the reduction in environmental impact of natural resource depletion. This paper presents the results of an experimental study on the axial compressive behavior of concrete-filled FRP tubes (CFFTs), prepared using different amounts of recycled concrete aggregate (RCA). A total of 36 CFFTs were tested under axial compression. The effects of the RCA replacement ratio, specimen cross-sectional shape, FRP type, and concrete strength were studied. The results indicate that the axial stress-strain behavior of CFFTs is influenced by the amount of RCA, with particularly significant influences noted on the ultimate axial strain and FRP hoop rupture strains. It was observed that, at the same in-place concrete strength, FRP-confined concrete with a higher RCA content exhibited a lower compressive strength and a higher ultimate axial strain under axial compression. It was also found that the increased RCA content leads to a decrease in hoop rupture strain of CFFTs. CFFTs manufactured with CFRP tubes (instead of BFRP tubes) and CFFTs with circular cross-sections (instead of square cross-sections) exhibit a higher compressive strength and a lower ultimate axial strain. The influences of specimen cross-sectional shape and FRP type on axial compressive behavior of CFFTs were seen to vary with the RCA content.

Keywords: Recycled concrete aggregate (RCA); Recycled aggregate concrete (RAC); Fiber-reinforced polymer (FRP); Confinement; Compressive strength; Stress-strain relationship.

[1] MPhil Candidate, School of Civil, Environmental and Mining Engineering, University of Adelaide, Australia.

[2] (Corresponding author) Senior Lecturer, School of Civil, Environmental and Mining Engineering, University of Adelaide, Australia. Tel : +618 8313 6477; Fax : +618 8313 4359; Email: togay.ozbakkaloglu@adelaide.edu.au

1. INTRODUCTION

In recent years, the increased rate of urbanization has led to the generation and release of large amounts of construction and demolition (C&D) wastes. From the viewpoint of environmental preservation and effective utilization of resources, it is beneficial and necessary to reuse the C&D wastes. Recycled concrete aggregate (RCA), which is obtained by crushing old concrete elements from construction and demolition (C&D) waste, has been considered as an alternative aggregate material for use in structural concrete, with the aim of achieving resource sustainability in the construction industry. Recycled aggregate concrete (RAC) is an environment-friendly concrete in which a part or all of the natural aggregate (NA) is replaced by RCA. A significant volume of studies have been reported to date on the behavior of RACs in literature. These studies have shown that RAC has great potential to be a feasible alternative to natural aggregate concrete (NAC) in the construction industry. However, when compared with companion NACs, RACs manufactured with full replacement of NAs by RACs exhibit around 20 to 30% lower compressive strengths [1-5], 30 to 50% lower elastic moduli [6-9], and up to 270% higher drying shrinkages [3,10]. Due to these shortcomings, currently RACs are mostly used as non-structural concretes, which greatly limits their use in infrastructure applications.

It is well established that external confinement of concrete with FRP tube results in a significant improvement in the compressive behavior of concrete. Over the past few decades, a great number of studies have been conducted to investigate the application of FRP confinement techniques in strengthening existing columns [11-17], and in the construction of new composite columns [18-22], as revealed by recent review studies [23-26]. However, a careful review of existing literature on confined RACs shows that only limited research attention has focused on the investigation of FRP-confined RACs, with four studies to date

reporting on their behavior [27-30]). Xiao et al. [27] and Xiao et al. [28] reported on the behavior of 25 concentrically or eccentrically loaded RAC specimens confined by glass FRP (GFRP), which had in-place concrete strengths up to 42.7 MPa and a fiber orientation of 30 degrees measured from lateral axis. Zhao et al. [29] tested 18 RAC specimens confined by GFRP sheets, with an approximately 45 MPa in-place concrete strength. Islam et al. [30] investigated the axial-compressive behavior of 10 square RAC specimens confined by carbon FRP (CFRP) or GFRP sheets, with the maximum unconfined concrete strength of 40.8 MPa. A review of existing studies on FRP-confined RACs revealed that no study has reported to date on the behavior of basalt FRP (BFRP)-confined RACs, and no information is currently available on the effect of cross section shape on axial compressive behavior of FRP-confined RACs. In addition, as reported in previous studies [31-33], the popularity of high-strength concrete (HSC) in the construction industry has been undergoing steady growth due to the superior performance and economy offered by the material over normal-strength concrete (NSC). However, no study has been reported to date on the behavior of high-strength RAC (HSRAC)-filled FRP tubes (HSRACFFTs).

This paper presents an experimental study that aimed to address the aforementioned research gaps through examination of influences of key parameters on axial compressive behavior of CFFTs manufactured with CFRP or BFRP tubes. This is the first study to report on the axial compressive behavior of CFFTs manufactured using HSRACs, and also the first study to investigate the behavior of BFRP-confined RACs. The paper initially provides a summary of the experimental program, including material properties, specimen properties, and testing procedures. Following this, results of the experimental program are presented. Finally, a detailed discussion of the results of the experimental study is provided, where the influences

of RCA replacement ratio, specimen cross-sectional shape, FRP type, and concrete strength are presented, along with other key experimental observations.

2. TEST PROGRAM

2.1 Test specimens

A total of 36 circular CFFTs, including nine circular and nine square normal-strength CFFTs (NSCFFTs) and 18 high strength-CFFTs (HSCFFTs) were manufactured and tested under axial compression. The details of these specimens are given in Table 6. The circular specimens were 152.5 mm in diameter measured at the concrete core, and 305 mm in height. The square specimens consistently had a side length of 152.5 mm measured at the concrete core, and a corner radius of 30 mm. The test parameters included: RCA replacement ratio (i.e. 0%, 50% or 100%), type of FRP (i.e. BFRP or carbon FRP (CFRP)), cross-sectional shape of testing specimen (i.e. square or circular) and concrete strength (i.e. NSC or HSC). All of the confined specimens were manufactured as CFFTs, with the FRP tubes manufactured using a manual wet lay-up procedure with unidirectional carbon or basalt fiber sheets.

2.2 Materials

2.2.1 Aggregates

The RCAs used in the present study were supplied by Adelaide Recycled Resource (ARR) in South Australia, which were produced by initially removing impurities from C&D wastes and subsequently crushing the demolition concrete using a jaw crusher. Figure 2 illustrates the RCA used in this study. These RCAs were added at different RCA volume replacement ratios (*RCA%*) of 0, 50, and 100 to represent NAC and concrete containing moderate and high amounts of RCAs. The physical properties of both grades of RCAs are given in Table 1. All coarse RCAs were initially washed to remove impurities, and then pre-oven dried for 24

hours at 105˚C and subsequently cooled at ambient temperature for more than three hours before mixing of the concrete.

The coarse NAs of the present study were crushed bluestone gravel sourced from McLaren Vale Quarry (Fleurieu Peninsula). To maintain consistency in the coarse aggregate size of RAC and conventional concrete mixes, the NAs with similar particle sizes to those of their companion RACs (i.e. 12 mm nominal maximum size) were selected. All natural coarse aggregates were also pre-oven dried for 24 hours at 105˚C and subsequently cooled at ambient temperature for more than three hours before mixing of the concrete. The natural sand with a maximum nominal size of 0.4 mm was supplied from Price Pit (Yorke Peninsula), and used as the fine aggregate for all concrete mixes. The natural sand used in the present study had a water absorption of 0.82%, and an oven-dried bulk density of 1520 kg/m^3.

2.2.2 Cementitious binder

Two types of cementitious binder materials were used in this study, namely ordinary Portland cement, and silica fume. The chemical compositions and physical properties of these binders are supplied in Table 2.

2.2.3 FRP tubes

The FRP tubes of all CFFT specimens were manufactured using a manual wet lay-up process by wrapping epoxy resin-impregnated fiber sheets around precision-cut high-density Styrofoam templates in the hoop direction. The epoxy resin was allowed to cure at room temperature for at least 24 hours before the FRP tubes were removed from their molds. The number of FRP plies of each specimen was calculated using the models proposed by Lim and

Ozbakkaloglu [25, 34] to achieve a sufficient amount of confinement that would lead to axial stress-strain curve with ascending second branch.

CFFTs were manufactured using a single length of FRP sheet wrapped continuously in the hoop direction, creating an overlap length of 150 mm that was supplied to prevent premature debonding failure. The material properties of the FRP sheets were obtained through flat coupon tests performed in accordance with ASTM standard D3039M-08 [35]. Table 3 provides the manufacturer-supplied properties of the unidirectional fiber sheets and epoxy resin used in the manufacture of both the BFRP and CFRP tubes, together with the properties of the BFRP and CFRP composites obtained from flat coupon tests, calculated based on nominal fiber thicknesses.

2.2.4 Concretes

As shown in Table 4, a total of six concrete mixes prepared in the present study – , including three batches of NSC mixes, and three batches HSC mixes, were mixed by two-stage mixing approach proposed by Tam et al. [36], and designed to have different water-to-binder ratios (*w/b*) and RCA replacement ratios (*RCA%*). Through proper adjustments of the selected parameters in mix proportions of the concrete, an equivalent 28-day unconfined strength (f'_c) of 40 MPa for NSC and 70 MPa for HSC were achieved. In Table 4, the term "water-effective" is defined as the amount of water that was available for reaction with binder material. The "water-total" reported in Table 4 was the total water added to each mix, and it consisted of the effective water and saturation water that was absorbed by fine and coarse aggregates. The effective *w/b* and total *w/b* ratios given in Table 4 were calculated based on the effective and total water amounts for each mix, respectively. The mixing process of all

the concrete in this study is in accordance to the method previously reported by Xie and Ozbakkaloglu [37].

2.3 Specimen designation

The specimens in Tables 6 to 9 were labeled as follows: Each label started with letter N and letters H for normal- and high- strength concrete mix, respectively. The following letter was used to represent the sectional shape of each CFFT, either C (for circular specimen) or S (for square specimen). This was followed by a subsequent letter (i.e. either C (for carbon fiber) or B (for basalt fiber)) that was used to indicate the type of FRP used for each specimen. The following number was used to indicate the ply number of FRP confinement. These were followed by a number that indicated the replacement ratio (in percentage) of RAC to NA in the concrete. Finally, the last number in the specimen designation (i.e., 1, 2 or 3) was used to distinguish three nominally identical specimens. For example, N-S-B5-50-1 is the first of the three identical normal-strength square CFFT specimens that were confined by 5 plies BFRP with a RCA replacement ratio of 50%.

2.4 Instrumentation and testing

As shown in Figs. 1 (a) and (b), axial deformations of the specimens were measured with four linear variable displacement transformers (LVDTs), which were mounted at the corners between the loading and supporting steel plates of the compression test machine as shown in Fig. 1. The average axial strains along the height of the specimens were calculated by using the recorded deformations. Additional four LVDTs were placed at the mid-height at a gauge length of 175 mm at 90 degree spacing along the circumference of specimens to measure the axial deformation of the middle portion of the specimens. Furthermore, the specimens were instrumented with two unidirectional strain gauges at the mid-height to measure axial strains,

which were used to validate LVDT measurements at the early stages of loading. For all specimens, the hoops strains recorded on FRP tubes were obtained from six unidirectional strain gauges with a 5-mm gauge length. In circular CFFTs, these strain gauges were spaced equally around the perimeter at the mid-height of the specimen, outside the overlap region. In square CFFTs, four of the six gauges were installed at the mid-span of each face of the specimen, and the remaining two gauges were placed on two opposite corners of the specimens.

The specimens were tested under axial compression using a 5,000-kN capacity universal testing machine. The loading was initially applied with load control at 3 kN per second, whereas displacement control was used at approximately 0.003 mm per second beyond the initial softening until specimen failure. Prior to testing, all specimens were ground at both ends to ensure uniform distribution of the applied load on specimen cross-section.

3. TEST RESULTS AND DISCUSSION

3.1 Unconfined specimens

The compressive strengths (f'_{co}) of the unconfined concrete of the present study were obtained through axial compression tests that were performed in accordance with ASTM standard C39/C39M-05 [38]. Table 5 presents the compressive strengths (f'_{co}) of these unconfined concrete. As can be seen from the test results given in Table 5, a comparable compressive strength (f'_{co}) was achieved for each concrete grade (i.e. 40 MPa for NSC and 70 MPa for HSC, respectively) at the concrete age of 28 days. It has been well-established in previous studies that the unconfined strength (f'_{co}) of RAC decreases with an increase in the RCA replacement ratio for a given effective *w/b* ratio, [39-42]. Therefore, in the present

study, the *w/b* ratios of the concrete mixes were progressively reduced with an increase in *RCA%* of the mix. This can be seen in Table 5.

In addition, the axial strains at peak stress (ε_{co}) of each concrete reported are given in Table 5 and were determined using two unidirectional strain gauges with 80 mm gauge-length placed along the mid-height region of each specimen. As can be seen from the results of axial strain at peak stress (ε_{co}) reported in Table 5, at a same compressive strength (f'_{co}), RACs with a lower *RCA%* consistently exhibited lower axial strains at peak stress (ε_{co}) compared to those of the companion RACs with higher *RCA%*. This observation accords with those reported in previous studies on unconfined RACs [43, 44] and it indicates that an increase in the recycled aggregate content results in increased strain-softening in concrete under compression. This can be attributed to the porous nature of recycled aggregate, which results in reduced stiffness of the concrete manufactured using it [45, 46]. It is also evident from Table 5, as expected, at a given RCA replacement ratio, the axial strains at peak stress (ε_{co}) increase with an increase in the concrete strength.

The elastic modulus (E_c) of the unconfined concrete was also established through the compression tests performed in accordance with the ASTM standard C469/C469M-14 [47]. The results of these tests are reported in Table 5. It can be seen from these results that, at the same compressive strength, the elastic modulus decreased with an increase in *RCA%* for both NSC and HSC mixes. This finding is in agreement with those reported previously [48, 49]. It is well understood that the modulus of elasticity has a strong correlation with the compressive strength of the concrete, as well as the volumetric proportion and quality of aggregates used in the concrete mix [50-52]. Therefore, the reduction in elastic modulus of the concretes of

the same compressive strength with an increase in *RAC%* can be explained by the inferior mechanical properties of the RCAs compared to those of the NAs.

3.2 Confined specimens

3.2.1 Failure mode

The typical failure modes of normal- and high-strength CFFTs are presented in Figs. 3 and 4, respectively. The observed failure mode of all CFFTs was rupture of the FRP tube concomitant with a sudden loss of applied load, except for specimen N-C-B3-100-2 that experienced a premature FRP debonding failure. As can be seen in these figures, the rupture of FRP tubes occurred at the mid-height region of the CFFTs, and in the case of square specimens the rupture of the FRP tube took place at or near one of the corners of the specimen. Compared to circular CFFTs, in square CFFTs the rupture of the FRP tube was more localized and was isolated to a smaller section along the height of the specimen.

3.2.2 Axial stresses and strains

Figures 5 (a) to (b) illustrate the different stages typically observed on axial stress–strain curves of the specimens of the present study with and without post-peak strain softening regions, respectively. The notation and definitions introduced in these figures are used consistently throughout the discussion presented in this paper. The summary of the key experimental results are shown in Tables 7 to 8. Table 7 presents the recorded axial stresses, which include: the compressive strength (f'_{cc}), initial peak stress (f'_{c1}) that marks the point of transition from the initial ascending branch to the softening region of the second branch (Fig. 5 (a)), stress at plateau formation (f'_{c2}) that marks the point of transition from softening to hardening region on the second branch of the stress-strain curve (Fig. 5(a)), and strength enhancement ratio (f'_{cc}/f'_{co}).

Table 8 shows the recorded ultimate axial strains (ε_{cu}) and strain enhancement ratio ($\varepsilon_{cu}/\varepsilon_{co}$) of the specimens. The ultimate axial strains (ε_{cu}) reported in Table 8 were obtained at specimen failure, either from a set of four full-height LVDTs that measured the displacements along the entire height of the specimen (referred to as FLVDT in Table 8), or a set of four cage LVDTs that were used to measure the displacements along the mid-height region of the specimen (referred to as MLVDT in Table 8). The comparisons of the strains obtained from these two measurement methods are also presented in the same table as the ratio of MLVDT/FLVDT.

A closer investigation of the results given in Tables 7 to 8 leads to a number of important observations on the ultimate condition of the specimens. The results firstly show that an increase in the RCA content often resulted in a slight decrease in the strength and strain enhancement ratios (f'_{cc}/f'_{co} and $\varepsilon_{cu}/\varepsilon_{co}$, respectively), and an increase in the ultimate axial strain (ε_{cu}) of the CFFTs. The results also show that, at a similar confinement ratio (f_l/f'_{co}), CFFTs manufactured with CFRP tubes developed a significantly higher axial compressive strength (f'_{cc}) and a lower ultimate axial strain (ε_{cu}) compared to CFFTs manufactured with BFRP tubes. It is also evident from Tables 7 and 8 that, at a similar confinement ratio (f_l/f'_{co}), the H-C-B6 series HSC CFFTs exhibited a slightly lower strength enhancement ratio (f'_{cc}/f'_{co}) and a significantly lower strain enhancement ratio ($\varepsilon_{cu}/\varepsilon_{co}$) compared to those of the companion N-C-B3 series NSC CFFTs.

The results presented in Table 8 show that the difference in axial strains recorded by MLVDT and FLVDT tended to increase with an increase in the unconfined concrete strength (f'_{co}). This finding is in support of those reported in previous studies on FRP-confined concrete [23,

53, 54], which attributed this change to the change in the concrete cracking pattern as a result of increased concrete brittleness with an increase in concrete strength. The test results given in Table 8 also indicate that the MLVDT/FLVDT ratio decreased with an increase in *RCA%* for the CFFTs with the same in-place concrete strength. This observation, therefore, suggests that the cracking behavior of concrete of a given unconfined concrete strength changes with *RCA%*.

In the following sections, the axial strains obtained from full-height LVDTs are used in the discussions on ultimate axial strains (ε_{cu}), as they represent the overall specimen behavior more accurately than mid-height LVDTs.

3.2.3 Hoop strains

The FRP hoop rupture strains ($\varepsilon_{h,rup}$) of the specimens of the present study, which were averaged from six strain gauges placed at specimen mid-height outside the overlap region, are shown in Table 9. FRP hoop strain reduction factors ($k_{\varepsilon,exp}$) calculated from Eq.(1) based on recorded hoop rupture strains are also given in the same table.

$$k_{\varepsilon,exp} = \frac{\varepsilon_{h,rup}}{\varepsilon_{fu}} \tag{1}$$

In Eq. (1), $\varepsilon_{h,rup}$ is the experimentally-recorded FRP hoop-rupture strain, and ε_{fu} is the ultimate tensile strain of fibers. In addition, theoretical values of FRP hoop strain-reduction factors ($k_{\varepsilon,theo}$) calculated using Eq.2, proposed by Lim and Ozbakkaloglu [25] for FRP-confined concrete in circular section, are also shown in Table 9.

$$k_{\varepsilon,theo} = 0.9 - 2.3\, f'_{co} \times 10^{-3} - 0.75 E_f \times 10^{-6} \tag{2}$$

In Eq. (2), f'_{co} is the axial compressive strength of the unconfined concrete in MPa, and E_f is the elastic modulus of the fiber material in MPa, where 100,000 MPa ≤ Ef ≤ 640,000 MPa.

The results shown in Table 9 indicate that circular CFFTs with a higher *RCA%* developed lower hoop rupture strains ($\varepsilon_{h,rup}$) than their companions with a lower *RCA%*. This is attributable to the change in the cracking behavior of concrete with a change in the *RCA%*, as discussed in Section 3.2.2. It is also evident from Table 9 that square CFFTs exhibited lower hoop rupture strains compared to those of the companion circular CFFTs having the same in-place concrete strength and RCA content. This can be explained by stress concentrations that develop at the corners of square FRP tubes and results in earlier rupture of the tube. As can be seen from the results reported in Table 9, at a similar confinement ratio (f_l/f'_{co}), CFFTs manufactured with CFRP tubes developed lower FRP hoop strain reduction factors ($k_{\varepsilon,exp}$) than those of the companion CFFTs manufactured with BFRP tubes. It can also be seen from the same table that the model in Eq. (2) successfully captured the reduction in $k_{\varepsilon,exp}$ with an increase in E_f (i.e. from BFRP to CFRP). The results also show that HSCFFTs consistently had lower hoop rupture strains ($\varepsilon_{h,rup}$) compared to those of their NSCFFT counterparts. The comparison of the experimental and theoretical values of FRP hoop strain-reduction factors ($k_{\varepsilon,exp}$ and $k_{\varepsilon,theo}$) in Table 8 also indicates that Eq. (2) provides conservative estimates of $k_{\varepsilon,exp}$ for the circular specimens with 0% replacement ratio and close estimates for the specimens with 50% and 100% RCA replacement ratios.

3.2.4 Influence of test parameters on observed behavior

Figures 6 to 9 illustrate the stress-strain curves of the CFFT of the present study. It can be seen from these figures, owing to the application of sufficient amount of confinement, all the sufficiently confined circular specimens exhibited a monotonically ascending curve, which

consists of a parabolic first ascending portion and a nearly linear second branch, whereas stress–strain curves of the square specimens had an almost horizontal second branch with only minimal tendency to ascend due to the less-effective confinement offered by the square FRP tubes compared to the circular FRP tubes. In addition, it is now understood that FRP-confined HSC specimens may exhibit a sudden drop in their axial load capacity and corresponding axial stress immediately after the initial peak condition on their stress-strain relationship. This behavior, which is caused by the brittle nature of HSC and was discussed in detail previously [17, 22, 24], was also observed in the RAHSCFFTs of the present study. Detailed discussions on the influence of each test parameter on the compressive behavior of CFFTs are presented in the following sections.

3.2.4.1 Effect of RCA replacement ratio

To investigate the influence of RCA replacement ratio on the axial compressive behavior of the CFFTs, comparisons were conducted among the specimens prepared using different content of RCAs. As can be seen from the axial stress-strain curves shown in Figs. 10 (a) to (d) and the results reported in Table 7, the compressive strengths (f'_{cc}) of the CFFTs decreased with an increase in the RCA replacement ratio. This observation can be explained by the fact that, as noted previously, hoop rupture strains ($\varepsilon_{h,rup}$) of CFFTs decreased with an increase in *RCA%*, which in turn resulted in lower confining pressures applied by the FRP tube to concrete. It is also evident from stress-strain curves illustrated in Figs. 10 (a) to (d) and the results presented in Table 8 that an increased RCA content led to a slight increase in the ultimate axial strain (ε_{cu}) in each group of CFFTs. This increase is consistent with the previously noted increase seen in ε_{co} of the unconfined specimens, and it can be attributed to the increased strain softening experienced by the concretes having higher RCA contents. In addition, it can be seen from Fig. 10 (a) to (d) that the length of the transition region, which

connects the first and second branches of the axial stress-strain curves as marked in Fig. 5, generally increased with an increase in *RCA%*. This observation is in support of that the CFFTs prepared with a higher *RCA%* exhibited a more progressive softening behavior. On the other hand, as can be seen in Table 8, the axial strain enhancement ratio ($\varepsilon_{cu}/\varepsilon_{co}$) of the CFFTs decreased with an increase in *RCA%*, which indicates that an increase in RCA% resulted in a less significant increase in ε_{cu} of the confined specimens than it did in ε_{co} of the companion unconfined specimens. Finally, it can be concluded from the observations presented in this section that an increase in the RCA content results in a decrease in the dilation rate of CFFTs, which is contributed by their reduced hoop strains and increased axial strains.

3.2.4.2 Effect of specimens cross-sectional shape

The influence of specimen cross-sectional shape on the axial compressive behavior of the CFFTs can be studied through the comparison of N-C-B and N-S-B series CFFTs. Circular and square CFFTs were provided with 3- and 5-layer FRP tubes, respectively, to allow for the difference in their confinement effectiveness [34]. As can be seen from the stress-strain curves illustrated in Fig. 11 (a) to (c), square CFFTs exhibited a flatter and a slightly longer second branch compared to that of the companion circular CFFTs. This contributed to the lower compressive strength (f'_{cc}) and higher ultimate axial strain (ε_{cu}) of the former series. As can be seen from Figs. 11 (a) to (c), the difference in the compressive strengths (f'_{cc}) of circular and square CFFTs increased with an increase in RAC content. This can be associated with the more significant decreases seen in second branch slopes of the axial stress-strain curves of square CFFTs with an increase in *RCA%* compared those in circular CFFTs. It can also be seen in Figs. 11 (a) to (c) that *RCA%* influenced the ultimate axial strain (ε_{cu}) of square and circular CFFTs similarly.

3.2.4.3 Effect of FRP type

To investigate the influence of FRP type on the compressive behavior of CFFTs, comparisons were conducted between H-C-B6 and H-C-C3 series CFFTs, which had similar confinement ratios (f_l/f'_{co}). The axial stress-strain curves illustrated in Figs.12 (a) to (c) and the results summarized in Tables 7 and 8, show that H-C-C3 series CFFTs manufactured with CFRP exhibited higher compressive strengths (f'_{cc}) and lower ultimate axial strains (ε_{cu}) compared to those of the companion H-C-B6 series CFFTs manufactured with BFRP. It is evident from the axial stress-strain curves given in Figs. 12 (a) to (c) that the influence of FRP type on the compressive behaviors of the CFFTs varied with the RCA content. It can be seen from these figures that the difference in compressive strengths (f'_{cc}) of CFFTs provided with CFRP and BFRP tubes increased with an increase in *RCA%*, which was contributed by more significant decreases seen in the second branch axial stress-strain curve slopes of CFFTs manufactured with CFRP tubes with an increase in *RCA%*, compared to those of companion CFFTs with BFRP tubes.

3.2.4.4 Effect of concrete strength

Figs. 13 (a) to (c) illustrate the influence of concrete strength on the compressive behavior of CFFTs. The comparisons shown in these figures indicate that, at a similar confinement ratio (f_l/f'_{co}), H-C-B series HSCFFTs exhibited lower strength enhancement ratios (f'_{cc}/f'_{co}) compared to those of the companion N-C-B series NSCFFTs. As can be seen in Figs. 13(a) to (c), ultimate axial strains (ε_{cu}) and hoop rupture strains ($\varepsilon_{h,rup}$) of HSCFFTs were also slightly lower than those of NSCFFTs. These observations are consistent with the findings of previous studies on the compressive behavior of FRP-confined NSC and HSC [17, 27, 54, 55]. Figure 13 also shows that, at each *RCA%*, HSCFFTs exhibited larger post-strength losses,

defined as the difference between f'_{c1} and f'_{c2} as illustrated in Fig.5, compared to those of the companion NSCFFTs. This observation, which is in agreement with those reported in a number of previous studies on CFFTs [17, 22, 24], can be attributed to the increased brittleness of concrete with an increase in its unconfined strength. Finally, the curves shown in Fig.13 indicate that the relationship between the NSC and HSC specimens was not affected significantly by *RCA%*.

5. CONCLUSIONS

This paper has reported the results of an experimental study on the axial compressive behavior of CFFTs manufactured with coarse RCAs of different contents. Based on the results and discussions presented in this study, the following conclusions can be drawn：

1. An increase in the RCA replacement ratio leads to a decrease in the compressive strength (f'_{cc}) and hoop rupture strain ($\varepsilon_{h,rup}$), and an increase in the ultimate axial strain (ε_{cu}) of CFFTs of the same in-place concrete strength.
2. The difference between ultimate axial strains measured using LVDTs mounted on CFFTs at their mid-height (MLVDT) and LVDTs mounted along the full height of specimens (FLVDT) increases with an increase in the RCA replacement ratio.
3. Under a similar effective confinement level, square CFFTs exhibit lower compressive strengths (f'_{cc}) and higher ultimate axial strains (ε_{cu}) compared to those of companion circular CFFTs. In addition, the difference in the compressive strengths (f'_{cc}) of circular and square CFFTs increases with an increase in RAC content.
4. At a given confinement ratio, CFFTs with CFRP tubes exhibit higher compressive strengths (f'_{cc}) and lower ultimate axial strains (ε_{cu}) compared to those of companion CFFTs with BFRP tubes. Furthermore, it has been observed that, compared to CFFTs with BFRP tubes, CFFTs with CFRP tubes exhibited a more significant decrease in their

second branch axial stress-strain curve slopes with an increase in *RCA%*.

5. At a given confinement ratio, the strength enhancement ratio (f'_{cc}/f'_{co}), ultimate axial strain (ε_{cu}) and hoop rupture strain ($\varepsilon_{h,rup}$) of CFFTs decrease with an increase in the unconfined concrete strength. The relative performance of NSC and HSC CFFTs is not affected significantly by their RCA content.

6. REFERENCES

[1] Elhakam, A. A., Mohamed, A. E., and Awad, E. (2012). Influence of self-healing, mixing method and adding silica fume on mechanical properties of recycled aggregates concrete. *Construction and Building Materials*, *35*, 421-427.

[2] Limbachiya, M., Meddah, M. S., and Ouchagour, Y. (2012). Use of recycled concrete aggregate in fly-ash concrete. *Construction and Building Materials*,*27*(1), 439-449.

[3] Limbachiya, M., Meddah, M. S., and Ouchagour, Y. (2012). Performance of Portland/silica fume cement concrete produced with recycled concrete aggregate. *ACI Materials Journal*, *109*(1).

[4] Mas, B., Cladera, A., del Olmo, T., and Pitarch, F. (2012). Influence of the amount of mixed recycled aggregates on the properties of concrete for non-structural use. *Construction and Building Materials*, *27*(1), 612-622.

[5] Sheen, Y. N., Wang, H. Y., Juang, Y. P., and Le, D. H. (2013). Assessment on the engineering properties of ready-mixed concrete using recycled aggregates. *Construction and Building Materials*, *45*, 298-305.

[6] Ajdukiewicz, A., and Kliszczewicz, A. (2002). Influence of recycled aggregates on mechanical properties of HS/HPC. *Cement and concrete composites*, *24*(2), 269-279.

[7] Rahal, K. (2007). Mechanical properties of concrete with recycled coarse aggregate. *Building and environment*, *42*(1), 407-415.

[8] Malešev, M., Radonjanin, V., and Marinković, S. (2010). Recycled concrete as aggregate for structural concrete production. *Sustainability*, *2*(5), 1204-1225.

[9] Rao, M. C., Bhattacharyya, S. K., and Barai, S. V. (2011). Influence of field recycled coarse aggregate on properties of concrete. *Materials and Structures*,*44*(1), 205-220.

[10] Kou, S. C., and Poon, C. S. (2012). Enhancing the durability properties of concrete prepared with coarse recycled aggregate. *Construction and Building Materials*, *35*, 69-76.

[11] Lam, L., and Teng, J. G. (2004). Ultimate condition of fiber reinforced polymer-confined concrete. *Journal of Composites for Construction*, *8*(6), 539-548.

[12] Ilki, A., Peker, O., Karamuk, E., Demir, C., and Kumbasar, N. (2008). FRP retrofit of low and medium strength circular and rectangular reinforced concrete columns. *Journal of Materials in Civil Engineering*, *20*(2), 169-188.

[13] Rousakis, T. C. and Karabinis, A. I. (2012). "Adequately FRP confined reinforced concrete columns under axial compressive monotonic or cyclic loading." *Materials and Structures*, 45(7), 957-975.

[14] Kusumawardaningsih, Y., and Hadi, M. N. S. (2010). Comparative behaviour of hollow columns confined with FRP composites. *Composite Structures*, *93*(1), 198-205.

[15] Wu, Y. F., and Wei, Y. Y. (2010). Effect of cross-sectional aspect ratio on the strength of CFRP-confined rectangular concrete columns. *Engineering Structures*, 32(1), 32-45.

[16] Dai, J. G., Bai, Y. L., and Teng, J. G. (2011). Behavior and modeling of concrete confined with FRP composites of large deformability. *Journal of Composites for Construction*, *15*(6), 963-973.

[17] Wang, Z., Wang, D., Smith, S. T., and Lu, D. (2011). CFRP-confined square RC columns. I: Experimental investigation. *Journal of Composites for Construction*, *16*(2), 150-160.

[18] Ozbakkaloglu, T., and Akin, E. (2012). Behavior of FRP-confined normal-and high-strength concrete under cyclic axial compression. *Journal of Composites for Construction*, *16*(4), 451-463.

[19] Mirmiran, A., Shahawy, M., Samaan, M., Echary, H. E., Mastrapa, J. C., and Pico, O. (1998). Effect of column parameters on FRP-confined concrete. *Journal of Composites for Construction*, *2*(4), 175-185.

[20] Fam, A., Schnerch, D., and Rizkalla, S. (2005). Rectangular filament-wound glass fiber reinforced polymer tubes filled with concrete under flexural and axial loading: Experimental investigation. *Journal of Composites for Construction*, *9*(1), 25-33.

[21] Park, J. H., Jo, B. W., Yoon, S. J., and Park, S. K. (2011). Experimental investigation on the structural behavior of concrete filled FRP tubes with/without steel re-bar. *KSCE Journal of Civil Engineering*, *15*(2), 337-345.

[22] Ozbakkaloglu, T. (2013). Compressive behavior of concrete-filled FRP tube columns: Assessment of critical column parameters. *Engineering Structures*, *51*, 188-199.

[23] Ozbakkaloglu, T. (2013). Concrete-filled FRP tubes: manufacture and testing of new forms designed for improved performance. *Journal of Composites for Construction*, *17*(2), 280-291.

[24] Lim, J. C., and Ozbakkaloglu, T. (2015). Influence of Concrete Age on Stress-Strain Behavior of FRP-Confined Normal- and High-Strength Concrete. *Construction and Building Materials*, 82, 61-70.

[25] Vincent, T., and Ozbakkaloglu, T. (2015). Influence of shrinkage on compressive behavior of concrete-filled FRP tubes: An experimental study on interface gap effect. *Construction and Building Materials*, 75, 144-156.

[26] Xie, T., and Ozbakkaloglu, T. (2015). Behavior of steel fiber-reinforced high-strength concrete-filled FRP tube columns under axial compression. *Engineering Structures*, 90, 158-171.

[27] Ozbakkaloglu, T., and Lim, J. C. (2013). Axial compressive behavior of FRP-confine concrete: Experimental test database and a new design-oriented model. *Composites Part B: Engineering*, 55, 607-634.

[28] Ozbakkaloglu, T., Lim, J. C. and Vincent, T. (2013). FRP-confined concrete in circular sections: Review and assessment of stress–strain models. *Engineering Structures*, 49, 1068–1088.

[29] Lim, J. C. and Ozbakkaloglu, T. (2014). Confinement model for FRP-confined high-strength concrete. *Journal of Composites for Construction, ASCE*, 17(5), 1-19.

[30] Lim, J. C. and Ozbakkaloglu, T. (2014). Lateral strain-to-axial strain relationship of confined concrete. *Journal of Structural Engineering, ASCE*, Doi: 10.1061/(ASCE)ST.1943-541X.0001094.

[31] Xiao, J., Huang, Y., Yang, J., and Zhang, C. (2012). Mechanical properties of confined recycled aggregate concrete under axial compression. *Construction and Building Materials*, *26*(1), 591-603.

[32] Xiao, J., Tresserras, J., and Tam, V. W. (2014). GFRP-tube confined RAC under axial and eccentric loading with and without expansive agent. *Construction and Building Materials*, *73*, 575-585.

[33] Zhao, J. L., Yu, T., and Teng, J. G. (2014). Stress-strain behavior of FRP-confined recycled aggregate concrete. *Journal of Composites for Construction*, *19*(3), 04014054.

[34] Islam, M. M., Choudhury, M. S. I., and Amin, A. F. M. S. (2015). Dilation Effects in FRP-Confined Square Concrete Columns Using Stone, Brick, and Recycled Coarse Aggregates. *Journal of Composites for Construction*, 04015017.

[35] Louk Fanggi, B. A., and Ozbakkaloglu, T. (2015). Behavior of Hollow and Concrete-Filled FRP-HSC and FRP-HSC-Steel Composite Columns Subjected to Concentric Compression. *Advances in Structural Engineering*, *18*(5), 715-738.

[36] Lim, J. C., and Ozbakkaloglu, T. (2015). Influence of concrete age on stress–strain behavior of FRP-confined normal-and high-strength concrete.*Construction and Building Materials*, *82*, 61-70.

[37] Vincent, T., and Ozbakkaloglu, T. (2015). Compressive behavior of prestressed high-strength concrete-filled aramid FRP tube columns: Experimental observations. *Journal of Composites for Construction*.

[38] Lim, J. C., and Ozbakkaloglu, T. (2014). Design model for FRP-confined normal-and high-strength concrete square and rectangular columns. *Mag. Concr. Res*,*66*(20), 1020-1035.

[39] ASTM. (2008). "Standard test method for tensile properties of polymer matrix composites materials." D3039M-08, West Conshohocken, PA.

[40] Tam, V. W., Gao, X. F., and Tam, C. M. (2005). Microstructural analysis of recycled aggregate concrete produced from two-stage mixing approach.*Cement and Concrete Research*, *35*(6), 1195-1203.

[41] Xie, T., and Ozbakkaloglu, T. (2015). Influence of Recycled Aggregate Size and Content on Behavior of Recycled Aggregate Concrete. *Journal of Cleaner Production, (accepted)*.

[42] ASTM. (2005). Standard Test Method for Compressive Strength of Cylindrical Concrete Specimens, C39/C39M-05, West Conshohocken, PA**.**

[43] Belén, G. F., Fernando, M. A., Diego, C. L., and Sindy, S. P. (2011). Stress–strain relationship in axial compression for concrete using recycled saturated coarse aggregate. *Construction and Building Materials*, *25*(5), 2335-2342.

[44] Wang, Z., Wang, L., Cui, Z., and Zhou, M. (2011). Effect of recycled coarse aggregate on concrete compressive strength. *Transactions of Tianjin University*, *17*, 229-234.

[45] Choi, W. C., and Yun, H. D. (2012). Compressive behavior of reinforced concrete columns with recycled aggregate under uniaxial loading. *Engineering Structures*, *41*, 285-293

[46] Ulloa, V. A., García-Taengua, E., Pelufo, M. J., Domingo, A., and Serna, P. (2013). New views on effect of recycled aggregates on concrete compressive strength. *ACI Materials Journal*, *110*(6).

[47] Otsuki, N., Miyazato, S. I., and Yodsudjai, W. (2003). Influence of recycled aggregate on interfacial transition zone, strength, chloride penetration and carbonation of concrete. *Journal of Materials in Civil Engineering*, *15*(5), 443-451.

[48] Liu, Q., Xiao, J., and Sun, Z. (2011). Experimental study on the failure mechanism of recycled concrete. *Cement and Concrete Research*, *41*(10), 1050-1057.

[49] Behera, M., Bhattacharyya, S. K., Minocha, A. K., Deoliya, R., and Maiti, S. (2014). Recycled aggregate from C&D waste & its use in concrete–A breakthrough towards sustainability in construction sector: A review.*Construction and building materials*, *68*, 501-516.

[50] Folino, P., and Xargay, H. (2014). Recycled aggregate concrete–Mechanical behavior under uniaxial and triaxial compression. *Construction and Building Materials*, *56*, 21-31.

[51] ASTM. (2014). Standard Test Method for Static Modulus of Elasticity and Poisson's Ratio of Concrete in Compression, C469 / C469M - 14, West Conshohocken, PA

[52] Butler, L., West, J. S., and Tighe, S. L. (2013). Effect of recycled concrete coarse aggregate from multiple sources on the hardened properties of concrete with equivalent compressive strength. *Construction and Building Materials*, *47*, 1292-1301.

[53] Etxeberria, M., V ázquez, E., Mar í, A., and Barra, M. (2007). Influence of amount of recycled coarse aggregates and production process on properties of recycled aggregate concrete. *Cement and Concrete Research*, *37*(5), 735-742.

[54] Zhou, F. P., Lydon, F. D., and Barr, B. I. G. (1995). Effect of coarse aggregate on elastic modulus and compressive strength of high performance concrete. *Cement and Concrete Research*, *25*(1), 177-186.

[55] Yang, C. C. (1998). Effect of the transition zone on the elastic moduli of mortar. *Cement and Concrete Research*, *28*(5), 727-736.

[56] Li, G., Zhao, Y., Pang, S. S., and Li, Y. (1999). Effective Young's modulus estimation of concrete. *Cement and Concrete Research*, *29*(9), 1455-1462.

[57] Lim, J. and Ozbakkaloglu, T. (2014). Influence of silica fume on stress–strain behavior of FRP-confined HSC. *Construction and Building Materials*, 63, 11-24.

[58] Vincent, T., and Ozbakkaloglu, T. (2014). Axial Strains in FRP-Confined Normal-and High-Strength Concrete: An Examination of Strain Measurement Methods. In *Advanced Materials Research* (Vol. 919, pp. 23-28).

[59] Pacheco-Torgal, F., Ding, Y., and Jalali, S. (2012). Properties and durability of concrete containing polymeric wastes (tyre rubber and polyethylene terephthalate bottles): An overview. *Construction and Building Materials*, *30*, 714-724.

[60] Ahmed, S. F. U. (2013). Existence of Dividing Strength in Concrete Containing Recycled Coarse Aggregate. *Journal of Materials in Civil Engineering*, *26*(4), 784-788.

[61] Matias, D., de Brito, J., Rosa, A., and Pedro, D. (2013). Mechanical properties of concrete produced with recycled coarse aggregates–Influence of the use of superplasticizers. *Construction and Building Materials*, *44*, 101-109.

[62] Bairagi, N. K., Ravande, K., and Pareek, V. K. (1993). Behaviour of concrete with different proportions of natural and recycled aggregates. *Resources, conservation and recycling*, *9*(1), 109-126.

[63] Ozbakkaloglu, T. (2013). Behavior of square and rectangular ultra high-strength concrete-filled FRP tubes under axial compression. *Composites Part B: Engineering*, *54*, 97-111.

LIST OF TABLE CAPTIONS

Table 1. Properties of coarse aggregates

Aggregate type	Nominal maximum particle size (mm)	Oven-dried bulk density (g/cm^3)	Relative density (g/cm^3)	Apparent density (g/cm^3)	Water absorption (%)
NA	12	1.54	2.71	2.86	2.01
RCA	12	1.18	2.22	2.56	6.12

Table 2. Chemical composition and physical properties of cementitious materials

Item	Cementitious materials (%)	
	Ordinary Portland cement	Silica fume
SiO_2	21.4	92.5
$ZrO_2 + HfO_2$	-	5.50
Al_2O_3	5.55	0.35
Fe_2O_3	3.46	0.40
P_2O_5	-	0.30
CaO	64.0	0.03
MgO	1.86	-
SO_3	1.42	0.90
K_2O	0.54	0.02
Na_2O	0.26	0.02
	Compounds	
C_3S	51.0	-
C_2S	23.1	-
C_3A	8.85	-
C_4AF	10.5	-
	Fineness	
Surface area (m^2/kg)	330	18,000

Table 3. Material properties of fibers and FRP composites

Type	Nominal fiber thickness	Fiber/FRP properties					
		Provided by manufacturer			Obtained from coupon tests*		
		Ultimate tensile stress f_f (MPa)	Ultimate tensile strain ε_f (%)	Elastic modulus E_f (GPa)	Ultimate tensile stress f_{frp} (MPa)	Ultimate tensile strain ε_{frp} (%)	Elastic modulus E_{frp} (GPa)
Basalt fiber	0.140	1680	2.30	73	1584	2.10	76
Carbon fiber	0.111	4370	1.90	230	4152	1.80	236

*Calculated based on nominal thickness of fibers

Table 4. Mix proportions of concrete

	NSC			HSC		
RCA Replaced NA ratio	0%	50%	100%	0%	50%	100%
Cement (kg/m^3)	380	380	380	506	506	506
Silica Fume (kg/m^3)	0	0	0	44	44	44
Sand (kg/m^3)	710	710	710	710	710	710
Natural Aggregate (kg/m^3)	1065	533	0	1065	533	0
Recycled Aggregate (kg/m^3)	0	408	816	0	408	816
Water- Effective (kg/m^3)	209	194	179	175	164	159
Water- Total (kg/m^3)	237	236	235	201	205	214
Superplasticizer (kg/m^3)	0	0	0	7	7	7
Effective *w/b* ratio*	0.55	0.51	0.47	0.33	0.31	0.30
Total *w/b* ratio*	0.62	0.62	0.62	0.37	0.38	0.40
Slump (mm)	220	125	115	245	170	175

*Including the water coming from the superplasticizer (i.e. 70% water by weight)

Table 5. Compression test results of unconfined specimens

Concrete mix	f'_{co} (MPa)	E_c (GPa)	ε_{co} (%)
NSC 0%	37.2	27.3	0.19
NSC 50%	38.2	26.8	0.21
NSC 100%	36.6	23.4	0.25
HSC 0%	69.6	34.6	0.24
HSC 50%	68.9	34.0	0.26
HSC 100%	66.8	32.3	0.28

Table 6. Details of FRP confined specimens

Specimens	f'_{co} (MPa)	No. of FRP plies	FRP type	Cross sectional shape	RCA replacement ratio
N-C-B3-0	37.2	3	Basalt	Circular	0%
N-C-B3-50	38.2	3	Basalt	Circular	50%
N-C-B3-100	36.6	3	Basalt	Circular	100%
N-S-B5-0	37.2	5	Basalt	Square	0%
N-S-B5-50	38.2	5	Basalt	Square	50%
N-S-B5-100	36.6	5	Basalt	Square	100%
H-C-B6-0	69.6	6	Carbon	Circular	0%
H-C-B6-50	68.9	6	Carbon	Circular	50%
H-C-B6-100	66.8	6	Carbon	Circular	100%
H-C-C3-0	69.6	3	Carbon	Circular	0%
H-C-C3-50	68.9	3	Carbon	Circular	50%
H-C-C3-100	66.8	3	Carbon	Circular	100%

Table 7. Axial compressive strengths of confined specimens

Specimens	Avg. f'_{co} (MPa)	f'_{c1} (MPa)	f'_{c2} (MPa)	f'_{cc} (MPa)	f'_{cc}/f'_{co}	Avg. f'_{cc} (Mpa)	Avg. f'_{cc}/f'_{co}
N-C-B3-0-1		39.5	39.0	53.5	1.44		
N-C-B3-0-2	37.2	42.8	41.1	52.2	1.40	52.5	1.41
N-C-B3-0-3		41.8	41.7	51.8	1.39		
N-C-B3-50-1		43.9	41.3	50.2	1.31		
N-C-B3-50-2	38.2	44.9	44.2	51.4	1.35	50.8	1.33
N-C-B3-50-3		41.4	40.3	50.9	1.33		
N-C-B3-100-1	36.6	45.1	44.6	48.4	1.32	48.5	1.32
N-C-B3-100-3		45.4	43.1	48.6	1.33		
N-S-B5-0-1		45.0	41.8	48.2	1.29		
N-S-B5-0-2	37.2	41.4	41.2	47.1	1.27	47.8	1.28
N-S-B5-0-3		41.3	40.1	48.1	1.29		
N-S-B5-50-1		42.1	40.2	44.0	1.15		
N-S-B5-50-2	38.2	44.9	40.8	42.5	1.11	43.3	1.13
N-S-B5-50-3		40.6	39.6	43.3	1.13		
N-S-B5-100-1		42.6	39.2	41.7	1.14		
N-S-B5-100-2	36.6	43.4	40.5	40.9	1.12	41.6	1.14
N-S-B5-100-3		44.4	39.6	42.1	1.15		
H-C-B6-0-1		77.4	69.9	86.5	1.24		
H-C-B6-0-2	69.6	76.0	67.6	87.4	1.26	85.7	1.23
H-C-B6-0-3		78.4	68.7	83.3	1.20		
H-C-B6-50-1		73.0	64.1	80.8	1.17		
H-C-B6-50-2	68.9	73.2	63.7	82.5	1.20	82.3	1.19
H-C-B6-50-3		72.5	64.9	83.5	1.21		
H-C-B6-100-1		71.3	63.2	79.3	1.19		
H-C-B6-100-2	66.8	71.0	64.2	78.3	1.17	79.7	1.19
H-C-B6-100-3		71.6	64.5	81.5	1.22		
H-C-C3-0-1		73.1	69.8	92.8	1.33		
H-C-C3-0-2	69.6	74.4	72.8	96.6	1.39	94.9	1.36
H-C-C3-0-3		74.4	70.3	95.3	1.37		
H-C-C3-50-1		76.5	71.9	90.1	1.31		
H-C-C3-50-2	68.9	75.7	70.4	90.8	1.32	91.2	1.32
H-C-C3-50-3		74.9	73.1	92.9	1.35		
H-C-C3-100-1		74.4	71.3	85.1	1.27		
H-C-C3-100-2	66.8	76.4	70.9	83.0	1.24	83.9	1.26
H-C-C3-100-3		77.4	71.8	83.5	1.25		

Table 8. Axial strains of confined specimens

Specimens	ε_{cu} (%)		Avg. ε_{cu} (%)		MLVDT/ FLVDT	Avg. $\varepsilon_{cu}/\varepsilon_{co}$ *
	FLVDT	MLVDT	FLVDT	MLVDT		
N-C-B3-0-1	2.02	1.88				
N-C-B3-0-2	1.97	1.77	1.99	1.83	0.92	10.5
N-C-B3-0-3	1.98	1.83				
N-C-B3-50-1	2.10	1.81				
N-C-B3-50-2	2.08	1.72	2.11	1.76	0.84	10.0
N-C-B3-50-3	2.14	1.75				
N-C-B3-100-1	2.27	1.56	2.24	1.60	0.71	8.96
N-C-B3-100-3	2.21	1.63				
N-S-B5-0-1	2.25	2.02				
N-S-B5-0-2	2.18	2.07	2.21	2.06	0.93	11.6
N-S-B5-0-3	2.21	2.09				
N-S-B5-50-1	2.41	1.96				
N-S-B5-50-2	2.33	1.87	2.38	1.91	0.80	11.3
N-S-B5-50-3	2.40	1.91				
N-S-B5-100-1	2.57	1.54				
N-S-B5-100-2	2.51	1.39	2.53	1.55	0.61	10.1
N-S-B5-100-3	2.52	1.71				
H-C-B6-0-1	1.92	1.53				
H-C-B6-0-2	1.94	1.35	1.92	1.44	0.75	7.99
H-C-B6-0-3	1.89	1.43				
H-C-B6-50-1	2.02	1.31				
H-C-B6-50-2	1.94	1.32	1.97	1.30	0.66	7.58
H-C-B6-50-3	1.95	1.27				
H-C-B6-100-1	1.96	1.24				
H-C-B6-100-2	2.02	1.13	1.99	1.19	0.60	7.10
H-C-B6-100-3	1.98	1.20				
H-C-C3-0-1	1.47	1.31				
H-C-C3-0-2	1.43	1.27	1.46	1.30	0.89	6.10
H-C-C3-0-3	1.49	1.32				
H-C-C3-50-1	1.54	1.17				
H-C-C3-50-2	1.59	1.28	1.57	1.22	0.78	6.03
H-C-C3-50-3	1.57	1.22				
H-C-C3-100-1	1.64	1.09				
H-C-C3-100-2	1.66	1.14	1.64	1.12	0.68	5.85
H-C-C3-100-3	1.61	1.12				

*Ultimate axial strains (ε_{cu}) were determined from full-height LVDTs.

Table 9. FRP hoop rupture strains of confined specimens

Specimens	$\varepsilon_{h,rup}$ (%)	Avg. $\varepsilon_{h,rup}$ (%)	$k_{\varepsilon,exp}$	Avg. $k_{\varepsilon,exp}$	Avg. $k_{\varepsilon,theo}$
N-C-B3-0-1	1.80		0.86		
N-C-B3-0-2	1.84	1.83	0.88	0.87	0.76
N-C-B3-0-3	1.86		0.89		
N-C-B3-50-1	1.66		0.79		
N-C-B3-50-2	1.61	1.63	0.77	0.78	0.76
N-C-B3-50-3	1.63		0.78		
N-C-B3-100-1	1.50	1.56	0.71	0.74	0.76
N-C-B3-100-3	1.61		0.77		
N-S-B5-0-1	1.40		0.67		
N-S-B5-0-2	1.64	1.50	0.78	0.72	-
N-S-B5-0-3	1.47		0.70		
N-S-B5-50-1	1.39		0.66		
N-S-B5-50-2	1.42	1.41	0.68	0.67	-
N-S-B5-50-3	1.42		0.68		
N-S-B5-100-1	1.11		0.53		
N-S-B5-100-2	1.18	1.18	0.56	0.56	-
N-S-B5-100-3	1.24		0.59		
H-C-B6-0-1	1.57		0.75		
H-C-B6-0-2	1.58	1.57	0.75	0.75	0.69
H-C-B6-0-3	1.56		0.74		
H-C-B6-50-1	1.49		0.71		
H-C-B6-50-2	1.50	1.49	0.71	0.71	0.69
H-C-B6-50-3	1.47		0.70		
H-C-B6-100-1	1.30		0.62		
H-C-B6-100-2	1.35	1.33	0.64	0.63	0.69
H-C-B6-100-3	1.33		0.63		
H-C-C3-0-1	1.23		0.68		
H-C-C3-0-2	1.19	1.20	0.66	0.67	0.57
H-C-C3-0-3	1.19		0.66		
H-C-C3-50-1	1.09		0.61		
H-C-C3-50-2	1.08	1.07	0.60	0.60	0.57
H-C-C3-50-3	1.05		0.58		
H-C-C3-100-1	1.02		0.57		
H-C-C3-100-2	0.99	0.98	0.55	0.55	0.57
H-C-C3-100-3	0.94		0.52		

LIST OF FIGURE CAPTIONS

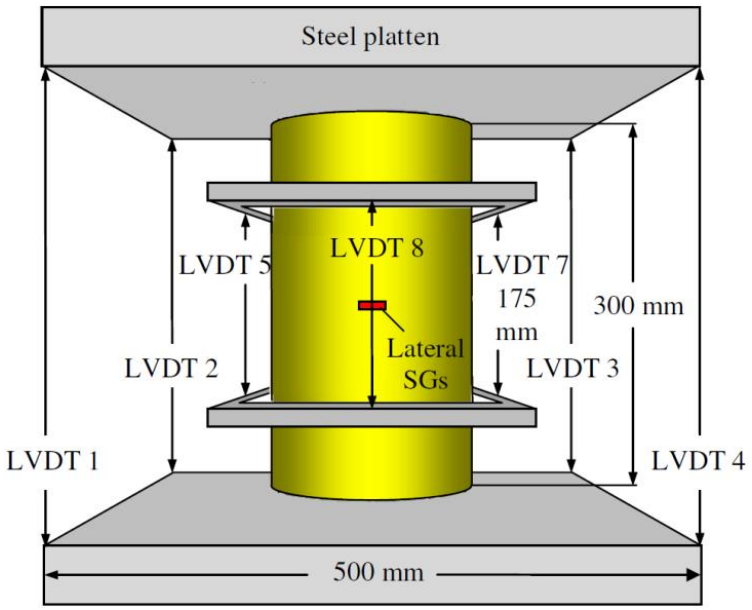

(a)

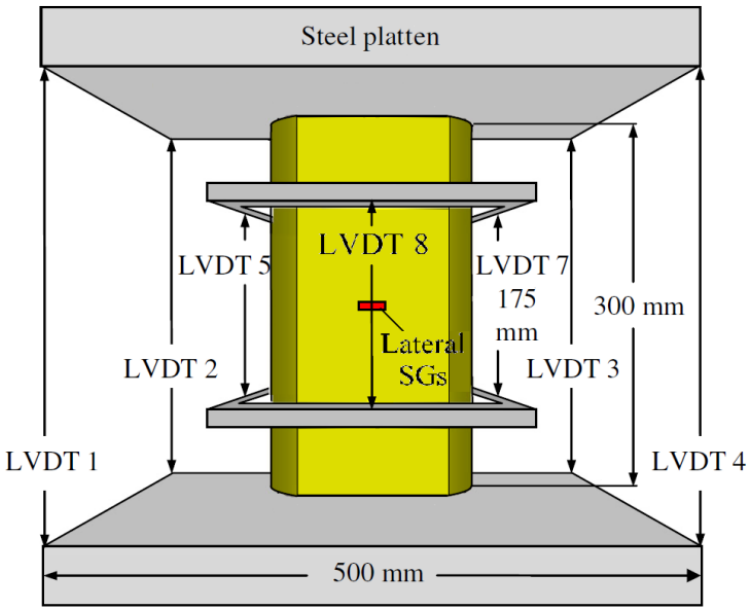

(b)

Figure 1. Test setup and instrumentation: (a) Circular specimens; (b) Square specimens.

(a) (b)

Figure 2. Coarse aggregates: a) RCA; b) NA

(a) (b) (c)

(c) (d) (e)

Figure 3. Failure modes of normal-strength CFFTs series: a) N-C-B-0; b) N-C-B-50; c) N-C-B-100; d) N-S-B-0; e) N-S-B-50; f) N-S-B-100

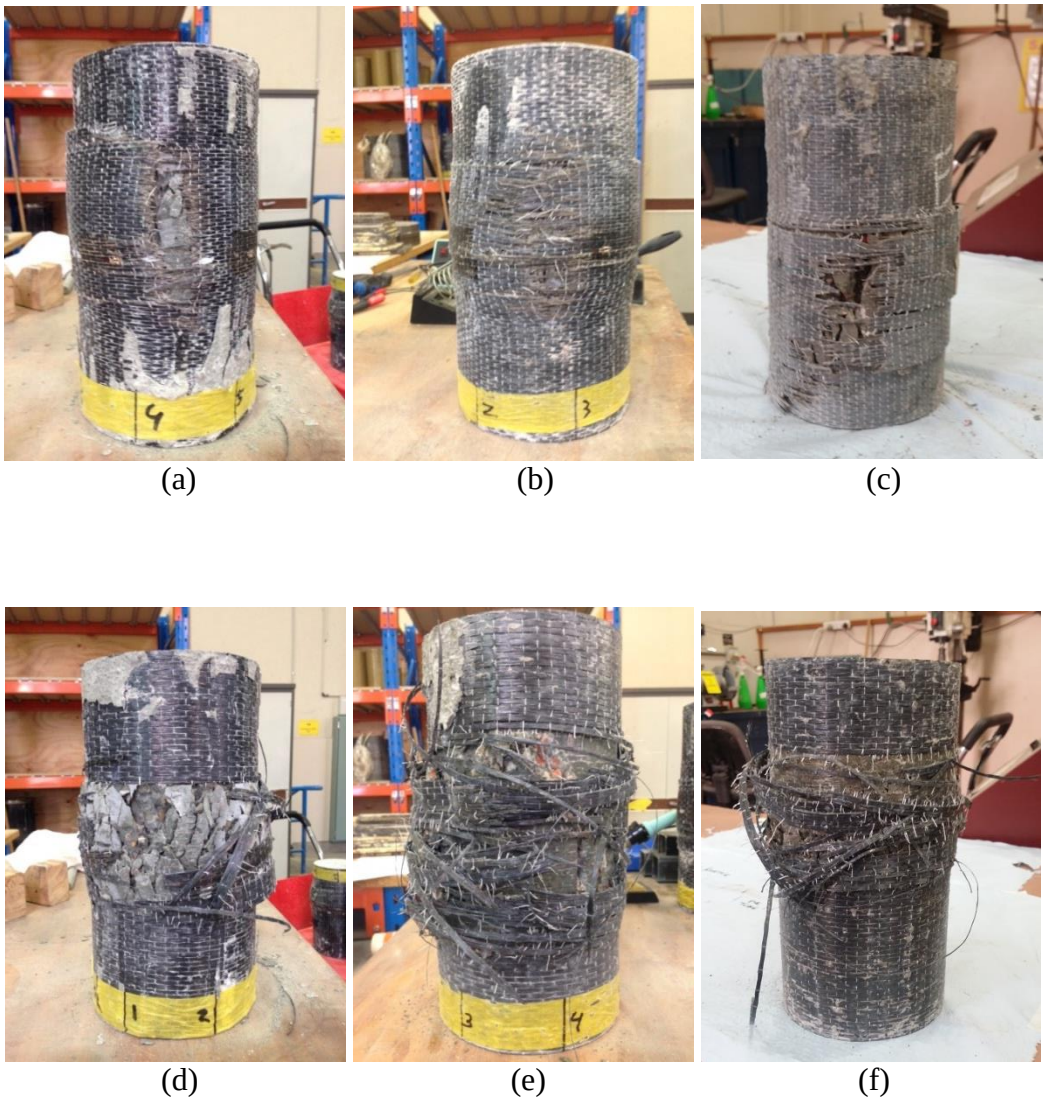

Figure 4. Failure modes of high-strength CFFTs series: a) H-C-B-0; b) H-C-B-50; c) H-C-B-100; d) H-C-C-0; e) H-C-C-50; f) H-C-C-100

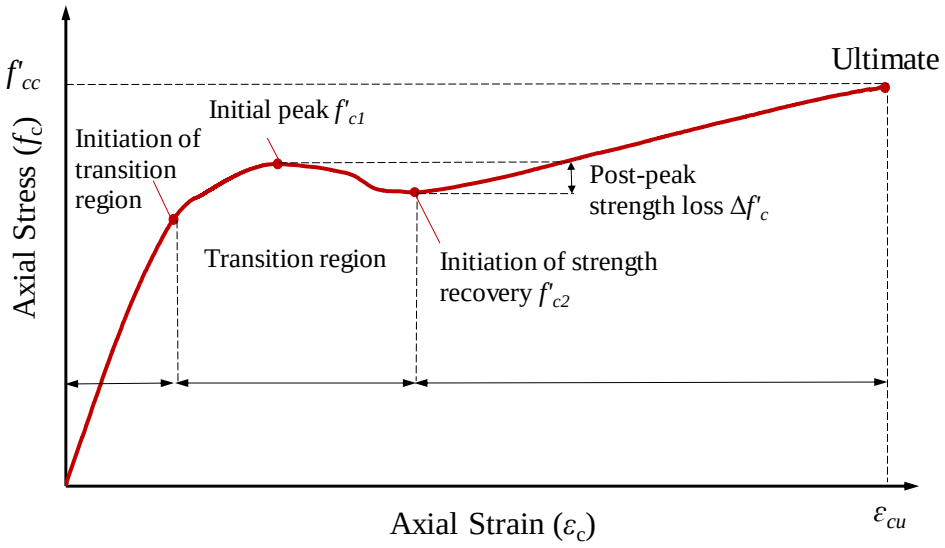

Figure 5. Illustration of critical points and regions on axial stress-strain curve

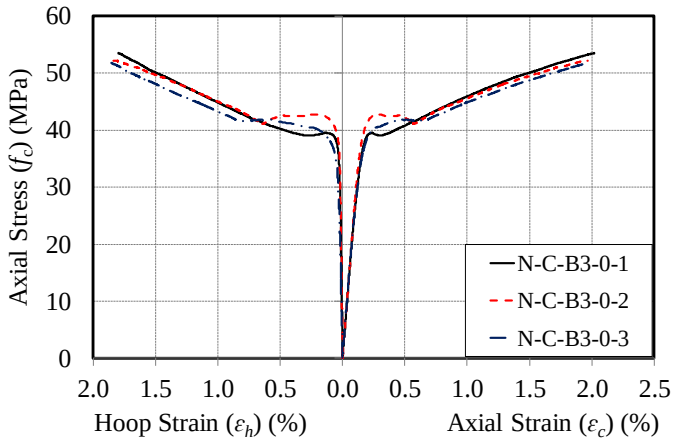

(a)

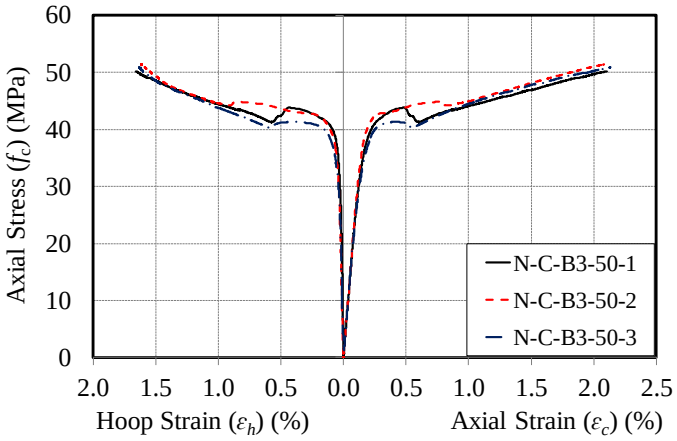

(b)

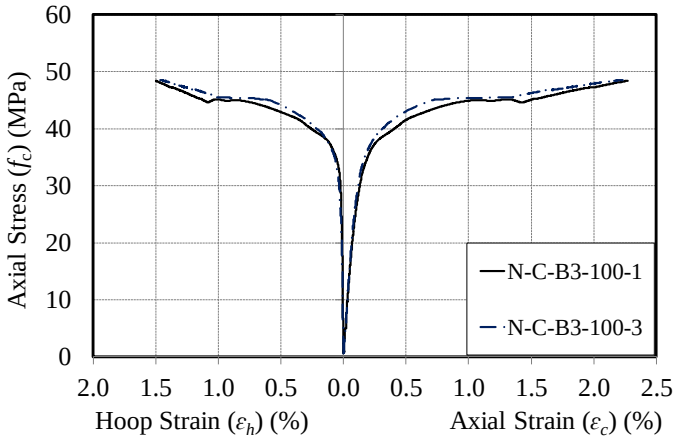

(c)

Figure 6. Axial stress-strain behavior of N-C-B3 series of CFFTs: a) N-C-B3-0; b) N-C-B3-50; c) N-C-B3-100

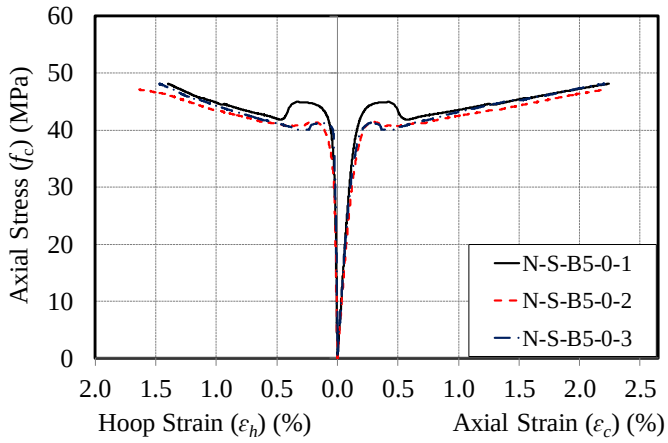

(a)

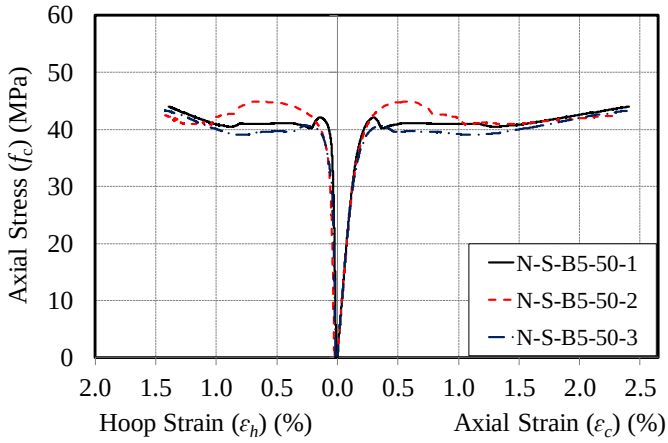

(b)

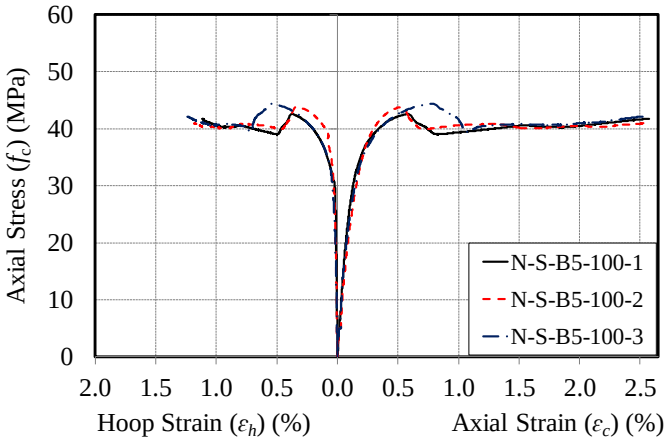

(c)

Figure 7. Axial stress-strain behavior of N-S-B5 series of CFFTs: a) N-S-B5-0; b) N-C-B5-50; c) N-S-B5-100

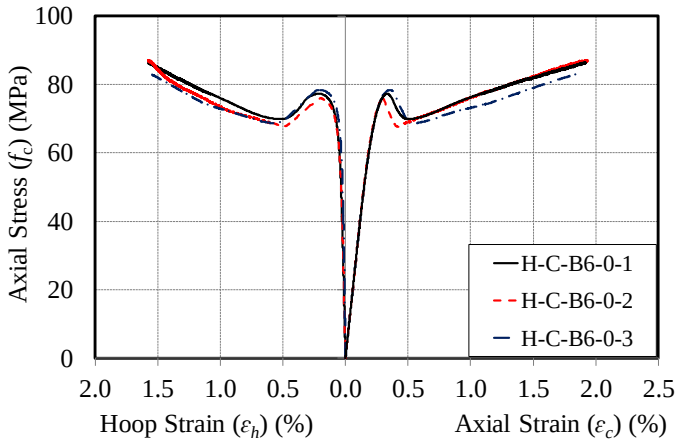

(a)

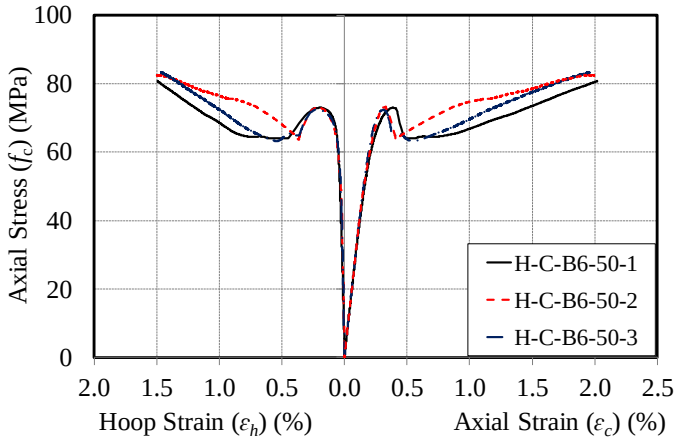

(b)

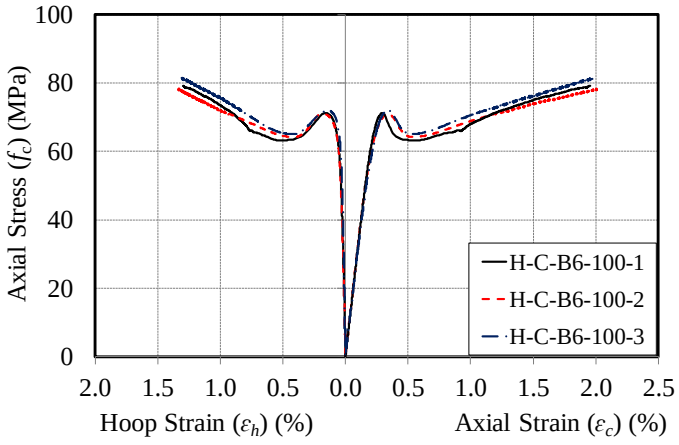

(c)

Figure 8. Axial stress-strain behavior of H-C-B6 series of CFFTs: a) H-C-B6-0; b) H-C-B6-50; c) H-C-B6-100

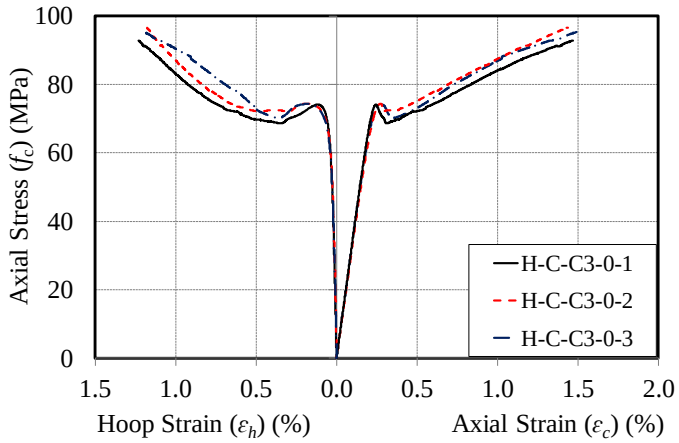

(a)

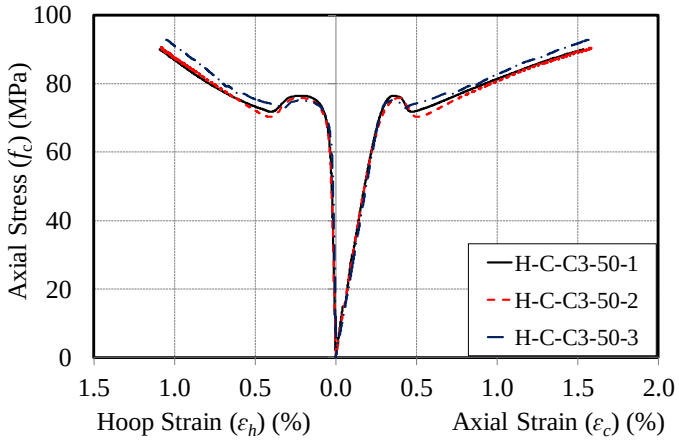

(b)

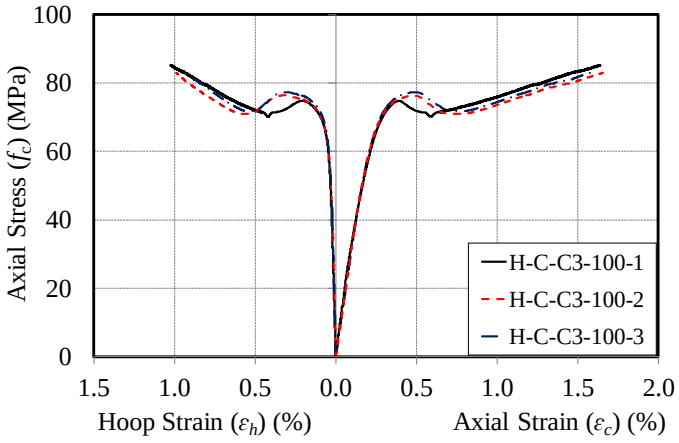

(c)

Figure 9. Axial stress-strain behavior of H-C-C3 series of CFFTs: a) H-C-C3-0; b) H-C-C3-50; c) H-C-C3-100

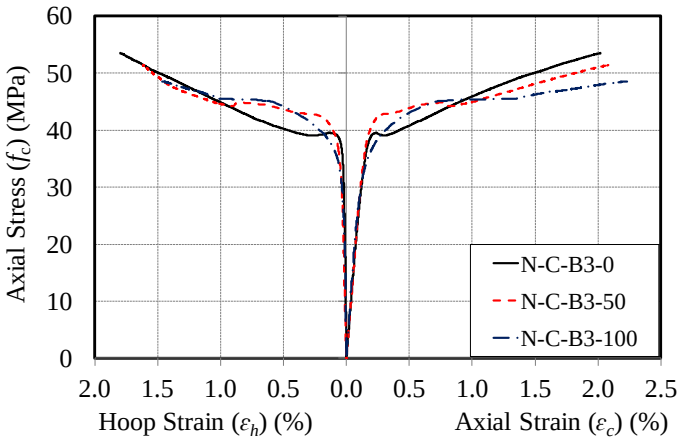
Axial Stress (f_c) (MPa)
60
50
40
30
20
10
0
2.0 1.5 1.0 0.5 0.0 0.5 1.0 1.5 2.0 2.5
Hoop Strain (ε_h) (%)
Axial Strain (ε_c) (%)
N-C-B3-0
N-C-B3-50
N-C-B3-100

(a)

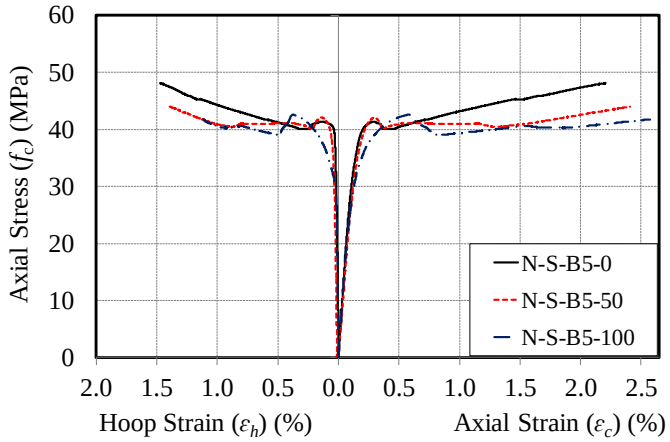
Axial Stress (f_c) (MPa)
60
50
40
30
20
10
0
2.0 1.5 1.0 0.5 0.0 0.5 1.0 1.5 2.0 2.5
Hoop Strain (ε_h) (%)
Axial Strain (ε_c) (%)
N-S-B5-0
N-S-B5-50
N-S-B5-100

(b)

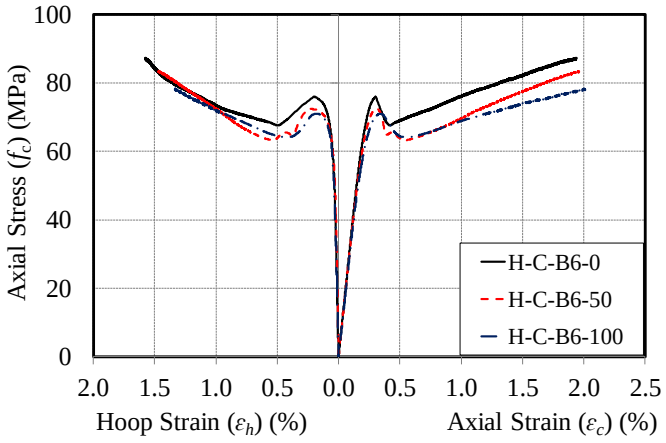
Axial Stress (f_c) (MPa)
100
80
60
40
20
0
2.0 1.5 1.0 0.5 0.0 0.5 1.0 1.5 2.0 2.5
Hoop Strain (ε_h) (%)
Axial Strain (ε_c) (%)
H-C-B6-0
H-C-B6-50
H-C-B6-100

(c)

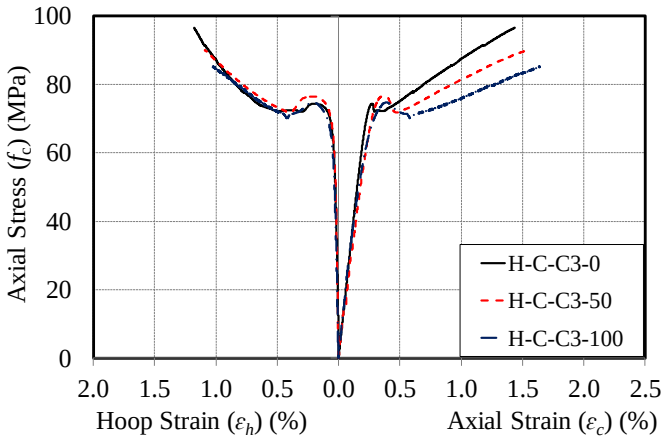

(d)

Figure 10. Influence of RCA replacement ratio on compressive behavior of CFFTs: a) N-C-B3; b) N-S-B5; c) H-C-B6; d) H-C-C3

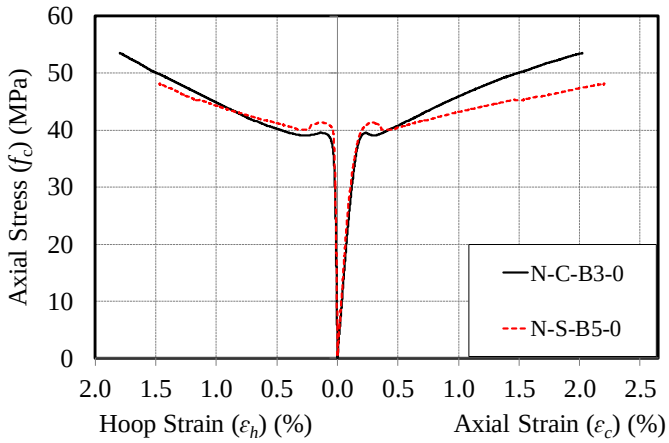

(a)

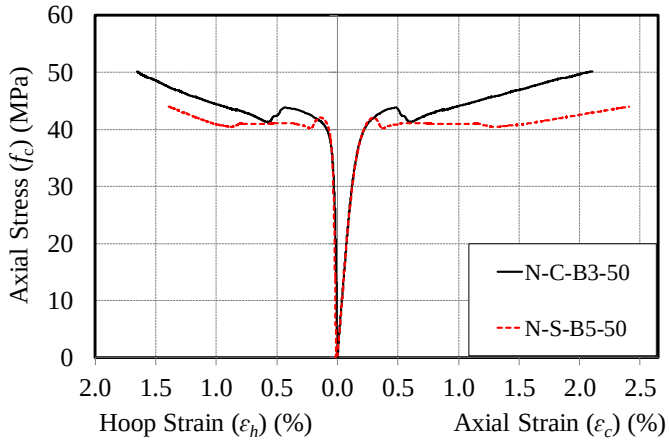

(b)

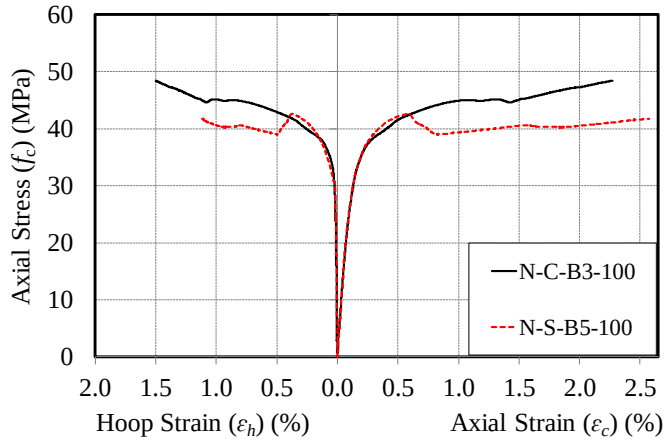

(c)

Figure 11. Influence of specimen cross sectional shape on compressive behavior of CFFTs: a) *RCA* = 0%; b) *RCA* = 50%; c) *RCA* = 100%

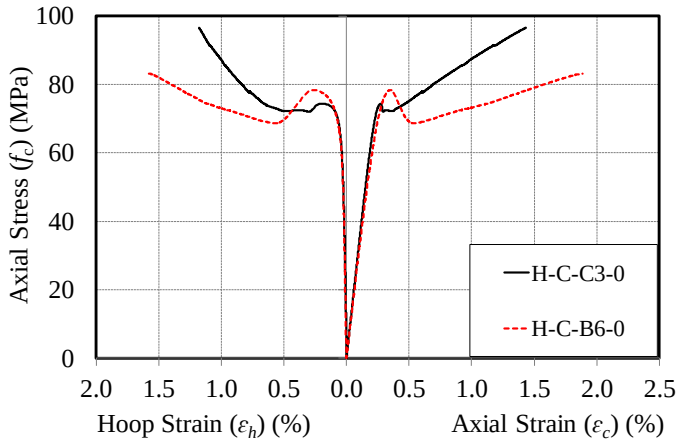

(a)

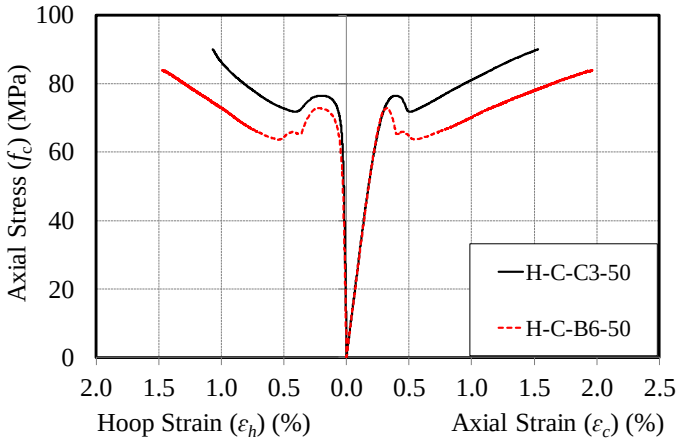

(b)

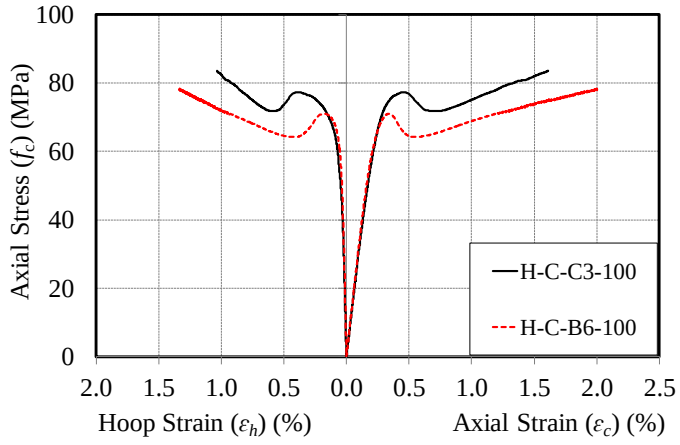

(c)

Figure 12. Influence of FRP type on compressive behavior of CFFTs: a) *RCA* = 0%; b) *RCA* = 50%; c) *RCA* = 100%

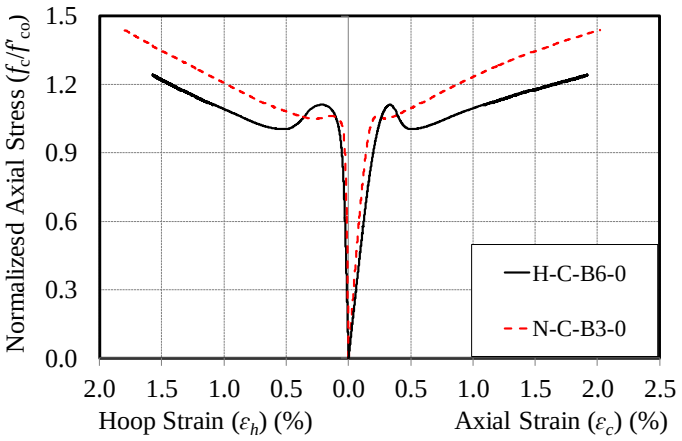

(a)

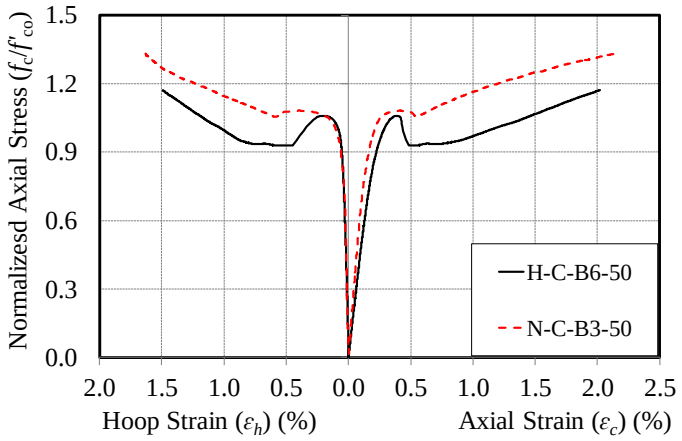

(b)

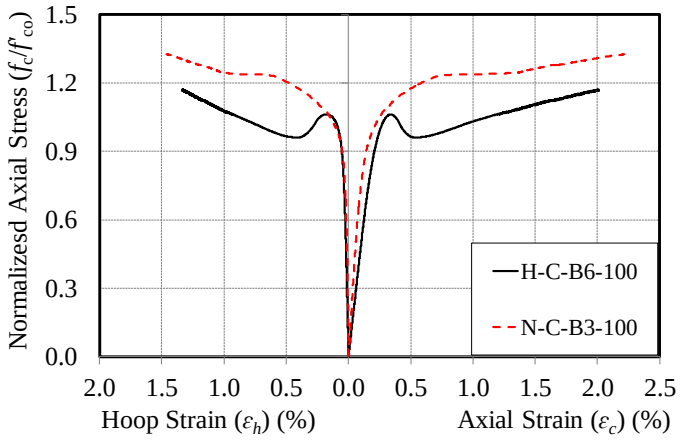

(c)

Figure 13. Influence of concrete strength on compressive behavior of CFFTs: a) *RCA* = 0%; b) *RCA* = 50%; c) *RCA* = 100%

JOURNAL ARTICLE 5

THIS PAGE HAS BEEN LEFT INTENTIONALLY BLANK

Statement of Authorship

Title of Paper	Behavior of steel fiber-reinforced high-strength concrete-filled FRP tube columns under axial compression
Publication Status	☑ Published ☐ Accepted for Publication ☐ Submitted for Publication ☐ Publication Style
Publication Details	Engineering Structures, 90, 158-171.

Author Contributions

Name of Principal Author (Candidate)	Tianyu Xie		
Contribution to the Paper	Analysis of test results, and preparation of manuscript		
Signature		Date	2/9/2015

Name of Co-Author	Dr Togay Ozbakkaloglu		
Contribution to the Paper	Design of experimental tests, supervision of experimental tests, and review of manuscript		
Signature		Date	2/9/2015

Engineering Structures 90 (2015) 158–171

Contents lists available at ScienceDirect

Engineering Structures

journal homepage: www.elsevier.com/locate/engstruct

Behavior of steel fiber-reinforced high-strength concrete-filled FRP tube columns under axial compression

Tianyu Xie, Togay Ozbakkaloglu *

School of Civil, Environmental and Mining Engineering, University of Adelaide, Australia

ARTICLE INFO

Article history:
Received 7 June 2014
Revised 17 February 2015
Accepted 17 February 2015
Available online 7 March 2015

Keywords:
High-strength concrete (HSC)
Fiber-reinforced polymer (FRP)
Steel fiber-reinforced high-strength concrete (SFRHSC)
Slurry infiltrated fiber concrete (SIFCON)
Confinement
Compressive strength
Stress–strain relationship

ABSTRACT

This paper presents the results of the first-ever experimental study on the axial compressive behavior of steel fiber reinforced high-strength concrete (SFRHSC)-filled FRP tubes. A total of 27 circular unreinforced and steel fiber reinforced high-strength concrete FRP tubes (SFRHSCFFTs) were tested under axial compression. The effects of steel fiber parameters, including fiber shape, fiber aspect ratio and fiber volume fraction were examined. Concrete type was also investigated as a parameter, where two different types of concrete, including a conventional HSC and slurry infiltrated fiber concrete (SIFCON) were considered. The results indicate that both SFRHSCFFTs and SIFCON-filled FRP tubes (SIFCONFFTs) exhibit highly ductile compressive behavior. The results also indicate that the axial stress–strain behavior of CFFTs is influenced by the presence and amount of internal steel fibers, with particularly significant influences noted on the FRP hoop rupture strains and post-peak strength losses. It is found that fiber volume fraction significantly affects the compressive behavior of CFFTs. Concrete type, fiber shape and fiber aspect ratio also have some, but less significant, influence on the behavior of CFFTs. It is observed that the compressive strength and ultimate strain of CFFTs increases with an increase in fiber volume fraction or a decrease in fiber aspect ratio. It is also observed that CFFTs reinforced with hooked end steel fibers exhibit improved compressive behavior compared to the companion CFFTs reinforced with crimped fibers.

1. Introduction

It is now well-understood that the confinement of concrete with fiber-reinforced polymer (FRP) composites can lead to significant improvements in both compressive strength and ductility of the concrete. A comprehensive review of the literature previously reported in Refs. [1–4] illustrated the great number of studies that have been undertaken on the topic to investigate the axial compressive behavior of both FRP-wrapped concrete columns (e.g., [5–12]) and concrete-filled FRP tubes (CFFTs) (e.g., [13–18]).

The superior structural engineering properties of high-strength concrete (HSC) over normal-strength concrete (NSC) makes it an attractive alternative for use in the construction of new composite columns such as CFFTs. A number of studies have recently been reported in the literature on FRP-confined HSCs (e.g., [19–27]), which have been complemented by a comprehensive experimental program that has been underway at the University of Adelaide on the behavior of FRP–HSC composite columns [28–38]. These studies have demonstrated the ability of these composite column systems to exhibit a highly ductile behavior under both concentric and simulated seismic loading conditions. However, as was also demonstrated in some of these studies, due to the inherently brittle nature of HSC, even well-confined columns often exhibit a temporary post-peak axial strength softening behavior, which negatively affects their overall performance [28,29,32,35,37]. These findings indicate that there may be benefits in exploring new composite structural systems that are able to maintain the desirable properties of FRP-confined HSC, while overcoming its identified shortcoming.

It is well understood that the inherently brittle behavior of plain concrete can be improved through the addition of internal steel fibers to the wet concrete mix [39–45]. The behavior of steel fiber reinforced concrete (SFRC) has been widely studied over the past three decades (e.g., [39–60]). These studies have found that the presence of internal steel fibers, which forms bridges across the cracks, is effective in delaying and arresting crack propagations, thereby resulting in improvements in the strength and ductility of concrete [41,43,47–53,55–57,59]. Benefiting from the improved properties of the internal concrete, SFRHSC-filled FRP tubes (SFRHSCFFT) may form an attractive composite system that is capable of addressing the aforementioned shortcoming seen in FRP-confined conventional HSC. However, as revealed by a careful review of the existing literature, no study has been reported to date

* Corresponding author. Tel.: +61 8 8313 6477; fax: +61 8 8313 4359.
E-mail address: togay.ozbakkaloglu@adelaide.edu.au (T. Ozbakkaloglu).

http://dx.doi.org/10.1016/j.engstruct.2015.02.020
0141-0296/

on the behavior of FRP-confined SFRCs under concentric compression. The only existing study on FRP-confined SFRCs examined the behavior of specimens that contained internal steel reinforcing bars under eccentric loading [61].

As the first experimental study reported to date on the axial compressive behavior of SFRHSCFFTs, the study presented in this paper was aimed at examining the influence of key parameters to address the aforementioned research gaps. In addition to the conventional SFRHSCFFTs, SIFCON-filled FRP tubes (SIFCONFFTs) were also studied as part of the experimental program to establish their performance under axial compression first time in the literature. The paper initially provides a summary of the experimental program, including specimen properties and the testing procedure. Following this, the results of the experimental program are presented. Finally, a detailed discussion on the results of the experimental study is provided, where the influence of concrete type, shape of steel fiber, aspect ratio of steel fiber and volume fraction of steel fiber are presented along with other key experimental observations.

2. Test program

2.1. Test specimens

A total of 27 circular CFFTs, including 15 SFRHSCFFTs, 3 HSCFFTs, 3 SIFCONFFTs and 3 unreinforced SIFCONFFTs were manufactured and tested under axial compression. In addition, 27 unconfined control specimens, with the same materials and geometric properties to the CFFTs they were companion to, were tested to establish the mechanical properties of unconfined concretes. The specimens were 152.5 mm in diameter, measured at the concrete core, and 305 mm in height. The test parameters included: type of concrete (i.e., SFRHSC or SIFCON), shape of steel fiber (i.e., hooked end or crimped), volume fraction of steel fibers (i.e., V_f = 0%, 1.5% or 2.5%) and aspect ratio of steel fiber (i.e., A_s = 37, 44 or 67). All the confined specimens were manufactured as CFFTs, with the FRP tubes manufactured using a manual wet lay-up procedure with unidirectional aramid fiber sheets. Details of these specimens are given in Table 1. Three nominally identical specimens were tested for each unique specimen configuration.

2.2. Materials

2.2.1. Concrete

The specimens were manufactured using five different concrete mixtures. Three of these mixes were proportioned as a conventional HSC mix and they consisted of crushed limestone as the coarse aggregate with a nominal maximum size of 10 mm, and silica fume dosed at 11% of the binder content by weight. All of these mixes had a water to cement ratio (w/c) of 0.285, and the only difference among them was the volume fraction of steel fibers (V_f) they contained, as shown in Table 2. The remaining two mixes were designed as SIFCON mixes with or without internal steel fibers. These mixes contained no coarse aggregates and they had a w/c of 0.245 and silica fume added at 20% of the binder content by weight. A polycarboxylic ether polymer based superplasticiser was added to all mixes to attain a workable mix.

In the preparation of the conventional SFRHSC specimens, the steel fibers were added after the addition of the water and superplasticiser to the mix. This approach was adopted to ensure that the unreinforced concrete developed a certain level of workability, after which it was possible to mix steel fibers with concrete under a 'wet' condition. For the SIFCON mixes, cementitious binder and fine aggregates were first blended under a dry condition. Water and superplasticiser were then gradually added into the mix to form cement mortar slurry. The prepared cement mortar slurry

Table 1
Details of FRP confined specimens.

	Concrete type	FRP tube total fiber thickness (mm)	Fiber type[a]	Fiber volume fraction V_f (%)	Fiber aspect ratio A_s (l_f/d_f)	Fiber reinforcing index RI ($V_f \times A_s$)
C-UR-1	HSC1	1.2	–	–	–	–
C-UR-2	HSC1	1.2	–	–	–	–
C-UR-3	HSC1	1.2	–	–	–	–
C-HV1.5A67-1	HSC2	1.2	II	1.5	67	1.01
C-HV1.5A67-2	HSC2	1.2	II	1.5	67	1.01
C-HV1.5A67-3	HSC2	1.2	II	1.5	67	1.01
C-HV2.5A67-1	HSC3	1.2	II	2.5	67	1.68
C-HV2.5A67-2	HSC3	1.2	II	2.5	67	1.68
C-HV2.5A67-3	HSC3	1.2	II	2.5	67	1.68
C-HV1.5A37-1	HSC2	1.2	I	1.5	37	0.56
C-HV1.5A37-2	HSC2	1.2	I	1.5	37	0.56
C-HV1.5A37-3	HSC2	1.2	I	1.5	37	0.56
C-HV2.5A37-1	HSC3	1.2	I	2.5	37	0.93
C-HV2.5A37-2	HSC3	1.2	I	2.5	37	0.93
C-HV2.5A37-3	HSC3	1.2	I	2.5	37	0.93
C-CV1.5A44-1	HSC2	1.2	III	1.5	44	0.66
C-CV1.5A44-2	HSC2	1.2	III	1.5	44	0.66
C-CV1.5A44-3	HSC2	1.2	III	1.5	44	0.66
C-CV2.5A44-1	HSC3	1.2	III	2.5	44	1.10
C-CV2.5A44-2	HSC3	1.2	III	2.5	44	1.10
C-CV2.5A44-3	HSC3	1.2	III	2.5	44	1.10
C-UR-SIF-1	SIFCON1	1.2	–	–	–	–
C-UR-SIF-2	SIFCON1	1.2	–	–	–	–
C-UR-SIF-3	SIFCON1	1.2	–	–	–	–
C-HV5A37-SIF-1	SIFCON2	1.2	III	5	37	1.85
C-HV5A37-SIF-2	SIFCON2	1.2	III	5	37	1.85
C-HV5A37-SIF-3	SIFCON2	1.2	III	5	37	1.85

[a] Refer to Table 3.

Table 2
Mix proportions of concrete.

	Conventional HSC			SIFCON	
Label	HSC1	HSC2	HSC3	SIFCON1	SIFCON2
Fiber volume fraction V_f (%)	0	1.5	2.5	0	5
Cement (kg/m^3)	500	500	500	931	931
Silica fume (kg/m^3)	62	62	62	233	233
Sand (kg/m^3)	702	702	702	1024	634
Limestone (kg/m^3)	1052	935	857	–	–
Water (kg/m^3)	144	144	144	255	255
Superplasticiser (kg/m^3)	20	20	20	37	37
Fiber (kg/m^3)	–	117	195	–	390
W/C ratio (%)	0.285	0.285	0.285	0.245	0.245

was then poured in the molds or FRP tubes one layer at a time, and steel fibers were placed at the top of each layer. Gentle external vibration was used throughout the pouring processes of the SIFCON mixes to ensure proper blending of the fibers and concrete.

As shown in Table 2, in the specimens that contained internal steel fibers, the fibers were added to the mix at a specified fiber volume fraction (V_f) by replacing part of the coarse aggregate in conventional SFRHSC and sand in SIFCON mixes. The test specimens were cast of nine separate batches, where each individual batch adopted one of the five mix proportions shown in Table 2.

2.2.2. Steel fibers

Three different types of steel fibers were selected, whose manufacturer supplied properties are summarized in Table 3. Fiber types I and II, shown in Fig. 2(a) and (b), were both hooked end type, but they had different fiber aspect ratios of 37 and 67, respectively. Fiber III, shown in Fig. 2(c) was crimped type and had an aspect ratio of 44. Steel fibers were added at volume fractions (V_f) of 0%, 1.5% or 2.5% in SFRHSC mixes, and 0% or 5% in SIFCON mixes. The reinforcing index (RI) of fibers was calculated by Eq. (1) for each specimen, and these values are reported in Table 1.

$$RI = (V_f \times A_s) \quad (1)$$

In Eq. (1), V_f is the fiber volume fraction (i.e., volume of fibers per unit volume of concrete), and A_s is the fiber aspect ratio ($A_s = l_f/d_f$, where l_f is the fiber length and d_f is the equivalent fiber diameter). The reinforcing index (RI) is often used to express the cumulative influence of steel fibers on the mechanical properties of SFRCs. It has been shown that the post-peak compressive stress–strain behavior of unconfined SFRC is significantly influenced by RI, with a reduction in the second branch slope resulting from an increase in RI [40,41,46,49].

Table 3
Material properties of steel fibers.

Type	Length l (mm)	Diameter d_f (mm)	Aspect ratio (l/d_f)	Tensile strength (MPa)	Shape
I	31	0.85	37	1200 ± 50	Hooked end
II	60	0.90	67	1050 ± 50	Hooked end
III	40	0.90	44	>900	Crimped

2.2.3. FRP tubes

The FRP tubes of all CFFT specimens were manufactured using a manual wet lay-up process by wrapping epoxy resin impregnated fiber sheets around precision-cut high-density Styrofoam templates in the hoop direction. The epoxy resin was allowed to cure at room temperature for at least 24 h before the FRP tubes were removed from their molds. The FRP tubes were prepared by using four layers of aramid FRP with a 0.3 mm ply thickness to achieve sufficient amount of confinement that would lead to axial stress–strain curves with ascending second branches. CFFTs were manufactured using a single length of FRP sheet wrapped continuously in the hoop direction, creating an overlap length of 150 mm that was supplied to prevent premature debonding failure. The specimens were also strengthened with a 30-mm wide single layer FRP strip applied in the hoop direction at both ends to ensure their failure occurred near the mid-height region, where the hoop strain gauges were placed. The material properties of the FRP sheets were obtained through flat coupon tests performed in accordance with ASTM standard D3039M-08 [62]. Table 4 provides the manufacturer supplied properties of the unidirectional fiber sheets and epoxy resin used in the manufacture of the FRP tubes together with the properties of the FRP composite obtained from flat coupon tests and calculated based on nominal fiber thicknesses.

2.2.4. Specimen designation

The specimens in Tables 1 and 5–8 were labeled as follows: Each label started with letter C and letters UC for confined and unconfined specimens, respectively, which was followed by a dash. In specimens that contained no internal steel fibers, the letters 'UR' were used after the dash to denote 'unreinforced'. In specimens that contained steel fibers, the dash was followed by a subsequent letter (i.e., either H (for hooked end) or C (for crimped)) that was used to indicate the shape of the steel fiber. The following letters V and A were used to represent the test parameters, namely, the steel fiber volume fraction (in percent) and steel fiber aspect ratio, respectively. Each of these letters was followed by a number that was used to specify the value of the given parameter. In specimens manufactured with SIFCON mixes, the abbreviation 'SIF' was added to the end of the specimen designation. Finally, the last number in the specimen designation (i.e., 1, 2 or 3) was used to distinguish three nominally identical specimens. For example, C-CV2.5A44-1 is the first of the three identical SFRHSCFFT specimens that were reinforced by crimped steel fibers with at an aspect ratio of 44, which were added to the mix at a fiber volume fraction of 2.5%.

2.2.5. Instrumentation and testing

As shown in Fig. 1, four linear variable displacement transducers (LVDT) were mounted at the corners between the loading

Table 4
Material properties of fiber, FRP composite and epoxy resin.

Type	Nominal fiber thickness t_f (mm/ply)	Fiber/FRP properties					
		Provided by manufacturer			Obtained from coupon tests[a]		
		Ultimate tensile stress f_f (MPa)	Ultimate tensile strain ε_f (%)	Elastic modulus E_f (GPa)	Ultimate tensile stress f_{frp} (MPa)	Ultimate tensile strain ε_{frp} (%)	Elastic modulus E_{frp} (GPa)
Aramid fiber	0.3	2600	2.20	118.2	2390	1.86	128.5

[a] Calculated based on nominal thickness of fibers.

Table 5
Compression test results of unconfined specimens.

Specimens	f'_{co} (MPa)	Avg. f'_{co} (MPa)	ε_{co}[a] (%)	Avg. ε_{co}[a] (%)	ε_{co}[b] (%)	Avg. ε_{co}[b] (%)
UC-UR-1	123.5		0.27		–	
UC-UR-2	127.0	125.4	0.33	0.30	–	–
UC-UR-3	125.7		0.30		–	
UC-HV1.5A67-1	131.6		0.34		0.28	
UC-HV1.5A67-2	124.6	129.6	0.29	0.32	0.23	0.26
UC-HV1.5A67-3	132.7		0.33		0.27	
UC-HV2.5A67-1	123.9		0.36		0.30	
UC-HV2.5A67-2	131.4	126.5	0.35	0.34	0.27	0.27
UC-HV2.5A67-3	124.2		0.34		0.25	
UC-HV1.5A37-1	124.0		0.32		0.30	
UC-HV1.5A37-2	127.1	125.8	0.35	0.32	0.34	0.31
UC-HV1.5A37-3	126.4		0.30		0.29	
UC-HV2.5A37-1	122.5		0.29		0.27	
UC-HV2.5A37-2	126.4	124.6	0.30	0.30	0.27	0.27
UC-HV2.5A37-3	124.8		0.31		0.26	
UC-CV1.5A44-1	116.1		0.36		0.28	
UC-CV1.5A44-2	115.7	116.8	0.33	0.34	0.25	0.27
UC-CV1.5A44-3	118.6		0.35		0.27	
UC-CV2.5A44-1	127.1		0.33		0.27	
UC-CV2.5A44-2	125.9	125.3	0.31	0.33	0.28	0.27
UC-CV2.5A44-3	122.8		0.36		0.27	
UC-UR-SIF-1	110.1		0.46		0.43	
UC-UR-SIF-2	112.6	111.3	0.48	0.47	0.43	0.43
UC-UR-SIF-3[c]	93.3		0.35		0.31	
UC-HV5A37-SIF-1	119.4		0.58		0.47	
UC-HV5A37-SIF-2	114.0	116.7	0.56	0.57	0.46	0.46
UC-HV5A37-SIF-3	116.6		0.57		0.46	

[a] Axial strain calculated by averaging four full-height LVDTs recorded data.
[b] Axial strain value recorded by strain gauges installed on longitudinal direction.
[c] Specimen failed prematurely. Excluded in the calculation of average values.

Table 6
Axial compressive stresses of confined specimens.

Specimens	Avg. f'_{co} (MPa)	f'_{cc} (MPa)	Avg. f'_{cc} (MPa)	f'_{c1} (MPa)	f'_{c2} (MPa)	$\Delta f'_c$ (MPa)	Avg. $\Delta f'_c$ (MPa)	f'_{cc}/f'_{co}	Avg. f'_{cc}/f'_{co}
C-UR-1		174.0		136.0	116.4	19.6		1.39	
C-UR-2[a]	125.4	160.6	177.3	133.4	118.6	14.8	19.2	1.28	1.41
C-UR-3		180.6		135.2	116.5	18.7		1.44	
C-HV1.5A67-1		179.8		142.0	139.8	2.2		1.39	
C-HV1.5A67-2	129.6	171.3	173.6	152.4	145.4	7.0	7.43	1.32	1.34
C-HV1.5A67-3		169.7		150.5	137.4	13.1		1.31	
C-HV2.5A67-1		191.6		134.0	134.0	0.0		1.51	
C-HV2.5A67-2	126.5	204.7	195.8	136.1	135.0	1.1	0.53	1.62	1.55
C-HV2.5A67-3		191.2		139.6	139.1	0.5		1.51	
C-HV1.5A37-1		191.8		128.1	127.7	0.4		1.52	
C-HV1.5A37-2	125.8	188.1	188.4	146.3	143.2	3.1	1.40	1.49	1.50
C-HV1.5A37-3		185.2		146.0	145.3	0.7		1.47	
C-HV2.5A37-1		199.9		137.2	136.9	0.3		1.60	
C-HV2.5A37-2	124.6	195.3	199.8	138.4	138.4	0.0	0.10	1.57	1.60
C-HV2.5A37-3		204.1		133.9	133.9	0.0		1.64	
C-CV1.5A44-1		171.1		130.0	120.4	9.6		1.46	
C-CV1.5A44-2	116.8	175.0	169.6	132.7	129.0	3.7	5.93	1.50	1.45
C-CV1.5A44-3		162.8		135.1	130.6	4.5		1.39	
C-CV2.5A44-1		201.9		129.8	129.8	0.0		1.61	
C-CV2.5A44-2[b]	125.3	168.8	201.9	131.8	131.2	0.6	0.00	1.35	1.61
C-CV2.5A44-3[b]		165.0		137.8	136.2	1.6		1.32	
C-UR-SIF-1		144.7		110.0	89.5	20.5		1.30	
C-UR-SIF-2	111.3	139.3	147.9	113.5	96.4	17.1	15.5	1.25	1.33
C-UR-SIF-3		159.6		115.4	106.6	8.8		1.43	
C-HV5A37-SIF-1		195.3		132.8	132.8	0.0		1.67	
C-HV5A37-SIF-2	116.7	185.1	192.2	140.0	139.9	0.1	0.76	1.59	1.65
C-HV5A37-SIF-3		196.3		132.8	130.6	2.2		1.68	

[a] Premature failure due to FRP debonding. Excluded in the calculation of average values.
[b] Premature failure due to excessive eccentricity during loading. Excluded in the calculation of average values.

Table 7
Axial strains of confined specimens.

Specimens	ε_{cu} (%)		Avg. ε_{cu} (%)		MLVDT/FLVDT
	FLVDTs	MLVDTs	FLVDTs	MLVDTs	
C-UR-1	2.07	1.30			
C-UR-2[a]	1.68	1.15	2.12	1.36	0.64
C-UR-3	2.16	1.42			
C-HV1.5A67-1	1.91	1.77			
C-HV1.5A67-2	1.78	1.52	1.79	1.47	0.81
C-HV1.5A67-3	1.68	1.11			
C-HV2.5A67-1	2.00	1.77			
C-HV2.5A67-2	2.50	2.16	2.15	1.85	0.86
C-HV2.5A67-3	1.95	1.62			
C-HV1.5A37-1	2.05	1.81			
C-HV1.5A37-2	1.82	1.67	1.94	1.73	0.89
C-HV1.5A37-3	1.95	1.71			
C-HV2.5A37-1	2.65	2.27			
C-HV2.5A37-2	2.16	1.83	2.37	1.98	0.83
C-HV2.5A37-3	2.31	1.84			
C-CV1.5A44-1	1.77	1.63			
C-CV1.5A44-2	1.90	1.41	1.77	1.63	0.84
C-CV1.5A44-3	1.64	1.39			
C-CV2.5A44-1	2.43	2.10			
C-CV2.5A44-2[b]	1.75	1.29	2.43	2.10	0.86
C-CV2.5A44-3[b]	1.68	1.32			
C-UR-SIF-1	2.32	1.23			
C-UR-SIF-2	2.31	1.47	2.43	1.44	0.59
C-UR-SIF-3	2.67	1.61			
C-HV5A37-SIF-1	2.58	1.95			
C-HV5A37-SIF-2	2.55	1.96	2.49	2.05	0.83
C-HV5A37-SIF-3	2.34	2.24			

[a] Premature failure due to FRP debonding. Excluded in the calculation of average values.
[b] Premature failure due to excessive eccentricity during loading. Excluded in the calculation of average values.

Table 8
FRP hoop rupture strains of confined specimens.

Specimens	$\varepsilon_{h,rup}$ (%)	Avg. $\varepsilon_{h,rup}$ (%)	$k_{\varepsilon,exp}$	Avg. $k_{\varepsilon,exp}$	Avg. $k_{\varepsilon,theo}$
C-UR-1	0.96		0.44		
C-UR-2[a]	0.91	1.02	0.41	0.46	0.52
C-UR-3	1.07		0.49		
C-HV1.5A67-1	1.23		0.56		
C-HV1.5A67-2	1.19	1.19	0.54	0.54	0.51
C-HV1.5A67-3	1.14		0.52		
C-HV2.5A67-1	1.37		0.62		
C-HV2.5A67-2	1.68	1.39	0.76	0.63	0.52
C-HV2.5A67-3	1.11		0.50		
C-HV1.5A37-1	1.40		0.64		
C-HV1.5A37-2	1.42	1.34	0.65	0.61	0.52
C-HV1.5A37-3	1.20		0.55		
C-HV2.5A37-1	1.75		0.80		
C-HV2.5A37-2	1.49	1.70	0.68	0.77	0.52
C-HV2.5A37-3	1.86		0.85		
C-CV1.5A44-1	1.11		0.50		
C-CV1.5A44-2	1.16	1.09	0.53	0.50	0.54
C-CV1.5A44-3	1.00		0.45		
C-CV2.5A44-1	1.47		0.67		
C-CV2.5A44-2[b]	1.01	1.47	0.46	0.67	0.52
C-CV2.5A44-3[b]	1.28		0.58		
C-UR-SIF-1	1.22		0.55		
C-UR-SIF-2	1.13	1.23	0.51	0.56	0.56
C-UR-SIF-3	1.35		0.61		
C-HV5A37-SIF-1	1.17		0.53		
C-HV5A37-SIF-2	1.42	1.33	0.65	0.60	0.54
C-HV5A37-SIF-3	1.40		0.64		

[a] Premature failure due to FRP debonding. Excluded in the calculation of average values.
[b] Premature failure due to excessive eccentricity during loading. Excluded in the calculation of average values.

and supporting steel plates of the compression test machine to measure the axial deformations of the specimens. The average axial strains along the height of the specimens were calculated by using the recorded deformations. Additional four LVDTs were placed at the mid-height at a gauge length of 175 mm at 90° spacing along the circumference of specimens to measure the axial deformation of the middle portion of the specimens. Furthermore, the specimens were instrumented at the mid-height with two unidirectional strain gauges to measure axial strains, which were used to validate LVDT measurements at the early stages of loading. Hoop strains recorded on FRP tubes were obtained from 9 unidirectional strain gauges with a 5-mm gauge length that were spaced equally around the perimeter at the mid-height of the specimen outside the overlap region.

The specimens were tested under axial compression using a 5000-kN capacity universal testing machine. The loading was initially applied with load control at 3 kN per second, whereas displacement control was used at approximately 0.003 mm per second beyond the initial softening until specimen failure. Prior to testing, all specimens were ground at both ends to ensure uniform distribution of the applied pressure, and the load was applied directly to the core of concrete through 150-mm diameter precision cut high-strength steel discs placed at both ends of the specimen.

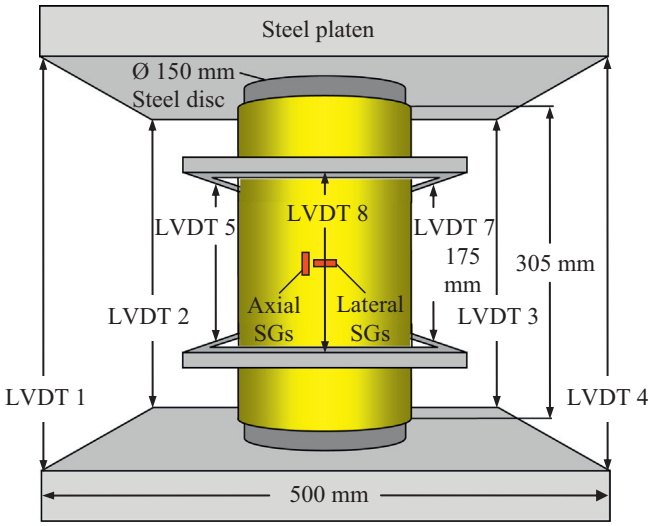

Fig. 1. Test setup and instrumentation.

3. Test results and discussion

3.1. Unconfined specimens

Table 5 presents the compressive strengths (f'_{co}) and the corresponding axial strains (ε_{co}) of the unconfined specimens. As is evident from the results shown in the table, the addition of steel fibers often resulted in a slight increase in the compressive strength. The axial strains at peak (ε_{co}) reported in Table 5 were determined using two different measurement methods (i.e., LVDTs and axial strain gauges). As evident from the table, the axial strains (ε_{co}) obtained from the LVDTs installed along the full-height of the specimens are slightly higher than those recorded by the strain gauges placed at specimen mid-height. The results in Table 5 also indicate that the presence of steel fibers resulted in

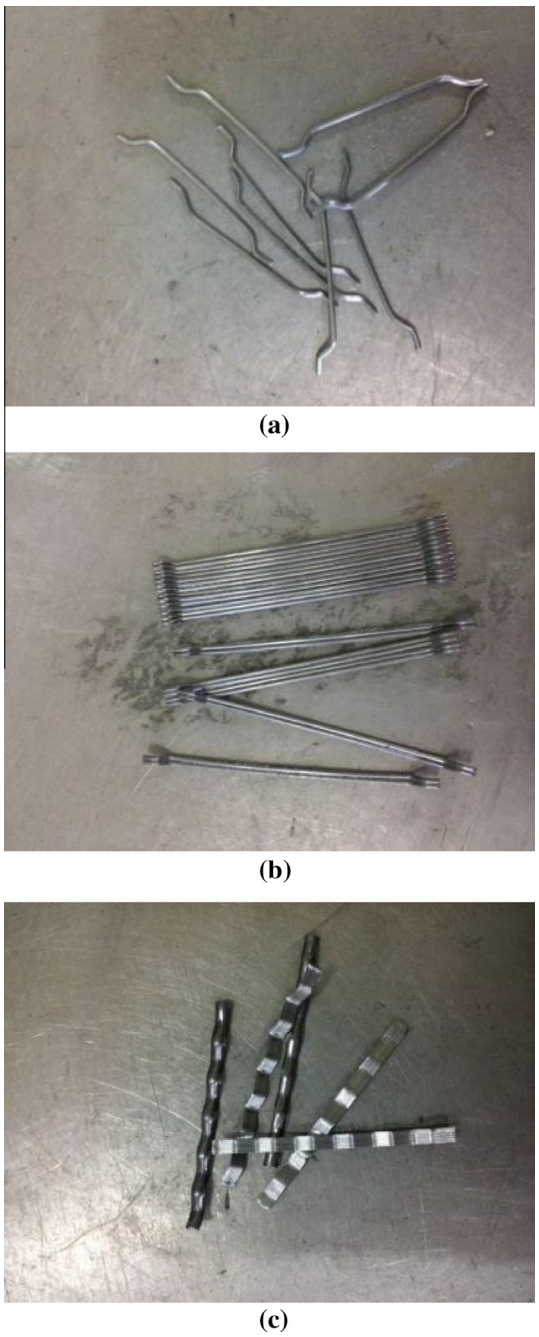

Fig. 2. Illustration of steel fibers: (a) steel fiber type I (hooked end, A_s = 37); (b) steel fiber type II (hooked end, A_s = 67); (c) steel fiber type III (crimped, A_s = 44).

an increase in the axial strain at peak (ε_{co}). This observation accords with those reported in previous studies on unconfined SFRCs, where it was found that the addition of steel fibers led to an increase in peak axial strain of SFRCs [40,41,53].

3.2. Confined specimens

3.2.1. Failure mode

The typical failure modes of test specimens with and without internal steel fibers are presented in Fig. 3(a) and (b) & Fig. 4(a)–(g), respectively. The observed failure mode of all the specimens was rupture of the FRP jacket concomitant with a sudden loss of applied load, except for Specimen C-UR-2 that experienced a premature FRP debonding failure as marked in Table 6. As can be seen in these figures, the rupture of FRP jackets occurred at the mid-height region of the specimens for all cases. Fig. 3(a) and (b) illustrates that the failure of the unreinforced HSCFFT specimens resulted from formation of a few major macro-cracks in the concrete. On the other hand, as shown in Fig. 4(a)–(g), smaller crack formations were observed in the concretes of SFRHSCFFT and SIFCONFFT specimens. These observed differences in the failure modes suggest that the cracking mechanism of the core concrete was influenced by the presence of steel fibers, which is discussed in detail later in the paper.

3.2.2. Axial stresses and strains

Fig. 5(a) and (b) illustrates the different stages typically observed on axial stress–strain curves of the specimens of the present study with and without post-peak strain softening regions, respectively. The notation and definitions introduced in this figure are used consistently throughout the discussion presented in this paper. The summary of the key experimental results are shown in Tables 6 and 7. Table 6 presents the recorded axial stresses, which include: the compressive strength (f'_{cc}), initial peak stress (f'_{c1}) that marks the point of transition from the initial ascending branch to the softening region of the second branch (Fig. 5(a)), stress at plateau formation (f'_{c2}) that marks the point of transition from softening to hardening region on the second branch of the stress–strain curve (Fig. 5(a)), and strength enhancement ratio (f'_{cc}/f'_{co}). Table 6 also shows the magnitude of the post-peak strength loss ($\Delta f'_c$), which were calculated as the difference between the values of f'_{c1} and f'_{c2}.

Table 7 shows the recorded ultimate axial strains (ε_{cu}) of the specimens. The ultimate axial strains (ε_{cu}) reported in Table 7 were obtained at specimen failure either from a set of four full-height LVDTs that measured the displacements along the entire height of the specimen (referred to as FLVDTs in Table 7) or a set of four cage LVDTs that were used to measure the displacements along the mid-height region of the specimen (referred to as MLVDTs in Table 7). The comparisons of the strains obtained from these two measurement methods are also presented in the same table as the ratio of MLVDT/FLVDT. It can be seen from Table 7 that the MLVDT strains were consistently lower than the FLVDT strain. A similar observation was reported in a number of recent studies, where the differences in strains were explained by the cracking behavior of the concrete and it was shown how the increased brittleness of concrete resulted in lower MLVDT/FLVDT ratios [1,37]. It is also evident from Table 7 that the CFFTs with inner steel fibers had higher MLVDT/FLVDT ratios than those of the companion unreinforced CFFTs. Following from the findings of the aforementioned studies, this observation indicates that the presence of inner steel fibers resulted in changes in the crack formations in HSC leading to more evenly distributed cracks rather than a few major cracks typically seen in unreinforced HSC with strength over 100 MPa. In the following sections, the strains obtained from full-height LVDTs were used on the discussions on ultimate axial strains (ε_{cu}), as it was believed that they represented the overall specimen behavior more accurately.

The results reported in Tables 6 and 7 allow a number of important observations be made on the ultimate conditions of the specimens. Firstly, the results indicate that the compressive strength (f'_{cc}) and ultimate strains (ε_{cu}) of the specimens generally increased with an increase in steel fiber volume fraction (V_f) and decreased slightly with an increase in steel fiber aspect ratio (A_s). The results also indicate that, for a given fiber aspect ratio (i.e., A_s = 37 or 44) and fiber volume fraction (i.e., V_f = 1.5% or 2.5%), specimens with hooked end fibers exhibited higher compressive strengths (f'_{cc}) and ultimate axial strains (ε_{cu}) compared to those of the companion specimens with crimped fibers. It is also evident from the results given in Tables 6 and 7 that the unreinforced HSCFFTs exhibited slightly higher compressive strength enhancement ratios

Fig. 3. Failure modes of unreinforced CFFTs: (a) C-UR series; (b) C-UR-SIF series.

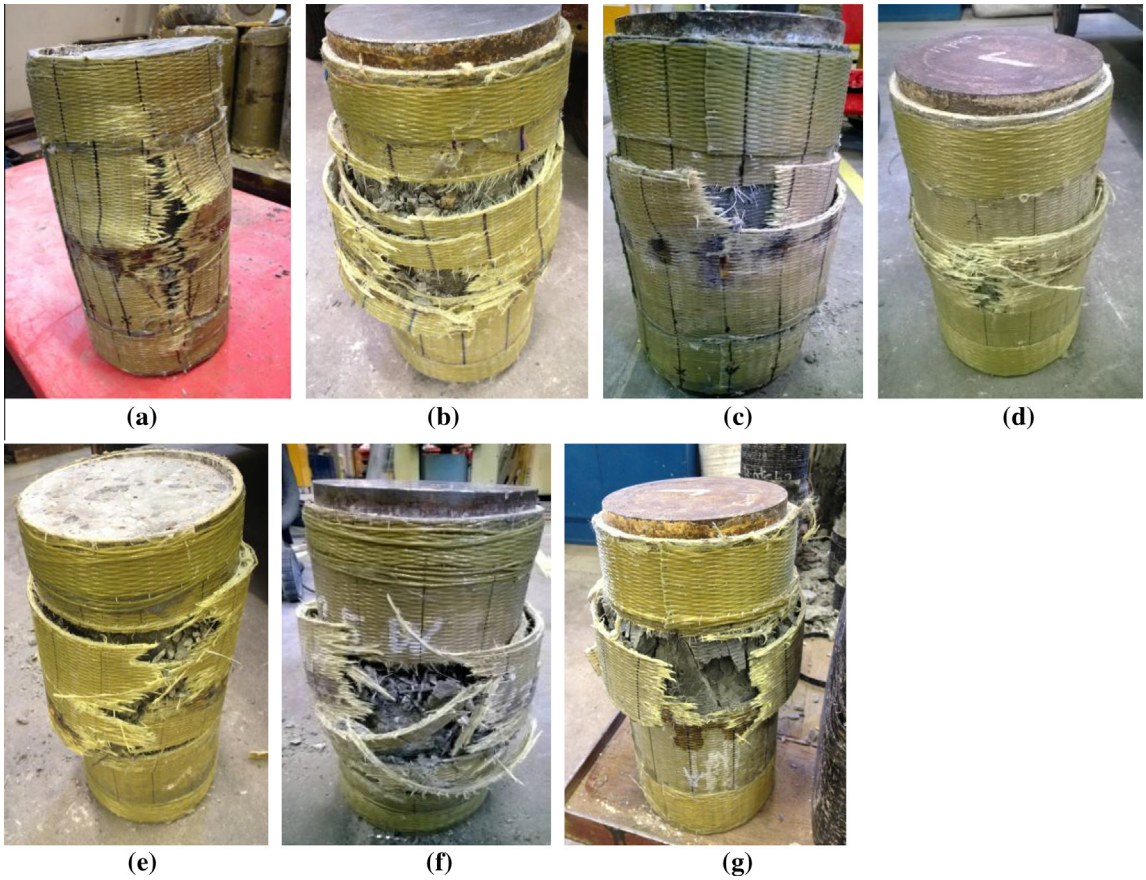

Fig. 4. Failure modes of fiber reinforced CFFTs: (a) C-HV1.5A67 series; (b) C-HV2.5A67 series; (c) C-HV1.5A37 series; (d) C-HV2.5A37 series; (e) C-CV1.5A44 series; (f) C-CV2.5A44 series; (g) C-HV5A37-SIF series.

(f'_{cc}/f'_{co}) than those of the companion unreinforced SIFCONCFFTs. On the other hand, the specimens in the latter group developed significantly higher ultimate axial strains (ε_{cu}) compared to those of the specimens in the former group. The influence of the key parameters on the stress–strain behavior of the specimens is discussed in detail later in the paper.

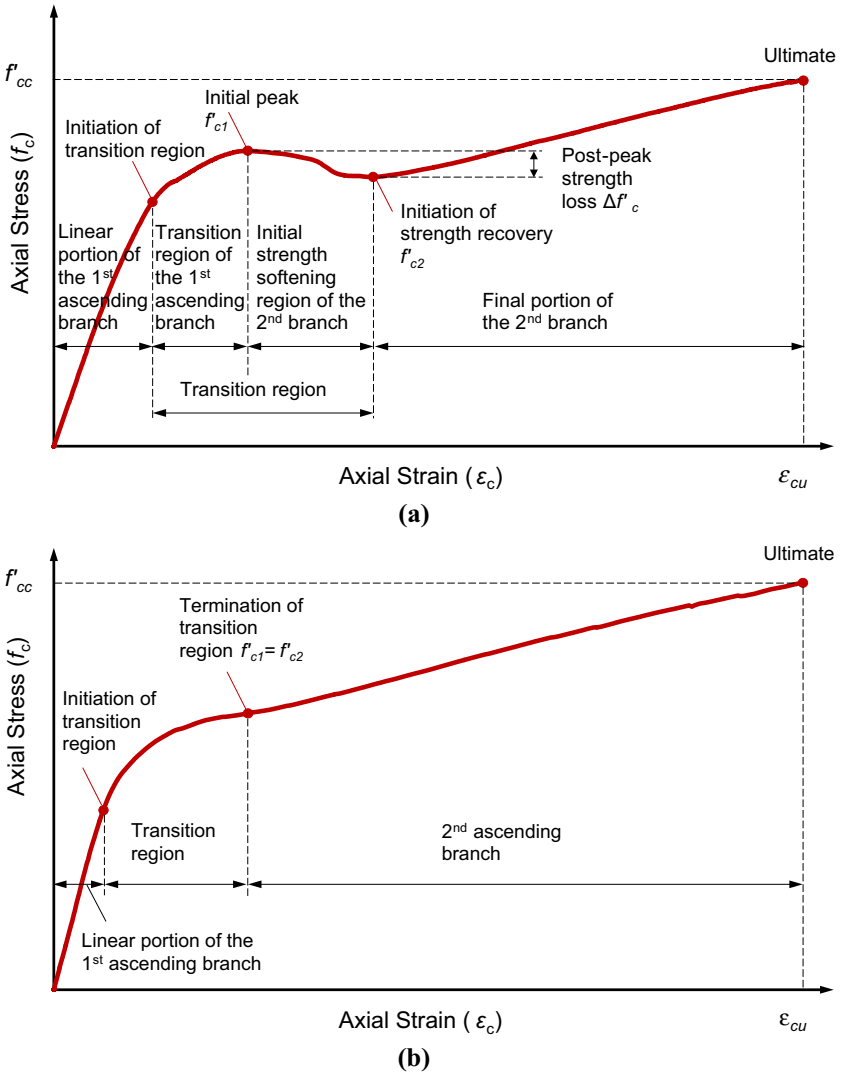

Fig. 5. Illustration of different stages of axial stress–strain curves: (a) stress–strain curve with strength loss; (b) stress–strain curve without strength loss.

3.2.3. Hoop strains

FRP hoop rupture strains ($\varepsilon_{h,rup}$) of the specimens of the present study, which were averaged from 9 strain gauges placed at specimen mid-height outside the overlap region, are shown in Table 8. In addition, experimental values of FRP hoop strain-reduction factors ($k_{\varepsilon,exp}$) calculated from Eq. (2) are also given in the same table.

$$k_{\varepsilon,exp} = \frac{\varepsilon_{h,rup}}{\varepsilon_{fu}} \tag{2}$$

In Eq. (2), $\varepsilon_{h,rup}$ is the experimentally recorded FRP hoop-rupture strain and ε_{fu} is the ultimate tensile strain of fibers. Both the experimental and theoretical values of FRP hoop strain-reduction factor ($k_{\varepsilon,exp}$ and $k_{\varepsilon,theo}$) are given in Table 8. Theoretical values of FRP hoop strain-reduction factors ($k_{\varepsilon,theo}$) were calculated using the expression proposed by Lim and Ozbakkaloglu [3] to predict the strain reduction factor of FRP-confined plain concrete, which is given in Eq. (3).

$$k_{\varepsilon,theo} = 0.9 - 2.3f'_{co} \times 10^{-3} - 0.75E_f \times 10^{-6} \tag{3}$$

In Eq. (3), f'_{co} is the axial compressive strength of the unconfined concrete in MPa, and E_f is the elastic modulus of fibers, where 100,000 MPa $\leqslant E_f \leqslant$ 640,000 MPa.

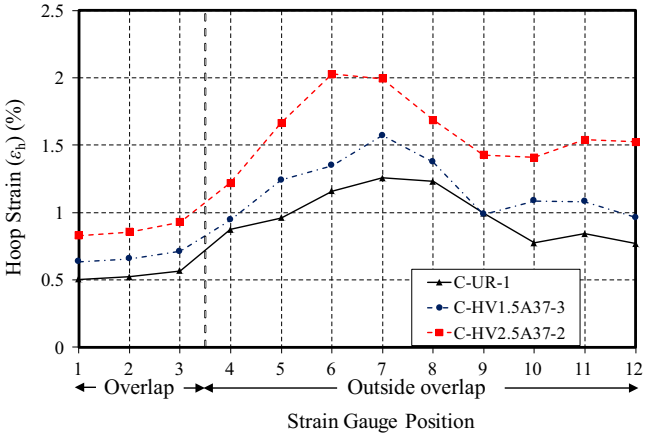

Fig. 6. Influence of inner steel fibers on hoop strain distributions of CFFTs.

The results shown in Table 8 indicate that the CFFTs with inner steel fibers developed higher hoop rupture strains ($\varepsilon_{h,rup}$) than those of the companion unreinforced CFFTs. It is also evident from the comparison of hoop rupture strain distributions of C-UR,

C-HV1.5A37 and C-HV2.5A37 series specimens illustrated in Fig. 6 that an increase in fiber volume fraction resulted in an increase in hoop rupture strain. The comparison of the experimental and theoretical values of FRP hoop strain-reduction factors ($k_{\varepsilon,exp}$ and $k_{\varepsilon,theo}$) in Table 8 indicates that Eq. (3) provides reasonably close predictions of $k_{\varepsilon,exp}$ for the unreinforced specimens. On the other hand, due to an increase in $\varepsilon_{h,rup}$ resulting from the presence of inner steel fibers, the equation underestimates $k_{\varepsilon,exp}$ of the CFFTs internally reinforced by steel fibers.

To explain this observation on the influence of internal fiber on the hoop rupture strain, it would be beneficial to have a closer look at crack formations in concrete under axial compression. As discussed previously in a number of studies, the brittleness of concrete increases with an increase in its compressive strength, which results in a change in crack pattern from heterogenic micro-cracks observed in NSC to localized macro-cracks experienced by HSC [12,17,29,32,35,37]. In the case of FRP-confined HSC, the localized macro-cracks that occur inside the concrete lead to stress concentrations on the FRP jacket, where the rupture of the jacket initiates. Because, at the time of failure, the hoop strains outside these stress concentration regions of infinitesimal length are significantly lower than that within the region, this failure mode results in lower recorded FRP hoop rupture strains. It was experimentally observed that, in the steel fiber reinforced specimens of the present study, the steel fibers formed bridges across the cracks of the concrete leading to a more even and controlled cracking, which in turn resulted in the reduction of isolated major cracks of concrete and the stress concentrations on the FRP jacket. Consequently, these specimens exhibited higher FRP hoop rupture strains compared to those observed in the companion unreinforced CFFTs.

3.2.4. Influence of test parameters on observed behavior

Axial stress–strain curves of the unreinforced and steel fiber reinforced CFFTs are shown in Figs. 7 and 8, respectively. In these curves, axial strains were obtained from full-height LVDTs. Previous research has established that sufficiently confined concrete exhibits a monotonically ascending curve, which consists of a parabolic first ascending portion and a nearly linear second branch [3,29,32,63]. However, it is now understood that FRP-confined HSC specimens may exhibit a sudden drop in their axial load capacity and corresponding axial stress immediately after the initial peak condition on their stress–strain relationship. This behavior, which is caused by the brittle nature of HSC as was discussed in detail previously [3,12,17,29,32,35,37], is referred to in the present study as the initial strength softening behavior, and the region corresponding to it is highlighted on the stress–strain curve shown in Fig. 5(a).

As illustrated in Fig. 7(a) and (b), all unreinforced specimens of the present study (i.e., HSCFFTs and unreinforced SIFCONFFTs) exhibited sudden post-peak strength losses in their axial stress–strain relationships. As shown in Fig. 8(a), (c) and (e), a similar loss was also experienced by the fiber reinforced specimens with a lower steel fiber volume fraction (i.e., V_f = 1.5%). On the other hand, as evident from Fig. 8(b), (d), (f) and (g), SFRHSCFFTs with a higher fiber volume fraction (i.e., V_f = 2.5%) and SIFCONCFFTs exhibited virtually no post-peak strength loss. These observations are also supported by the $\Delta f'_c$ values reported in Table 6, which indicate that the magnitude of the post-peak strength loss ($\Delta f'_c$) of HSCFFTs can be significantly reduced through the use of steel fibers.

Detailed discussions on the influence of each test parameter on the axial stress–strain behavior of CFFTs are provided in the following sections.

3.2.4.1. Effect of concrete type. The influence of the concrete type on the compressive behavior of CFFTs is investigated by comparing

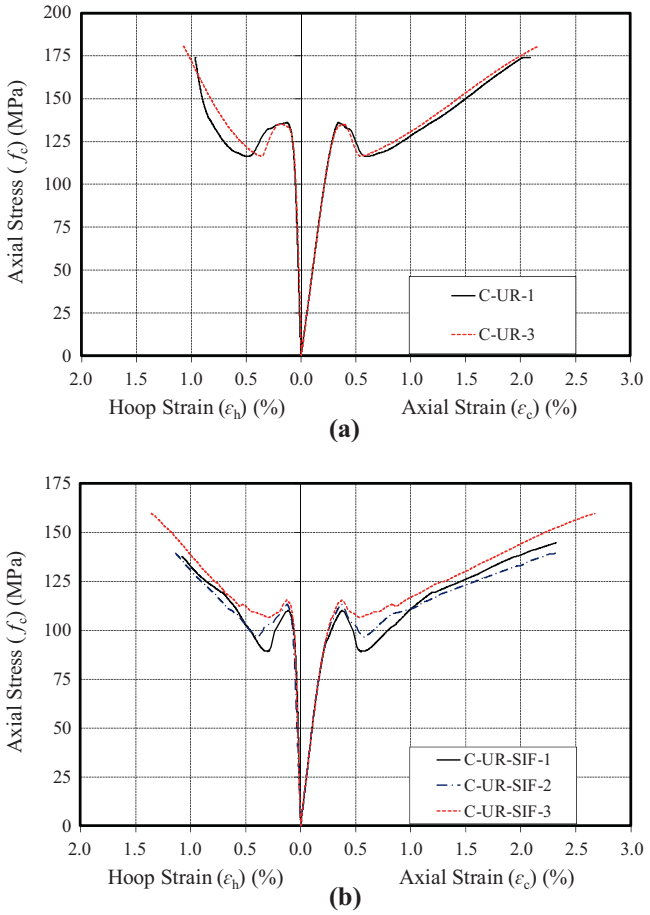

Fig. 7. Axial stress–strain behavior of unreinforced CFFTs: (a) C-UR series; (b) C-UR-SIF series.

the specimens manufactured with two different types of unreinforced concrete (i.e., conventional HSC and unreinforced SIFCON). It is evident from the stress–strain curves shown in Fig. 9 and the results reported in Table 6 that the HSCFFTs had higher compressive strengths (f'_{cc}) than the unreinforced SIFCONFFTs. Although this can be partly explained by the slightly higher unconfined concrete strength (f'_{co}) of the former group, as evident from Tables 6, the HSCFFTs also developed a slightly higher strength enhancement ratio (f'_{cc}/f'_{co}) compared to that of the unreinforced SIFCONFFTs. On the other hand, as shown in Table 7, the latter group exhibited a higher ultimate strain (ε_{cu}) than that of the former. The results in Table 6 also show that the HSCFFTs and unreinforced SIFCONFFTs exhibited similar post-peak strength losses ($\Delta f'_c$).

As was established in previous studies, the strength and crack resistance of conventional concrete increases with an increase in its coarse aggregate content, due to the interlock effect of the material [64–67]. After the formation of the initial cracks, the coarse aggregates on the crack surfaces provide an interlocking action, which slows the crack propagations, resulting in an improved compressive strength and reduced axial deformation of the concrete. This mechanism can explain the higher strength enhancement ratio (f'_{cc}/f'_{co}) and relatively lower ultimate strain (ε_{cu}) of the HSCFFTs with coarse aggregates compared to those of the companion unreinforced SIFCONs that contained no coarse aggregates. However, no clear influence of this interlock mechanism is evident on the post-peak strength loss region, suggesting that the full formation of the said mechanism takes place during the later stages of testing.

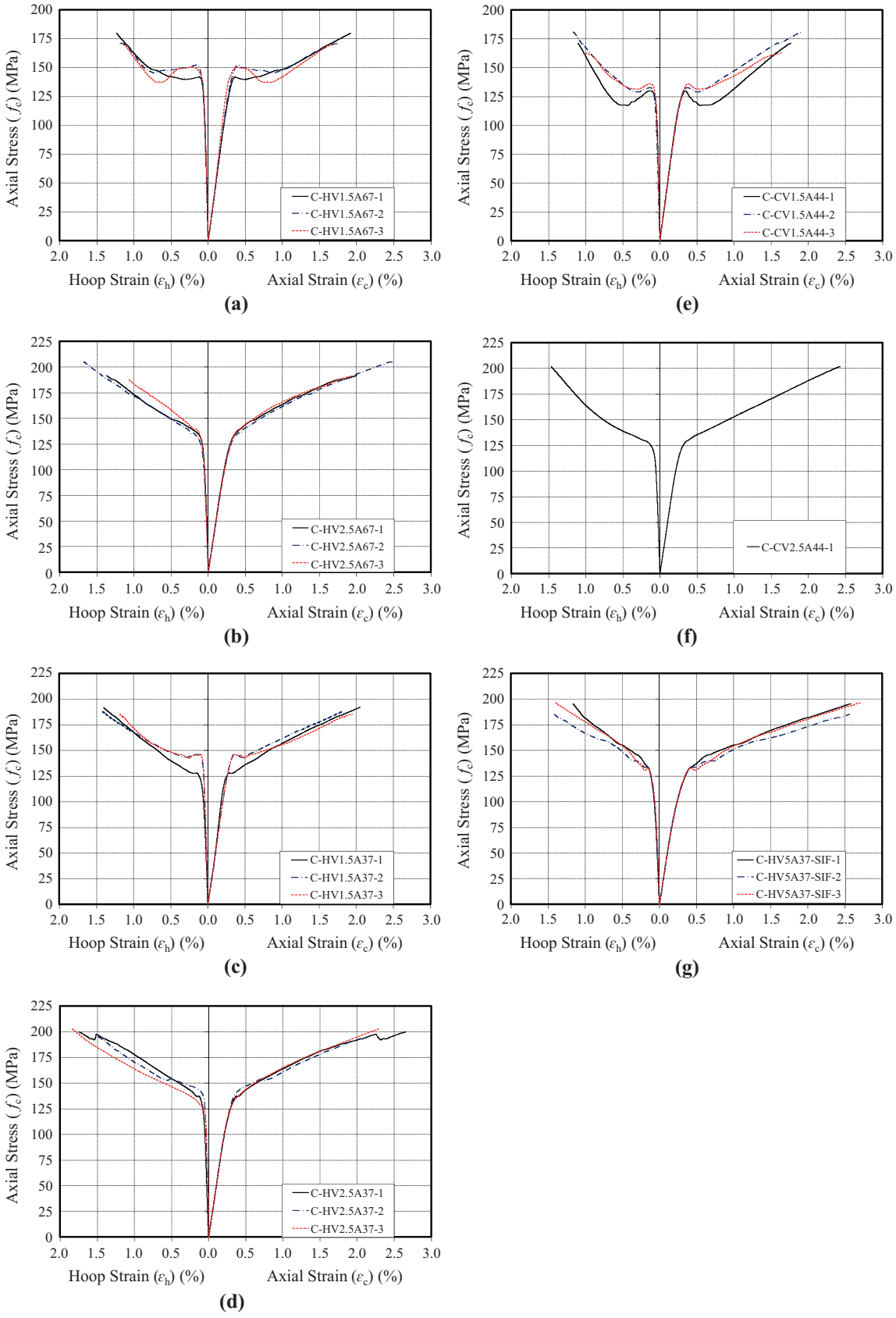

Fig. 8. Axial stress–strain behavior of fiber reinforced CFFTs: (a) C-HV1.5A67 series; (b) C-HV2.5A67 series; (c) C-HV1.5A37 series; (d) C-HV2.5A37 series; (e) C-CV1.5A37 series of specimens; (f) C-CV2.5A37 series; (g) C-HV5A37-SIF series.

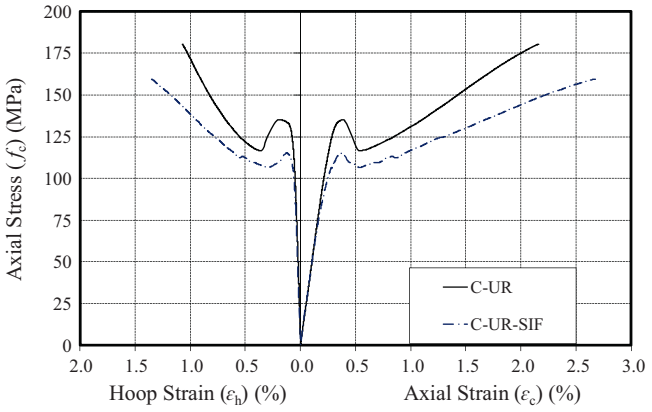

Fig. 9. Influence of concrete type on compressive behavior of unreinforced CFFTs: C-UR series vs. C-UR-SIF series.

In addition to the above observations, it can also be seen from the results reported in Tables 8 that the unreinforced SIFCONFFTs developed a slightly higher hoop rupture strain ($\varepsilon_{h,rup}$) than the HSCFFTs with a slightly higher unconfined concrete strength (f'_{co}). This finding is in general agreement with those of the previous studies, where it was found that the hoop rupture strains ($\varepsilon_{h,rup}$) decrease with an increase in the unconfined concrete strength (f'_{co}) [3,12,37].

3.2.4.2. Effect of steel fiber shape. Fig. 10(a) and (b) illustrates the influence of the fiber shape on the axial stress–strain behavior of SFRHSCFFTs. The curves shown in Fig. 10(a) and the results given in Tables 6 and 7 illustrate that the hooked end steel fibers performed better than the crimped fibers in improving the compressive behavior of the SFRHSCFFTs at a lower fiber volume fraction (i.e., V_f = 1.5%). The compressive strengths (f'_{cc}) and ultimate strains (ε_{cu}) of C-HV1.5A37 series specimens with hooked end fibers were slightly higher than those of C-CV1.5A44 series specimens with crimped fibers. As evident from Fig. 10(a), between the two groups, C-HV1.5A37 series specimens experienced a lower post-peak strength loss ($\Delta f'_c$) compared to that experienced by C-CV1.5A44 series specimens. Moreover, the comparison of the $\varepsilon_{h,rup}$ values of these companion groups in Table 8 shows that the specimens with hooked end fibers developed higher FRP hoop rupture strain ($\varepsilon_{h,rup}$) compared to their companions with crimped fibers.

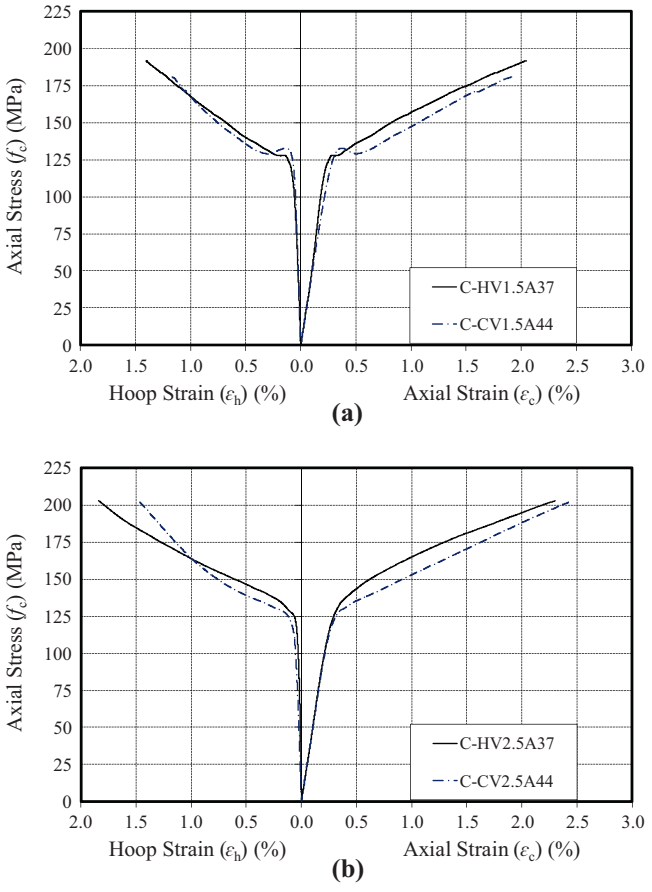

Fig. 10. Influence of fiber shape on compressive behavior of SFRCHSCFFTs: (a) V_f = 1.5%; (b) V_f = 2.5%.

For the specimens with a higher fiber volume fraction (i.e., V_f = 2.5%), it is evident from the stress–strain curves shown in Fig. 10(b) and the test results given in Tables 6 and 7, C-HV2.5A37 series specimens with hooked end fibers and the companion C-CV2.5A44 series specimens with crimped fibers exhibited almost identical compressive strengths (f'_{cc}) and ultimate strains (ε_{cu}). The $\Delta f'_c$ values shown in Table 6 indicate that the addition of a higher volume fraction (i.e., V_f = 2.5%) of hooked end and crimped fibers resulted in full prevention of the post-peak strength loss of HSCFFTs. In addition, the comparison of the $\varepsilon_{h,rup}$ values of these companion specimens in Table 8 indicates that the specimens with hooked end fibers developed higher FRP hoop rupture strains ($\varepsilon_{h,rup}$) compared to their companion with crimped fibers. This finding is in agreement with that from the previous comparison group with V_f = 1.5%.

The observations presented in this section suggest that the hooked end fibers are more effective in improving the overall compressive behavior of HSCFFTs than crimped fibers. This finding is in support of those reported on the compressive behavior of unconfined SFRHSCs previously that the hooked end fibers provided a more pronounced improvement on the post-peak stress–strain behavior compared to crimped fibers [39,42]. The better performance of specimens with hooked end fibers can be attributed to the higher bond strengths between the fibers and concrete that result from the fiber geometry, which results in a better composite action.

3.2.4.3. Effect of fiber volume fraction. Fig. 11(a)–(d) presents the influence of the fiber volume fraction (V_f) on the axial compressive behavior of the SFRHSCFFT and SIFCONFFT specimens of the present study. The specimens in each comparison group were prepared using the same concrete mix and steel fibers, and they were nominally identical except for their steel fiber volume fractions (V_f). Stress–strain curves shown in Fig. 11(a)–(c) and the results given in Table 6 indicate that an increase in fiber volume fraction (V_f) led to an increase in compressive strength (f'_{cc}) of SFRHSCFFTs. As evident from Table 7, the specimens with the fiber volume fraction of 2.5% (V_f = 2.5%) also exhibited higher ultimate axial strains (ε_{cu}) compared to their companions with V_f = 0% or 1.5%. However, the results show that the ultimate strains of the specimens with V_f = 1.5% were slightly lower than those of the companion unreinforced HSCFFTs. These observations indicate that the ultimate axial strain of HSCFFTs is sensitive to fiber volume fraction of the concrete. The stress–strain curves illustrated in Fig. 11(a)–(c) and the results reported in Table 6 also reveal that specimens with higher fiber volume fraction ratio experienced a lower post-peak strength loss ($\Delta f'_c$). It is evident from these results that the provision of internal fibers at V_f = 2.5% resulted in complete prevention of the post-peak strength loss, which is otherwise typically experienced by HSCFFTs. In addition, as discussed previously, the specimens reinforced with steel fibers at V_f = 2.5%

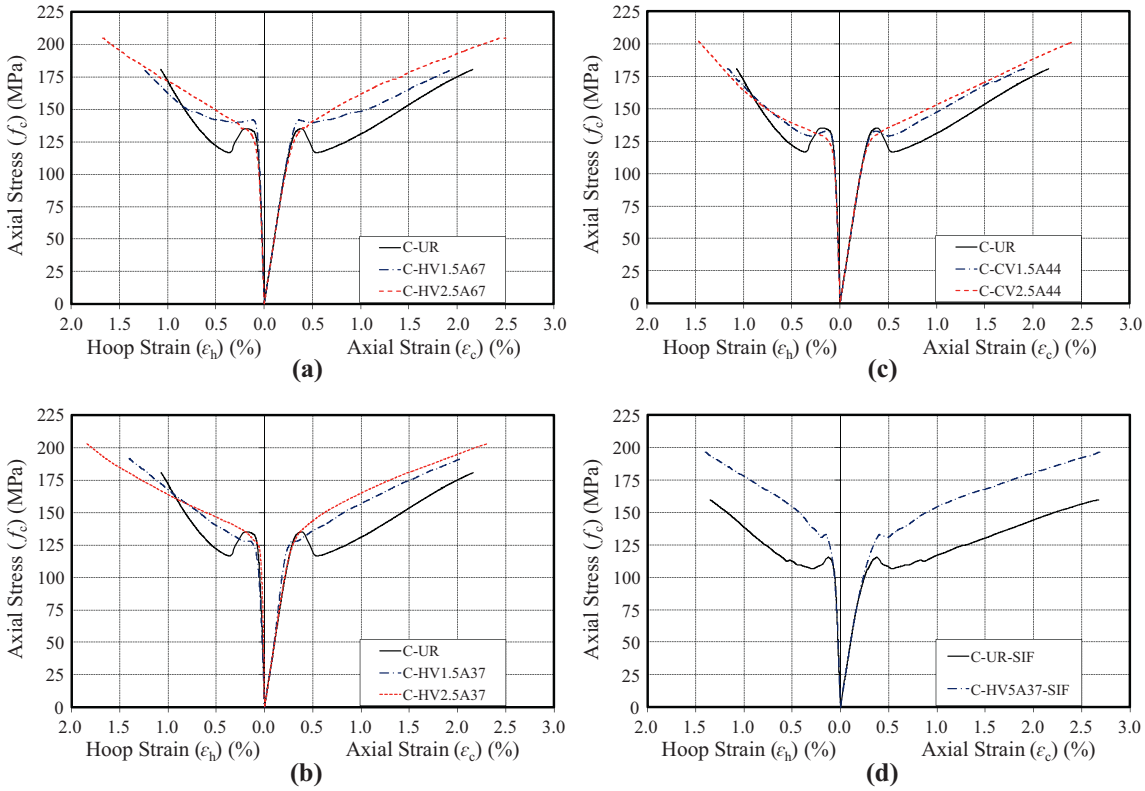

Fig. 11. Influence of steel fiber volume fraction on compressive behavior of SFRCHSCFFTs and SIFCONFFTs: (a) hooked end fibers, A_s = 67; (b) hooked end fibers, A_s = 37; (c) crimped fibers, A_s = 44; (d) hooked end fibers, A_s = 37 (SIFCON).

exhibited significantly higher FRP hoop rupture strains compared to those observed in the companion unreinforced CFFTs.

Fig. 11(d) presents the influence of the fiber volume fraction (V_f) on the compressive behavior of the SIFCONFFTs. The stress–strain curves shown in this figure and the results presented in Tables 6 and 7 indicate that the presence of internal steel fibers resulted in an increase both the compressive strength (f'_{cc}) and ultimate axial strain (ε_{cu}) of SIFCONFFTs. It is also evident from the results that the post-peak strength losses ($\Delta f'_c$) that were experienced by the unreinforced specimens (i.e., C-UR-SIF) were not observed in the internally reinforced SIFCONFFTs (i.e., C-HV5A37-SIF). Furthermore, in agreement with what was seen for the conventional HSCFFTs, it was observed that C-HV5A37-SIF series specimens developed higher FRP hoop rupture strains compared to those of C-UR-SIF series specimens. These observations from the conventional HSC- and SIFCON-CFFTs indicate that the presence of internal steel fibers benefit the compressive behavior of both groups in a similar manner. The comparison of the HSCFFTs with V_f = 2.5% with SIFCONFFTs indicate that these groups of specimens exhibited comparable stress enhancement ratios (f'_{cc}/f'_{co}) and ultimate strains (ε_{cu}). Slightly higher values observed in SIFCONFFTs can be attributed to the higher fiber volume fraction (i.e., V_f = 5%) of these specimens.

In explaining the above findings, it is worthwhile to refer to previously reported studies on unconfined SFRHSCs, where it was found that the specimens with higher fiber volume fractions exhibited higher compressive strengths and decreased slopes in the descending branches of their stress–strain curves [40,41,44,46]. These improvements in the axial stress–strain behavior are attributable to the confinement effect of the internal steel fibers, which is directly correlated to the volume of steel fibers. The results of the present study indicate that this additional confinement provided by the internal steel fibers results in enhancements in the compressive strength (f'_{cc}), ultimate strain (ε_{cu}), post-peak strength loss ($\Delta f'_c$) and FRP hoop rupture strain ($\varepsilon_{h,rup}$) of CFFTs manufactured with conventional HSC and SIFCON. It is clear from these findings that fiber volume fraction should be treated as an influential parameter on the axial compressive behavior of CFFTs.

3.2.4.4. Effect of fiber aspect ratio. To illustrate the influence of the fiber aspect ratio (A_s) on the behavior of SFRHSCFFTs, Fig. 12(a) and (b) shows the stress–strain curves of companion specimens with different fiber aspect ratios (i.e., A_s = 37 or 67). As can be seen from the curves of the specimens with a lower fiber volume fraction ratio (i.e., V_f = 1.5%) in Fig. 12(a), C-HV1.5A37 series specimens exhibited stress–strain curves with slightly longer second branches compared to those of the companion C-HV1.5A67 series specimens, which contributed to the higher compressive strengths (f'_{cc}) and ultimate axial strains (ε_{cu}) of the former group. As evident from the $\Delta f'_c$ values given in Table 6, C-HV1.5A37 series specimens also experienced lower post-peak strength losses ($\Delta f'_c$) compared to C-HV1.5A67 series specimens. In addition, as can be seen in Table 8, the former group exhibited higher FRP hoop rupture strains ($\varepsilon_{h,rup}$) compared to those of the latter group. The companion of the specimens with a higher fiber volume fraction (i.e., C-HV2.5A37 and C-HV2.5A67) in Fig. 12(b) and Tables 6–8 leads to similar observations with those obtained from C-HV1.5 series specimens. That is, the specimens with a lower fiber aspect ratio (i.e., A_s = 37) developed slightly higher compressive strengths (f'_{cc}), ultimate axial strains (ε_{cu}) and FRP hoop rupture strains ($\varepsilon_{h,rup}$) compared those seen in specimens reinforced with longer fibers (i.e., A_s = 67).

These observations indicate that the steel fibers with lower aspect ratios are more effective in improving the compressive behavior of HSCFFTs that the fibers with higher aspect ratio in improving the axial compressive behavior of CFFTs. This finding is in support of those reported in previous studies on unconfined

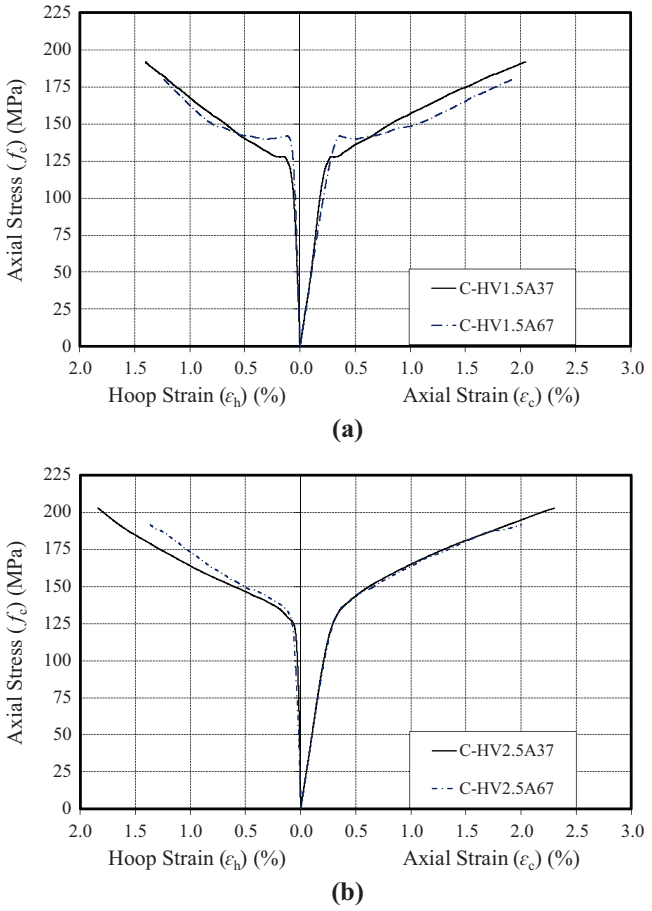

Fig. 12. Influence of fiber aspect ratio on compressive behavior of SFRCHSCFFTs: (a) V_f = 1.5%; (b) V_f = 2.5%.

SFRHSCs [40,41,43,45,46], where it was found that the second branch slope of the axial stress–train curves were influenced by the fiber aspect ratio. In these studies, it was observed that the slope of the descending branch of the stress–strain curve of unconfined SFRHSCs decreased with an increase in the aspect ratio of steel fibers (A_s). This influence can be explained to the ability of steel fibers with lower aspect ratios to effectively control the initiation and propagation of initial cracks of SFRHSCs under increasing axial deformation [41,45]. On the other hand, the fibers with higher aspect ratios have been reported to be less effective in arresting crack propagation immediately after the formation of initial cracks [41,45]. In addition, for a given fiber diameter (d_f) and volume fraction (V_f), the number of fibers increase with a decrease in the fiber aspect ratio (A_s), which results in a more scattered distribution leading to an increased likelihood for the path of cracks to cross through the fibers [46,68]. These properties of the shorter steel fibers make them more effective in providing internal confinement to concrete, which in turn leads to an improved compressive behavior of SFRHSCs manufactured with such fibers. The findings of the present study indicate that this mechanism is also in action in SFRCHSCFFTs.

4. Conclusions

This paper has presented the results of an experimental study on the behavior of the influence of steel fibers on the axial compressive behavior of HSCFFTs. Based on the discussions and results presented in this study, the following conclusions can be drawn:

1. Sufficiently confined circular HSCFFTs, SFRHSCFFTs and SIFCONFFTs exhibit highly ductile axial compressive behavior. Among the different specimen groups investigated in this study, SIFCONFFTs with a fiber volume fraction (V_f) of 5% exhibited the highest strength enhancements and ultimate axial strains.
2. The presence of steel fibers reduces the isolated major crack formations in HSC and leads to a more even and controlled cracking of concrete under axial compression. This in turn reduces the stress concentrations on the FRP jacket, leading to higher FRP hoop rupture strains ($\varepsilon_{h,rup}$) of CFFTs.
3. SFRHSCFFTs and SIFCONFFTs exhibit lower post-peak strength losses ($\Delta f'_c$) compared to that of companion HSCFFTs. It was observed SFRHSCFFTs with 2.5% steel fiber volume fraction and SIFCONFFTs with 5% fiber volume fraction experienced virtually no strength loss ($\Delta f'_c$).
4. Under the same amount of FRP confinement, HSCFFTs and unreinforced SIFCONFFTs with comparable unconfined concrete strengths (f'_{co}) exhibit similar post-peak strength losses ($\Delta f'_c$). However, HSCFFTs exhibit slightly higher axial strength enhancement ratios (f'_{cc}/f'_{co}) but significantly lower axial strains (ε_{cu}) compared to those of unreinforced SIFCONFFTs.
5. At a given fiber volume fraction (V_f) and fiber aspect ratio (A_s), the shape of steel fibers has only a minor influence on the axial compressive behavior of SFRHSCFFTs. It was found that the CFFTs reinforced with hooked end steel fibers developed slightly higher compressive strengths (f'_{cc}) and FRP hoop rupture strains ($\varepsilon_{h,rup}$), and exhibited lower post-peak strength losses ($\Delta f'_c$) compared to the companion CFFTs containing crimped fibers. No significant correlation was evident between the fiber shape and the ultimate axial strain (ε_{cu}) of CFFTs.
6. At a given fiber volume fraction (V_f), CFFTs reinforced with hooked end fibers with a lower aspect ratio (i.e., A_s = 37) develop higher compressive strengths (f'_{cc}), ultimate axial strains (ε_{cu}) and hoop rupture strains ($\varepsilon_{h,rup}$), and they also exhibit lower post-peak strength losses ($\Delta f'_c$) compared to those seen in companion CFFTs containing hooked end fibers with a higher aspect ratio (i.e., A_s = 67). It was observed that even at a lower fiber volume fraction (i.e., V_f = 1.5%), A_s = 37 fibers were able to prevent the post-peak strength loss of CFFTs almost fully.
7. Axial compressive behavior of SFRHSCFFTs and SIFCONFFTs is significantly influenced by the volume fraction of steel fibers (V_f). The CFFTs contacting fibers at a higher volume fraction (i.e., V_f = 2.5%) exhibits improved ultimate conditions (i.e., f'_{cc} and ε_{cu}) and a post-peak strength loss behavior compared to companion CFFTs with a lower fiber volume fraction (i.e., V_f = 1.5%).

Acknowledgements

The authors would like to extend their gratitude to Ms. Hu and Zhao, and Messrs. Wen and Zheng, who performed the experimental procedures presented in this paper. This research is part of an ongoing program at The University of Adelaide on FRP-concrete composite columns.

References

[1] Ozbakkaloglu T, Lim JC. Axial compressive behavior of FRP-confined concrete: experimental test database and a new design-oriented model. Compos B Eng 2013;55:607–34.
[2] Ozbakkaloglu T, Lim JC, Vincent T. FRP-confined concrete in circular sections: review and assessment of stress–strain models. Eng Struct 2013;49:1068–88.
[3] Lim JC, Ozbakkaloglu T. Confinement model for FRP-confined high-strength concrete. J Compos Constr ASCE 2014;17(5):1–19.
[4] Lim JC, Ozbakkaloglu T. Lateral strain-to-axial strain relationship of confined concrete. J Struct Eng ASCE 2014. http://dx.doi.org/10.1061/(ASCE)ST.1943-541X.0001094.

[5] Karabinis AI, Rousakis TC. Concrete confined by FRP material: a plasticity approach. Eng Struct 2002;24(7):923–32.
[6] Lam L, Teng JG. Ultimate condition of fiber reinforced polymer-confined concrete. J Compos Constr 2004;8(6):539–48.
[7] Ilki A, Peker O, Karamuk E, Demir C, Kumbasar N. FRP retrofit of low and medium strength circular and rectangular reinforced concrete columns. J Mater Civ Eng 2008;20(2):169–88.
[8] Kusumawardaningsih Y, Hadi MNS. Comparative behaviour of hollow columns confined with FRP composites. Compos Struct 2010;93(1):198–205.
[9] Wu YF, Wei YY. Effect of cross-sectional aspect ratio on the strength of CFRP-confined rectangular concrete columns. Eng Struct 2010;32(1):32–45.
[10] Dai JG, Bai YL, Teng JG. Behavior and modeling of concrete confined with FRP composites of large deformability. J Compos Constr 2011;15(6):963–73.
[11] Wang Z, Wang D, Smith ST, Lu D. CFRP-confined square RC columns. I: experimental investigation. J Compos Constr 2011;16(2):150–60.
[12] Ozbakkaloglu T, Akin E. Behavior of FRP-confined normal-and high-strength concrete under cyclic axial compression. J Compos Constr 2012;16(4):451–63.
[13] Mirmiran A, Shahawy M, Samaan M, Echary HE, Mastrapa JC, Pico O. Effect of column parameters on FRP-confined concrete. J Compos Constr 1998;2(4):175–85.
[14] Fam A, Schnerch D, Rizkalla S. Rectangular filament-wound glass fiber reinforced polymer tubes filled with concrete under flexural and axial loading: experimental investigation. J Compos Constr 2005;9(1):25–33.
[15] Li G. Experimental study of FRP confined concrete cylinders. Eng Struct 2006;28(7):1001–8.
[16] Park JH, Jo BW, Yoon SJ, Park SK. Experimental investigation on the structural behavior of concrete filled FRP tubes with/without steel re-bar. KSCE J Civ Eng 2011;15(2):337–45.
[17] Ozbakkaloglu T. Compressive behavior of concrete-filled FRP tube columns: assessment of critical column parameters. Eng Struct 2013;51:188–99.
[18] Ozbakkaloglu T. Concrete-filled FRP tubes: manufacture and testing of new forms designed for improved performance. J Compos Constr 2013;17(2):280–91.
[19] Berthet JF, Ferrier E, Hamelin P. Compressive behavior of concrete externally confined by composite jackets. Part A: experimental study. Constr Build Mater 2005;19(3):223–32.
[20] Mandal S, Hoskin A, Fam A. Influence of concrete strength on confinement effectiveness of fiber-reinforced polymer circular jackets. ACI Struct J 2005;102(3).
[21] Almusallam TH. Behavior of normal and high-strength concrete cylinders confined with E-glass/epoxy composite laminates. Compos B Eng 2007;38(5):629–39.
[22] Eid R, Roy N, Paultre P. Normal-and high-strength concrete circular elements wrapped with FRP composites. J Compos Constr 2009;13(2):113–24.
[23] Wu HL, Wang YF, Yu L, Li XR. Experimental and computational studies on high-strength concrete circular columns confined by aramid fiber-reinforced polymer sheets. J Compos Constr 2009;13(2):125–34.
[24] Cui C, Sheikh SA. Experimental study of normal-and high-strength concrete confined with fiber-reinforced polymers. J Compos Constr 2010;14(5):553–61.
[25] Xiao QG, Teng JG, Yu T. Behavior and modeling of confined high-strength concrete. J Compos Constr 2010;14(3):249–59.
[26] Zohrevand P, Mirmiran A. Behavior of ultrahigh-performance concrete confined by fiber-reinforced polymers. J Mater Civ Eng 2011;23(12):1727–34.
[27] Pham TM, Hadi MN. Confinement model for FRP confined normal-and high-strength concrete circular columns. Constr Build Mater 2014;69:83–90.
[28] Ozbakkaloglu T. Axial compressive behavior of square and rectangular high-strength concrete-filled FRP tubes. J Compos Constr ASCE 2013;17(1):151–61.
[29] Ozbakkaloglu T, Vincent T. Axial compressive behavior of circular high-strength concrete-filled FRP tubes. J Compos Constr 2013;18(2):04013037.
[30] Louk Fanggi BAL, Ozbakkaloglu T. Compressive behavior of aramid FRP–HSC–steel double-skin tubular columns. Constr Build Mater 2013;48:554–65.
[31] Idris Y, Ozbakkaloglu T. Seismic behavior of high-strength concrete-filled FRP tube columns. J Compos Constr 2013;17(6):04013013.
[32] Ozbakkaloglu T. Behavior of square and rectangular ultra high-strength concrete-filled FRP tubes under axial compression. Compos B Eng 2013;54:97–111.
[33] Ozbakkaloglu T, Fanggi BAL. Axial compressive behavior of FRP-concrete-steel double-skin tubular columns made of normal-and high-strength concrete. J Compos Constr 2013;18(1):04013027.
[34] Ozbakkaloglu T, Fanggi BAL. FRP–HSC–steel composite columns: behavior under monotonic and cyclic axial compression. Mater Struct 2013. http://dx.doi.org/10.1617/s11527-013-0216-0.
[35] Vincent T, Ozbakkaloglu T. Influence of concrete strength and confinement method on axial compressive behavior of FRP confined high-and ultra high-strength concrete. Compos B Eng 2013;50:413–28.
[36] Vincent T, Ozbakkaloglu T. Influence of fiber orientation and specimen end condition on axial compressive behavior of FRP-confined concrete. Constr Build Mater 2013;47:814–26.
[37] Lim J, Ozbakkaloglu T. Influence of silica fume on stress–strain behavior of FRP-confined HSC. Constr Build Mater 2014;63:11–24.
[38] Ozbakkaloglu T, Idris Y. Seismic behavior of FRP-high-strength concrete-steel double skin tubular columns. J Struct Eng ASCE 2014;140(6):04014019.
[39] Soroushian P, Bayasi Z. Fiber type effects on the performance of steel fiber reinforced concrete. ACI Mater J 1991;88(2).
[40] Nataraja MC, Dhang N, Gupta AP. Stress–strain curves for steel-fiber reinforced concrete under compression. Cem Concr Compos 1999;21(5):383–90.
[41] Bhargava P, Sharma UK, Kaushik SK. Compressive stress–strain behavior of small scale steel fibre reinforced high strength concrete cylinders. J Adv Concr Technol 2006;4(1):109–21.
[42] Holschemacher K, Müller T. Influence of fibre type on hardened properties of steel fibre reinforced concrete. Modern building materials, structures and techniques. In: Proceedings of the 9th international conference, Vilnius; 2007.
[43] Bencardino F, Rizzuti L, Spadea G, Swamy RN. Stress–strain behavior of steel fiber-reinforced concrete in compression. J Mater Civ Eng 2008;20(3):255–63.
[44] Paultre P, Eid R, Langlois Y, Lévesque Y. Behavior of steel fiber-reinforced high-strength concrete columns under uniaxial compression. J Struct Eng 2010;136(10):1225–35.
[45] Khalil WI, Gorgis IN, Mahdi ZR. Behavior of high performance fiber reinforced concrete column. J Eng Appl Sci 2012;7(11).
[46] Ezeldin AS, Balaguru PN. Normal-and high-strength fiber-reinforced concrete under compression. J Mater Civ Eng 1992;4(4):415–29.
[47] Ding Y, Kusterle W. Compressive stress–strain relationship of steel fibre-reinforced concrete at early age. Cem Concr Res 2000;30(10):1573–9.
[48] Kholmyansky MM. Mechanical resistance of steel fiber reinforced concrete to axial load. J Mater Civ Eng 2002;14(4):311–9.
[49] Ramesh K, Seshu DR, Prabhakar M. Constitutive behaviour of confined fibre reinforced concrete under axial compression. Cem Concr Compos 2003;25(3):343–50.
[50] Sukontasukkul P, Mindess S, Banthia N. Properties of confined fibre-reinforced concrete under uniaxial compressive impact. Cem Concr Res 2005;35(1):11–8.
[51] Thomas J, Ramaswamy A. Mechanical properties of steel fiber-reinforced concrete. J Mater Civ Eng 2007;19(5):385–92.
[52] Xu LH, Xia DT, Xia GZ, Chi Y. Effect of steel fiber and polypropylene fiber on the strength of high strength concrete. J Wuhan Univ Technol 2007;29(4):58–60.
[53] Holschemacher K, Mueller T, Ribakov Y. Effect of steel fibres on mechanical properties of high-strength concrete. Mater Des 2010;31(5):2604–15.
[54] Ayan E, Saatçioğlu Ö, Turanli L. Parameter optimization on compressive strength of steel fiber reinforced high strength concrete. Constr Build Mater 2011;25(6):2837–44.
[55] Ou YC, Tsai MS, Liu KY, Chang KC. Compressive behavior of steel-fiber-reinforced concrete with a high reinforcing index. J Mater Civ Eng 2011;24(2):207–15.
[56] Chi Y, Xu L, Zhang Y. Experimental study on hybrid fiber-reinforced concrete subjected to uniaxial compression. J Mater Civ Eng 2012;26(2):211–8.
[57] Hassan AMT, Jones SW, Mahmud GH. Experimental test methods to determine the uniaxial tensile and compressive behaviour of ultra high performance fibre reinforced concrete (UHPFRC). Constr Build Mater 2012;37:874–82.
[58] Tokgoz S, Dundar C. Tests of eccentrically loaded L-shaped section steel fibre high strength reinforced concrete and composite columns. Eng Struct 2012;38:134–41.
[59] Wang S, Zhang MH, Quek ST. Mechanical behavior of fiber-reinforced high-strength concrete subjected to high strain-rate compressive loading. Constr Build Mater 2012;31:1–11.
[60] Caballero-Morrison KE, Bonet JL, Navarro-Gregori J, Serna-Ros P. An experimental study of steel fiber-reinforced high-strength concrete slender columns under cyclic loading. Eng Struct 2013;57:565–77.
[61] Hadi MN. Behaviour of eccentric loading of FRP confined fibre steel reinforced concrete columns. Constr Build Mater 2009;23(2):1102–8.
[62] ASTM. Standard test method for tensile properties of polymer matrix composites materials. D3039M-08, West Conshohocken, PA; 2008.
[63] Lam L, Teng JG. Design-oriented stress–strain model for FRP-confined concrete. Constr Build Mater 2003;17(6):471–89.
[64] Counto UJ. The effect of the elastic modulus of the aggregate on the elastic modulus, creep and creep recovery of concrete. Mag Concr Res 1964;16(48):129–38.
[65] Stock AF, Hannantt DJ, Williams RIT. The effect of aggregate concentration upon the strength and modulus of elasticity of concrete. Mag Concr Res 1979;31(109):225–34.
[66] Beshr H, Almusallam AA, Maslehuddin M. Effect of coarse aggregate quality on the mechanical properties of high strength concrete. Constr Build Mater 2003;17(2):97–103.
[67] Shen W, Dong R, Li J, Zhou M, Ma W, Zha J. Experimental investigation on aggregate interlocking concrete prepared with scattering–filling coarse aggregate process. Constr Build Mater 2010;24(11):2312–6.
[68] Vandewalle L. Postcracking behaviour of hybrid steel fiber reinforced concrete. In: Proc 6th int conf on fracture mechanics of concrete and concrete structures—FraMCoS, vol. 6; 2007. p. 1367–75.

CONCLUSIONS

This thesis has presented the results of an investigation into the development of novel concretes for structural applications. Research gaps were identified through a comprehensive review of current literature and a series of experimental studies were undertaken at the University of Adelaide to systematically address these gaps. The novel concrete technologies that have been investigated in this research study included: i) ambiently-cured coal ash-based geopolymer concrete (GPC), ii) recycled aggregate concrete (RAC), iii) RAC-filled FRP tubes, and iv) steel fibre-reinforced high-strength concrete- filled FRP tubes.

The research presented in this thesis makes a significant contribution to the current literature through its original findings on the investigated novel concretes and structural systems manufactured using them. The specific research contribution of each journal publication that resulted from this study [1-5] is summarized below.

1. Xie and Ozbakkaloglu [1] - This paper presented the first experimental study reported to date on the behaviour of bottom ash-and blended fly and bottom ash-based geopolymer concrete cured under ambient temperature. Several important findings on the observed influence of the mass ratio of fly ash-to-bottom ash, liquid alkaline-to-coal ash binder ratio, coal ash content and concrete type on the mechanical and durability-related properties of ambiently-cured GPCs were reported.

2. Xie and Ozbakkaloglu [2] - This paper presented the results of an experimental study on the compressive behaviour of GPCs. Findings on the influence of type, particle size and chemical composition of coal ash, the alkaline liquid to binder ratio and concentration of sodium hydroxide solution on the axial compressive behaviour and strength development of ambiently-cured GPCs were presented.

3. Xie and Ozbakkaloglu [3] - The study presented in this paper experimentally investigated the mechanical and durability-related properties of concretes of the same compressive strength prepared with coarse RCAs of different sizes and contents. The experimental study reported in this paper was the first to examine the influence of RCA size on the behaviour of RACs.

4. Xie and Ozbakkaloglu [4] - This paper presented the results of an experimental study on the axial compressive behaviour of RAC-filled basalt and carbon FRP tubes. The experimental study reported in this paper was the first study to report

on the axial compressive behaviour of CFFTs manufactured using high-strength RACs, and also the first study to investigate the behaviour of BFRP-confined RACs.

5. Xie and Ozbakkaloglu [5] - This paper presented the first experimental study on the axial compressive behaviour of steel fibre-reinforced high-strength concrete filled FRP tubes. Investigation of the axial compressive behaviour of 27 test specimens led to important findings on the influence of concrete type steel fibre shape, steel fibre aspect ratio and steel fibre volume fraction.

Recommendations for future research

The following recommendations made for future research:

1. No study has been reported to date on the use of nanomaterials to improve the performance of ambiently-cured GPCs. This forms an important direction for future research.
2. . There is a need for establishing a comprehensive test database for mechanical properties of GPCs to establish a clear understanding and model on the influence of important parameters on the behaviour of GPCs.
3. As shown in this thesis, the compressive strength of ambiently-cured GPCs tends to be lower than that of OPCs. It was also shown in this thesis that the use of FRP as external confinement can significantly improve the performance of concrete materials. Therefore, future research can investigate the behaviour of FRP-confined geopolymer concrete.
4. Investigation of the incorporation of other types of waste materials such as recycled coarse and fine aggregates, recycled plastic, foundry sand, glass powder to both GPC and OPC is recommended with the aim of producing high-volume waste-based concrete materials.

LIST OF PUBLICATIONS

[1] Xie, T., and Ozbakkaloglu, T. (2015). Behaviour of low-calcium fly and bottom ash-based geopolymer concrete cured at ambient temperature. *Ceramics International*, *41*(4), 5945-5958.

[2] Xie, T., and Ozbakkaloglu, T. (2015). Influence of coal ash properties on compressive behavior of FA-and BA-based GPC. *Magazine of Concrete Research*, 10.1680/macr.14.00429.

[3] Xie, T., and Ozbakkaloglu, T. (2015). Influence of Recycled Aggregate Size and Content on Behavior of Recycled Aggregate Concrete, *Journal of Cleaner Production*, (tentatively accepted subject to final revisions).

[4] Xie, T., and Ozbakkaloglu, T. (2015). Behavior of Recycled Aggregate Concrete-filled Basalt and Carbon FRP Tubes. (Submitted).

[5] Xie, T., and Ozbakkaloglu, T. (2015). Behavior of steel fiber-reinforced high-strength concrete-filled FRP tube columns under axial compression. *Engineering Structures*, *90*, 158-171.